Additive Manufacturing Processes for Photonics and Electronics

by

Benjamin Rorem

A dissertation submitted in partial fulfillment
of the requirements for the degree of
Doctor of Philosophy
(Applied Physics)
in the University of Michigan
2025

Doctoral Committee:

Professor L. Jay Guo, Chair
Professor John Heron
Professor Jinsang Kim
Professor Cagliyan Kurdak

Benjamin Rorem

brorem@umich.edu

ORCID iD: 0000-0003-0190-5090

© Benjamin Rorem 2025

Dedication

This thesis is dedicated to my family, Mark, Nancy, Amanda

and

my beloved Shiuli.

Acknowledgements

This PhD would not be possible without the help of many people. I would first like to thank Professor L. Jay Guo for his guidance over the past 5 years. He is truly one of a kind and always has new ideas. He gave me freedom to explore topics that interested me and always provided insightful perspectives when results were unclear. He has a strong grasp on conceptual ideas due to his physics background, and I was always encouraged to find connections between our results and well-known phenomena. I would also like to thank my dissertation committee members, Professor Cagliyan Kurdak, Professor Jinsang Kim, and Professor John Heron, for their support throughout my PhD. Prof. Kurdak is the director of the Applied Physics program and was instrumental in providing a welcoming environment upon my arrival to the University of Michigan, and I appreciate his willingness to discuss any troubles from academics to personal life. Prof. Kim was a patient and valuable mentor during our collaboration, and I am thankful for his expertise and clear communication when explaining macromolecular topics. Prof. Heron gave many valuable suggestions on metal oxide growth and XPS analysis and I appreciate his flexibility this Fall.

I would also like to thank those who helped me throughout my research at the University of Michigan. When I joined Prof. Guo's group, Yichun Zhang and Dr. Kaito Yamada were my first mentors. Yichun patiently taught me how to use the photoacoustic setup, answering questions long after I took over. Dr. Yamada taught me the principles of physics simulations in

COMSOL, as well as cleanroom protocol. Thank you to Dr. Jorge Barreda for his mentorship while learning nanofabrication, he taught me many techniques that I still use. I want to acknowledge Matt Oonk and Dennis Schweiger for their help, knowledge, and suggestions while building the custom evaporator. I also want to thank Mira Diab El Harakeh for her support during our collaboration and for answering many questions. I would also like to thank Dr. Tae Cho for his assistance when writing my first paper, he provided great support when I was unsure. I want to thank Dr. Sarah Seva for her optimism and device expertise during our collaboration. Lastly, I'd like to thank Daniel Penley for his support. He helped me design a new printing setup as well as aided me take great microscope images for my structural color paper.

Throughout the PhD, I was supported by the Guo group as well. I want to thank our former members: Dr. Taehwa Lee, Dr. Saurabh Acharya, Dr. Yongbum Park, Dr. Sungho Lee, Dr. Haozhu Wang, Dr. Wei-Jie Feng, Dr. Weikuan Lin, Dr. Taigao Ma, Dr. Jennie Paik, and Dr. Boonjae Jang for helping me and answering many questions, as well as providing interesting research of their own. I also want to thank the current group members: Anwesha Saha, Yian (Evan) Cheng, Dijia Zou, Mohammad Ali Kazmi, Hyeonwoo Kim, and Lingyue Zhu. Thank you all for your support and I will remember our time together always. The future of the group is in bright hands.

I especially want to thank my Applied Physics cohort: Andrea Londono, Anwesha Saha, Ariana Bueno, Chris Ayala, Freddy Cisneros, Isak Johnson, Jacob Waelder, Khalil Bryant, Kwyn Kelso, Laila Hayani, Michael Springstead, Nicholas Ernst, Dr. Saaj Chattopadhyay, Wendy Lyu, and Zach Croft. In addition, my Applied Physics roommates, Dr. George Dowhan and Brendan Stassel. You all are my family and I cannot express how important you were and are to my PhD experience. Thank you.

Thank you to my Gustavus Physics professors for their inspiration and guidance that led me to pursue a PhD. Professor Chuck Niederriter was my academic advisor and an incredible role model. Professor Tom Huber was my ultrasound research advisor and a great support. Thank you also to Professor Jessie Petricka, Professor Paul Saulnier, and Professor Darsa Donelan for their expertise, wisdom, and care for their students. Lastly, thank you to Professor Steve Mellema and Shirley for their love and support for my whole life. Mel has always encouraged me to ask questions and learn, and he is an enormous influence on my academic career. In addition, thank you to Professor Jim Kakalios, my summer research advisor at the University of Minnesota, for introducing me to nanomaterials and thin film characterization. These skills and research fostered my own PhD work, and I remember my time with his group fondly.

Thank you to all my teachers in school, they developed me into the person I am today. Katie Botten first encouraged me to pursue architecture and engineering, and she had an incredibly positive impact on my curiosity and confidence. Jerry Burkhart taught me to think about advanced mathematics in creative ways. John Lawton taught me to be patient and kind, even in science. Jon Graff taught me life sciences and to appreciate our ecosystems. Joe Broze taught me to be creative and informed when studying geography, and to persevere when reaching for my goals. Matt Moore taught me how to research historical information and to critically think about history. Scott Urban taught me that government and history can be incredibly exciting, and to always believe in your students. Kristine Barnes taught me to be expressive and the importance of learning about other cultures. Mark Szybnski taught me to enjoy chemistry, and he always knew how to make students laugh. Mark Zenk taught me the fundamentals of engineering and to focus on problems that need solving. Lastly, Eric Koser introduced me to physics with enthusiasm and exemplified how to explain difficult concepts in understandable ways.

Next, I want to thank my support system throughout my PhD experience. Thank you to my cousins Rory, Kjersa, Joe, and Michael for their incredible humor and support. Our DnD sessions have been a perfect way to stay connected and to think creatively. Thank you to my friends Adam, Tanner, Garrett, Akira, Ash, Chris, Jim, and Charlie for the great memories and laughter throughout the years. I can always count on them to turn my day around. Thank you to Ma, Baba, and Jui for their words of affirmation and laughter. These years have been very difficult for us, and I am so happy that we are able to support each other.

Last and most importantly, I want to express my deepest appreciation for my family. Thank you to my parents, Nancy and Mark, for your love and support, even while I am across the country. You have always encouraged me to follow my dreams, and I can't thank you enough. Thank you to my sister, Amanda, for your love and ability to always make me laugh. Thank you also to my brother-in-law, Ryan, and my niece and nephew, Ella and Aiden, for supporting me and being an amazing family. Thank you to Aunt Patricia for reading most of this thesis and for being so giving. Lastly, I am so lucky to have found my life partner during my PhD. She is a rock during all the stressful times, she is the funniest person I have ever met, and she is so beautiful. Shiuli, you are the best and I love you.

Table of Contents

Dedication ii

Acknowledgements iii

List of Tables xii

List of Figures xiii

List of Appendices xvi

Abstract xvii

Chapter 1 Introduction and Overview of Structural Color and Additive Manufacturing 1

1.1 Background on Color and Structural Color 1

1.1.1 Importance of Color in Material Science and Manufacturing 1

1.1.2 Structural Color vs Pigment-Based Color 2

1.2 Fundamentals of Color Theory and Quantification 4

1.2.1 Color Perception 4

1.2.2 Quantifying Color: The CIEXYZ Color Space 5

1.2.3 Quantifying Color: The CIELAB Color Space 6

1.2.4 Quantifying Color: Reflection Spectra and Chroma 8

1.3 Mechanisms for Achieving Structural Color 13

1.3.1 Introduction to Structural Color Mechanisms 13

1.3.2 High-Low-Absorber (HLA) and Metal-Dielectric-Metal (MDM) Structures 14

1.4 Thesis Outline 19

1.4.1 Innovations in Additive Manufacturing for Functional Coatings 19

1.4.2 Advanced Additive Techniques for Printed Electronics 20

Chapter 2 Harnessing Natural Minerals for Structural Colors 21
2.1 Introduction to Structural Colors from Natural Minerals 21
2.1.1 Motivation for Using Abundant Minerals in Structural Colors 21
2.2 Fundamentals of High-Low-Absorber (HLA) Structures for Structural Color 22
2.2.1 Overview of the HLA Structure 22
2.2.2 Comparison to MDM 23
2.3 Selection and Processing of Raw Minerals for Structural Colors 24
2.3.1 Choosing Suitable Minerals for Each Layer in HLA 24
2.3.2 Preparation and Processing of Minerals 25
2.4 Deposition and Characterization of Mineral-Based Structural Color Films 26
2.4.1 E-Beam Evaporation Mechanism 26
2.4.2 Changes in Material Composition During E-Beam Evaporation 29
2.4.3 E-Beam Evaporation of Mineral-Based Films 30
2.4.4 Characterization Techniques for Structural Color Films 32
2.5 Results: Optical Properties and Color Quality of Mineral-Based Films 32
2.5.1 Cost-effective Coatings with SiO_2 and TiO_2 Films 32
2.5.2 SiO_2 Distillation with E-beam Evaporation 34
2.5.3 Optical Performance of TiO_2 Films 36
2.5.4 Performance of Absorbing Layers from CuO and Fe_2O_3 37
2.5.5 XPS Analysis of Metal Oxide Films 39
2.5.6 High-Chroma Color with Abundant Minerals 42
2.6 Cost and Environmental Benefits of Mineral-Based Structural Colors 43
Chapter 3 Advanced Structural Color Applications 45
3.1 Introduction to Advanced Structural Color Applications 45
3.2 Structural Black 46

3.2.1 Piano Black in Industry 46
3.2.2 Overview of the DMDM Structure 47
3.2.3 Deposition and Characterization of Structural Black Films 47
3.3 Thermochromic Structural Color Coatings 48
3.3.1 Overview of Thermochromic Coatings 48
3.3.2 Overview of the Thermo-Optic Effect 49
3.3.3 Deposition and Characterization of Thermochromic TiO_2 Films 50
3.3.4 Thermal Sensing with Thermochromic Structural Colors 51
3.4 Glass Fusing Structural Color Films 55
3.4.1 Overview of Glass Fusing 55
3.4.2 Spin Coating and Fusing Structural Color Flakes 56
Chapter 4 Patterning and Conformal Coatings with Area-Selective Atomic Layer Deposition ...58
4.1 Introduction to Conformal Coatings and Patterning Techniques 58
4.1.1 Overview of Atomic Layer Deposition and Conformal Coatings 58
4.1.2 Importance of Patterning in Structural Color Applications 59
4.1.3 Principles of AS-ALD and E-Jet Printing 60
4.2 Materials and Process Parameters in AS-ALD for Structural Colors 61
4.2.1 Materials Selection for Multilayer Structural Color Coatings 61
4.2.2 Process Parameters and Control in ALD 62
4.3 Deposition of Conformal Structural Colors with ALD 63
4.3.1 Planar MDM Structures with ALD 63
4.3.2 Conformal Structural Colors on Metal 3D-Printed Objects 66
4.4 Techniques for Patterning Structural Colors with AS-ALD 68
4.4.1 Patterning with Polymer Inhibitors in AS-ALD 68
4.4.2 Patterning Polymer Inhibitors with E-jet Printing 71

4.5 Characterization and Evaluation of ALD-Coatings 73
4.5.1 Optical and Structural Characterization of AS-ALD Coatings 73
4.5.2 Assessing Color Durability in Conformal Coatings 74
4.6 Brief Overview of SALD and Its Potential for High-Throughput Coating 77
4.6.1 Introduction to Spatial ALD (SALD) for High-Throughput Coating 77
4.6.2 High-Throughput Characterization of Film Thickness 77
Chapter 5 Printing Thin Film Transistors with Shock-wave Jet Printing 79
5.1 Introduction to Carbon Nanotubes (CNTs) in Electronics 79
5.1.1 Overview of Printed Electronics 79
5.1.2 Challenges in Traditional CNT Printing Methods 80
5.2 Fundamentals of Shock-wave Jet Printing (SJP) for CNTs 82
5.2.1 Principles of SJP 82
5.2.2 Advantages of SJP for CNTs 84
5.3 SJP Setup and Process Parameters 85
5.3.1 Overview of the SJP Mechanism and Equipment 85
5.3.2 Process Parameters and Optimization 86
5.4 Printing CNT Transistors with SJP 86
5.4.1 Design and Fabrication of CNT Transistor Structures 86
5.4.2 Morphological Comparison of IJP and SJP Devices 87
5.4.3 Electrical Comparison of IJP and SJP Devices 89
5.4.4 Printing Unsonicated Ink with SJP 95
5.5 Characterization and Performance of SJP-printed CNTs 96
5.5.1 Compositional and Structural Characterization 96
5.5.2 Electrical Performance and Reliability Testing 98
Chapter 6 Shock-wave Jet Printing of Solid Functional Materials 101

6.1 Introduction to Solid-State Printing and Functional Materials 101
6.1.1 Overview of Functional Solid Materials in Advanced Manufacturing 101
6.1.2 Challenges in Traditional Printing of Solid Materials 102
6.2 Fundamentals of Shock-wave Jet Printing for Solid Materials 103
6.2.1 Mechanism of Solid Material Ejection via Shock-wave Jet Printing 103
6.2.2 Advantages of SJP for Solid-State Materials 104
6.2.3 Selection of Functional Materials for SJP 105
6.2.4 Challenges and Techniques in Printing Organic Molecules 106
6.3 Case Study: Printing of Organic Molecules and Crystals 107
6.3.1 Morphological Characterization of Printed Solid Materials 107
6.3.2 Optimization of Solid Printing Patterns 108
Chapter 7 Conclusion and Future Work 111
7.1 Summary of Key Findings 111
7.2 Future Research Directions 113
Appendices 116
Bibliography 126

List of Tables

Table 1. Calculated chroma values for each structure shown in Figure 6. 12

Table 2. Calculated hole mobility values ($cm^2/V.s$) using *Eqn. 5-2* for different percolating paths. 92

List of Figures

Figure 1. Structural colors in nature including a) peacock feathers, b) Pollia condensata berries, and c) Tansy beetles. 2

Figure 2. Standard color gamuts used for digital displays and printing inks. 4

Figure 3. The CIE 1931 standard observer. Image adopted from ref. 38. 5

Figure 4. CIEL*a*b* perceptually uniform color space. Credit to Ultra Metal Finishing <https://www.umfcorp.com/post/understanding-the-cielab-l-a-b-scale>.\ 7

Figure 5. Structural color and chroma. TiO2 and SiO2 thicknesses ranged from 0 to 400 nm with the stack color shown in a) and the stack chroma shown in b). Three high-chroma areas were selected, and their reflection spectra are shown in c), d), and e). Chroma values were calculated based on CIELAB coordinates. 10

Figure 6. Reflection spectra of a) green and b) magenta structural colors. The calculated CIELAB values are included in c) and d), respectively. 11

Figure 7. Light propagation and absorption in a) MDM and b) HLA structures. 16

Figure 8. Absorption and electric field intensity in an HLA structure for a-c) first-order resonance and d-f) second-order resonance. 17

Figure 9. Phase analysis of a) first-order and b) second-order resonance light in an HLA cavity. 18

Figure 10. The Ellingham diagram for metal oxides. Relevant reactions are highlighted. Image adopted from Ref. 75. 28

Figure 11. High-chroma, planar HLA coatings with varying cavity thicknesses. Optical microscope images, reflectance spectra, and calculated CIELAB coordinates are included. 33

Figure 12. a) Refractive indices of SiO_2-containing minerals. b) and c) show blue topaz before and after deposition, respectively. 34

Figure 13. Refractive index data for TiO_2 films. 36

Figure 14. Refractive indices of evaporated absorbing films. 38

Figure 15. XPS spectra for the CuO, Fe_2O_3, Fe_3O_4, and mixture films. 40

Figure 16. High-chroma HLA coatings from abundant minerals with a metallic copper oxide absorbing film. 43

Figure 17. Structural black using the DMDM structure. Reflection spectra for a) visible wavelengths and expanded to b) ultraviolet wavelengths indicate near-zero visible reflection... 48

Figure 18. The thermo-optic effect in thick TiO_2 films. a) Camera images, b) refractive index data, c) measured reflectance spectra, and d) simulated reflectance spectra. 51

Figure 19. Color change in thick TiO_2 films, adjusted by tuning the SiO_2 layer thickness, between room temperature (RT) and 100 °C. 52

Figure 20. Thermochromic TiO_2 coatings used as temperature sensors. a) and b) show the temperature shift in two HLA structures with varying SiO_2 cavity thicknesses. c) is a camera image of the sample in b). d) and e) exhibit color change based on Joule heating..... 53

Figure 21. Clear glaze film a) before and b) after firing at 700 °C. c) Color flakes fused to clear glaze film. 56

Figure 22. a) Cross-sectional SEM image of a deposited MDM structure and b) a schematic representation. 62

Figure 23. a) Structural colors produced by planar MDM stacks with varying ZnO thicknesses, including measured and simulated reflectance spectra. b) RGB values plotted on a chromaticity diagram. c) Reflection peaks and d) valleys as a function of ZnO thickness. 64

Figure 24. a) 3D-printed metal objects coated with MDM structures, including uncoated (left), 80 nm ZnO (middle) and 120 nm ZnO (right) samples. b-c) Optical microscopy images showing surface details. 67

Figure 25. Conformal ALD coatings including a-d) SEM images of trench coatings and e-f) MDM coatings on curved glass and polyimide. 68

Figure 26. a-f) Process Flow for Patterning Block “M” structure with Area-Selective Atomic Layer Deposition..... 69

Figure 27. Patterned structural color coating with AS-ALD including a a) schematic and b) optical microscope image. c) AFM step analysis and d) XPS Zn characterization confirm difference in composition between masked and unmasked areas. 70

Figure 28. Structural color patterning with e-jet printing and AS-ALD, including a a) schematic process flow and b-d) optical microscope images. 72

Figure 29. Thermal stability of blue and yellow wolverine figurines in ambient air at 300 °C. Both figurines were coated with a protective anti-reflective Al_2O_3 layer. 75

Figure 30. Measured reflectance spectra for planar a-b) MDM and c-d) DMDM structures during 300 °C baking, demonstrating a higher DMDM endurance. 76

Figure 31. Histogram of CNT length in purchased CNT ink, provided by NanoIntegris Inc. 82

Figure 32. SJP printing setup including a) CNT transistor schematic, optical microscope images of b) IJP and c) SJP devices, and d) SJP schematic. 83

Figure 33. a-b) SEM and c-d) AFM images of IJP-printed (left) and SJP-printed (right) CNT TFTs. 88

Figure 34. A schematic of simple CNT networks and effective mobility parameters. 92

Figure 35. a-b) Transfer characteristics of the CNT-TFT devices for a drain bias of 1V. c-e) Id-Vd family plots. 93

Figure 36. SEM images of representative CNT networks printed by a) IJP (10 passes) and c) SJP (1 print pass). False colored versions are included in b) and d) to extract surface coverage. 94

Figure 37. Raman spectra of sonicated ink, as well as IJP and SJP-printed devices. 97

Figure 38. Magnified SEM images of a) 10 print pass IJP channel and b) one print pass SJP channel. 98

Figure 39. a) $ION/IOFF$ with respect to mobility for both printer types. b) Mobility and c) log ($ION/IOFF$) versus channel length for various printing tests 99

Figure 40. The SJP experimental setup with a thin transfer layer (orange). 103

Figure 41. DPP8 molecule in its amorphous, supercooled liquid (left) and crystalline (right) states. 105

Figure 42. SJP-printed 600 μm “L” patterns for three transfer layers. 107

Figure 43. Fluorescence of printed DPP8 molecules, demonstrating crystallization along the transfer layer base (bottom right). 108

Figure 44. Crystalline DPP8 patterns for two different travel distances. 109

Figure 45. SJP-printed amorphous DPP8 on four glass coatings. 110

Figure 46. Exterior of the custom-built evaporator chamber. 116

Figure 47. Vacuum and water-cooling system of the custom-built evaporator. 117

Figure 48. Interior of the custom-built evaporator chamber. 118

Figure 49. Controllers of the custom-built evaporator. 119

Figure 50. Optics of the SJP system. 121

Figure 51. PA capsule and shadowgraph lens of the SJP system. 122

List of Appendices

Appendix A: The Custom-Built Evaporator Setup.....116

Appendix B: The Shock-wave Jet Printing Setup and TFT Device Fabrication.....121

Abstract

Advances in additive manufacturing have revolutionized the fabrication of functional photonic and electronic materials, offering sustainable solutions for vibrant structural color coatings and high-performance printed electronics. This thesis explores innovative strategies for integrating abundant natural minerals and advanced printing techniques to create durable, cost-effective materials for versatile applications.

The fundamentals of structural color theory and their application to simple, vibrant thin-film stacks are presented, supported by simulations and interference calculations to understand the physical mechanisms of these designs. High-Low-Absorber (HLA) and Metal-Dielectric-Metal (MDM) structures are examined as foundational designs for high-chroma coatings, demonstrating the potential of interference-based methods for achieving intense, environmentally stable colors.

HLA structures were developed using minimally processed minerals, such as rutile-derived TiO_2 and silica-based SiO_2, to produce scalable, tri-layered coatings with significant reductions in material costs and environmental impact compared to traditional pigment-based coatings. A novel metallic copper oxide absorber film was fabricated using a mixture of iron oxide and copper oxide mineral powders, showcasing a sustainable approach to color production. Additionally, this work discusses repeatability and best practices for electron-beam evaporation of mineral powders to ensure consistent coating performance.

The utility of structural color coatings is extended to advanced applications, including optical sensing and decorative technologies. Thermochromic TiO_2 coatings exhibit viable temperature-sensing capabilities, suitable for integrated optics circuits. Glass fusing techniques create robust structural colored glass for decorative purposes, while structural black coatings provide durable, low-reflection finishes for aesthetic and functional applications.

Area-selective atomic layer deposition (AS-ALD) was used to achieve precise patterning and conformal deposition of structural colors, enabling vibrant, uniform coatings on complex 3D-printed objects. Microscale multi-color patterns were also created with AS-ALD, offering scalable, high-resolution optical designs. The integration of Spatial ALD (SALD) to enhance film uniformity and throughput is also discussed.

In the realm of electronics, a novel photoacoustic printing method, Shock-wave Jet Printing (SJP), addressed limitations in traditional printing methods, such as nozzle-clogging and material degradation. SJP enabled high-resolution deposition of carbon nanotubes (CNTs) for thin-film transistors, achieving competitive effective mobilities compared to conventional inkjet printing. The effective mobility of percolating CNT networks was analyzed, providing insights into device performance.

SJP was further demonstrated for solid-state printing of organic molecules, preserving material integrity while achieving high-resolution patterns critical for optoelectronics and sensing applications. Emissive organic molecules were successfully deposited in microscale patterns, showing the potential of SJP for processing materials incompatible with traditional techniques.

Together, these findings establish a synergistic framework for additive manufacturing of structural colors and electronics, utilizing abundant raw materials and advanced fabrication techniques to address both aesthetic and functional demands. This work sets the stage for future studies in sustainable photonics and printed electronics, advancing the field toward scalable, cost-effective, and environmentally conscious manufacturing processes.

Chapter 1 Introduction and Overview of Structural Color and Additive Manufacturing

1.1 Background on Color and Structural Color

1.1.1 Importance of Color in Material Science and Manufacturing

Color is an incredibly important aspect of our interpretation of our surroundings. It is so significant that one of the primary expressions of human emotion is through the use of color in visual media. Everywhere you look, vivid natural or artificial colors are designed to capture your attention. Examples include the harsh reds on stop signs, the soothing blues on packaging, and the vibrant yellows of flowers. For those fortunate enough to experience color, the world is vastly enhanced by its presence.

In our modern world, filled with advanced manufacturing and marketing, color is more important than ever in enhancing the aesthetics of new products. For example, buildings are adapting smart windows and decorative solar panels to enhance visual appeal.[1,2] Personal phones also require increasingly vivid color displays and cases.[3]

Other areas, which have relied on color throughout their entire existence, continue to show room for improvement. For instance, house paints fade over time and must be refreshed every couple of years. The colors of cloth materials also fade over time due to UV absorption and oxidation. Therefore, it is imperative to develop color coatings that are vibrant, long-lasting, and environmentally resistant for functional purposes.

Additive manufacturing (AM) is a growing field that offers numerous solutions to these issues.[4–7] Also known as 3D printing, additive manufacturing involves building structures layer

by layer, often using polymer materials deposited by a printer head.[8,9] Other techniques achieve much higher resolution, creating photonic and electronic devices through the stacking of layers.[10]

1.1.2 Structural Color vs Pigment-Based Color

Structural color refers to the use of nanoscale structures that resonate with visible wavelengths of light. Some well-known examples are shown in Figure 1, demonstrating peacock feathers, berries, and beetle wings. Structural colors can be made with inorganic materials, making them inert and environmentally stable.[11,12] They are in direct contrast to organic pigments, which are microscale particles that absorb some wavelengths of light and scatter the rest.[13] However, the molecular bonds in organic pigments are easily damaged by UV light and environmental stresses.[14]



Figure 1. Structural colors in nature including a) peacock feathers, b) Pollia condensata berries, and c) Tansy beetles.

There are many methods to create structural color, including but not limited to thin film interference, diffraction gratings, photonic crystals, and plasmonic resonances.[4,15–29] A simple structural color method uses thin film stacks, which create color by confining resonant wavelengths in an optical cavity.[4,30,31] Vibrant colors are possible with only three layers, making thin film stacks a simple application that can be integrated with additive manufacturing.[4]

This work utilizes structural color in innovative and sustainable ways. Vivid colors are produced using abundant mineral source materials instead of high-purity ones, which reduces manufacturing costs and improves environmental impact.[32] Colors are also patterned through area-selective atomic layer deposition, a form of additive manufacturing capable of creating colored patterns that conform to irregular surfaces.[4] The addition of a top dielectric anti-reflection coating further enhances the color of these conformal coatings, protecting the color stack even when baked at 300 °C for 15 hours

One important stack design in this work is the High-Low-Absorber (HLA) structure, discussed further in section 1.3.2.[30,32,33] This structure contains three dielectric films with different optical behaviors, achieving high chroma without the need for expensive metal layers. Additionally, using three distinct types of thin films helps the development of a large database of thin film behaviors, which is useful for machine-learning design.[34]

To fabricate these structures at scale and on complex surfaces, advanced additive manufacturing techniques are indispensable. AM enables precise nanoscale fabrication, essential for vibrant, stable structural colors. It also allows unparalleled flexibility in patterning and deposition, as demonstrated by techniques like area-selective atomic layer deposition (AS-ALD) and photoacoustic printing, which produce detailed patterns and conformal coatings on 3D-printed parts.

By employing the use of abundant, minimally processed minerals, AM reduces costs and environmental impact compared to traditional high-purity materials. Together, these advantages make AM a transformative platform for structural color coatings, combining functionality and sustainability. These synergies are central to this thesis, addressing important challenges in creating durable, cost-effective, and versatile color coatings.

1.2 Fundamentals of Color Theory and Quantification

1.2.1 Color Perception

Human eye cones are sensitive to three sections of the visible spectrum and the brain calculates a color based on the cone signal intensities.[35] These sections are known as Red, Green, and Blue (RGB). Display pixels create color by adjusting small RGB LEDs. Digital displays combine these three colors in various amounts, forming a color gamut.[36–38] This gamut covers a wide range of colors perceivable to humans, the wider the gamut, the more colorful the display. To achieve a large gamut, high color purity is needed.

In Figure 2, two standard color gamuts are shown, Adobe and sRGB.[37,38] sRGB is the standard gamut used for digital displays, where the red, green, and blue LED color purity is represented by the corners of the gamut. The further from the middle, the purer the color. Adobe has a larger gamut and thus has a wider range of perceptible colors. These gamuts are overlaid on a chromaticity plot, which will be explained in section 1.2.2.

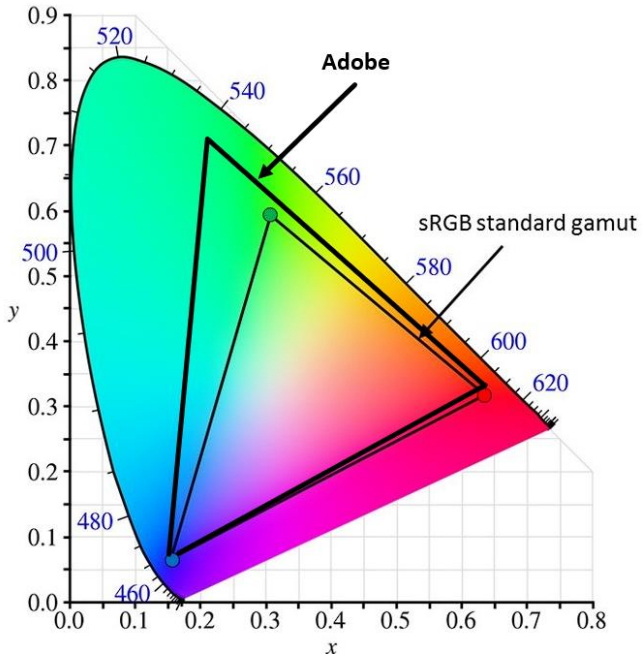


Figure 2. Standard color gamuts used for digital displays and printing inks.

1.2.2 Quantifying Color: The CIEXYZ Color Space

Color is an optical response of the brain and can vary between individuals and species, making it a unique sense to each organism. Comparisons between individuals may result in conflicting perceptions. To understand the true color of any object, we must study its reflection spectrum. The reflection spectrum shows the percentage of incident light reflected at each wavelength. It provides an unbiased visible response that can be analyzed and converted to a color representation. Established conversions were determined by the CIE (Commission Internationale de l'éclairage) in 1931 for xyz and again in 1976 for Lab.[39,40] In 1931, the CIE created the standard observer to represent the average optical response of a human eye, shown in Figure 3.[41]

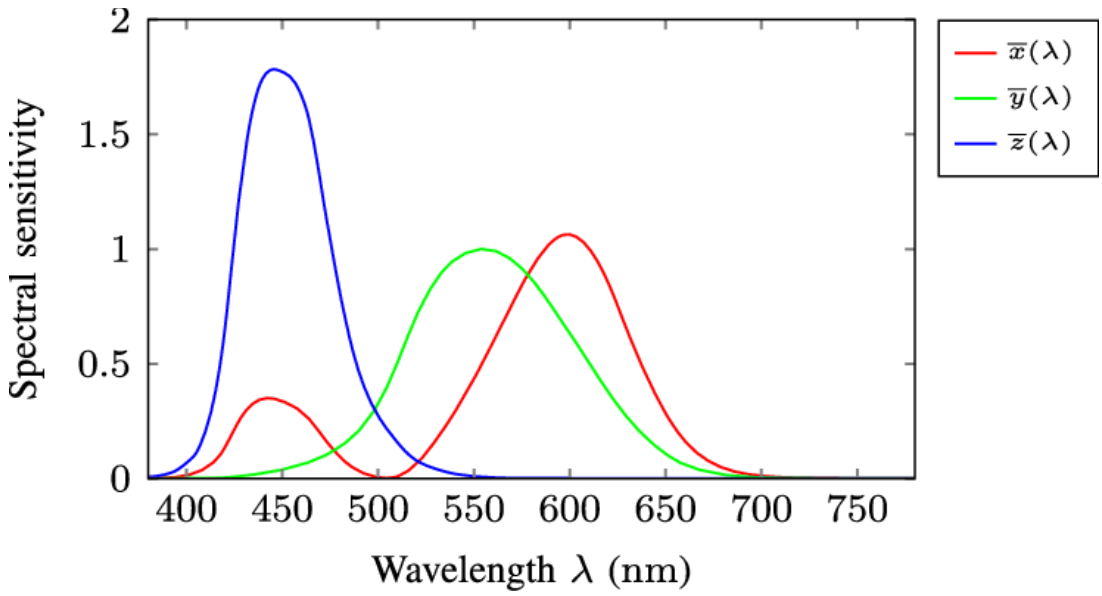


Figure 3. The CIE 1931 standard observer. Image adopted from ref. 38.

The standard observer contains three color matching functions that are used to create tristimulus values: X, Y, and Z:

$$X = \int R(\lambda)I(\lambda)\bar{x}(\lambda)d\lambda$$

$$Y = \int R(\lambda)I(\lambda)\bar{y}(\lambda)d\lambda$$

$$Z = \int R(\lambda)I(\lambda)\bar{z}(\lambda)d\lambda$$

Eqn. 1-1

$R(\lambda)$ is the reflection spectrum, $I(\lambda)$ is the power spectrum of the illumination source, and $\bar{x}(\lambda)$ is the color matching function from the 1931 standard observer. Tristimulus values from *Eqn. 1-1* are then normalized and used to map color on a chromaticity plot like in Figure 2. These normalized color coordinates can also be converted to rgb values to approximate color with display pixels.

1.2.3 Quantifying Color: The CIELAB Color Space

In color spaces, color is usually separated into three categories: brightness, hue, and chroma. The typical chromaticity plot does not account for brightness, only hue and chroma. Chroma is the measure of color purity independent of the background illumination. The 1931 color space is not perceptually uniform, though, meaning the chroma does not uniformly change with hue. In 1976 the CIE created Lab, a perceptually uniform color space.[42] This space is determined by three variables, L*, a*, and b*, as shown in Figure 4. L* is the brightness and varies from 0 to 100; a* lies on the red-green chroma axis, and b* lies on the blue-yellow chroma axis. a* and b* values can vary from -128 to 128; the origin has no color purity while the edges have maximum color purity. With this color representation, we can determine the chroma,

$$C^* = \sqrt{a^{*2} + b^{*2}},$$

Eqn. 1-2

and quantify the color purity of an object.

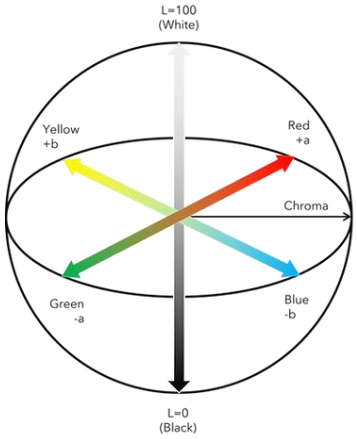


Figure 4. CIEL*a*b* perceptually uniform color space. Credit to Ultra Metal Finishing <https://www.umfcorp.com/post/understanding-the-cielab-l-a-b-scale>.\

CIELAB is based on opponent process theory, in which cones are paired.[43,44] The brain reads differences between the Long and Medium cone signals as well as the difference between the Medium and Short cones. These comparisons are represented in CIELAB as the red-green axis and blue-yellow axis. Colorblindness is caused by a defect with one of these signals. CIELAB has multiple process steps to convert tristimulus values, XYZ, to a circular, perceptually uniform color space, shown in *Eqn. 1-3*.[40]

$$L^* = 116\, f\left(\frac{Y}{Y_N}\right) - 16$$

$$a^* = 500\, (f\left(\frac{X}{X_N}\right) - f\left(\frac{Y}{Y_N}\right))$$

$$b^* = 200\, (f\left(\frac{Y}{Y_N}\right) - f\left(\frac{Z}{Z_N}\right))$$

where t is $\frac{X}{X_N}$, $\frac{Y}{Y_N}$, and $\frac{Z}{Z_N}$,

$$f(t) = \begin{cases} \sqrt[3]{t} & if\ t > \delta^3 \\ \frac{t}{3\delta^2} + \frac{4}{29} & otherwise \end{cases}$$

$$\delta = \frac{6}{29}$$

Eqn. 1-3

X_N, Y_N, and Z_N are reference illuminations, common values are D50 and D65, representing horizon daylight and noon daylight respectively.[45] In this color analysis, tristimulus values, X, Y, and Z, are cube rooted to approximate human eye cone sensitivity to light. At low brightness ($t < \delta^3$), the cube root breaks down and a linear approximation is used. L* is calculated directly from the Y value, which represents the green eye cone. a* and b* values are calculated by the difference in tristimulus values, representing opponent process theory. The constants in *Eqn. 1-3* were empirically determined by the Adams-Nickerson formula and a 1976 CIE subcommittee.[46] Adams and Nickerson determined a scaling ratio for L*, a*, and b* which produced a circular, perceptually uniform color space. The CIE subcommittee then determined the constants in *Eqn. 1-3* by multiplying the Adams-Nickerson formula constants by the cube root expression constants, then scaling by 0.91 so the maximum L* value is 100. The result is a perceptually uniform color space that can be thought of in cylindrical coordinates. Z is brightness, ρ is chroma, and φ is hue. CIELAB follows opponent process theory, representing color by comparing sections of the visible spectrum.

1.2.4 Quantifying Color: Reflection Spectra and Chroma

Is there a way to directly determine chroma from the reflection spectrum? Qualitatively, Endler claims that a high chroma corresponds to a steep reflection peak slope and a large difference between sections of the spectrum.[47] This can be interpreted as tall, narrow reflection peaks with low background reflection. However, such a spectrum is difficult to create with subtractive color. Simple vibrant structural color coatings rely on destructive interference due to phase cancellation. The vibrant structures are designed so that the propagating electric field is maximized in the absorbing layers at destructive resonant wavelengths, yielding strong

absorption peaks.[11,12,25] Since the substrates are optically thick, negating transmission, strong absorption peaks also mean strong reflection valleys. If chroma is indeed tied to reflection peaks, we must understand how reflection valleys can influence the shape of reflection peaks in the visible spectrum.

One example of high chroma color coatings is a tri-layer stack designed with a silicon substrate absorber, silica low index layer, and titania high index layer as shown in Figure 5a. The stack reflection spectra were simulated with the transfer matrix method (TMM) and measured refractive indices. As the dielectric layer thicknesses were surveyed, the reflection spectra were converted to rgb values and plotted in Fig 5a. The spectra were also converted to CIELAB coordinates and chroma values using *Eqns. 1-1*, *1-2,* and *1-3*, indicating three chroma hotspots when adjusting the dielectric layers' thicknesses, shown in Fig. 5b. These high chroma reflectance spectra are shown in Fig 5c-e. The lowest order resonance in Fig 5c has the highest chroma, near the maximum value. The second order resonance in Fig. 5d and 5e have slightly lower, nearly equal chroma values.

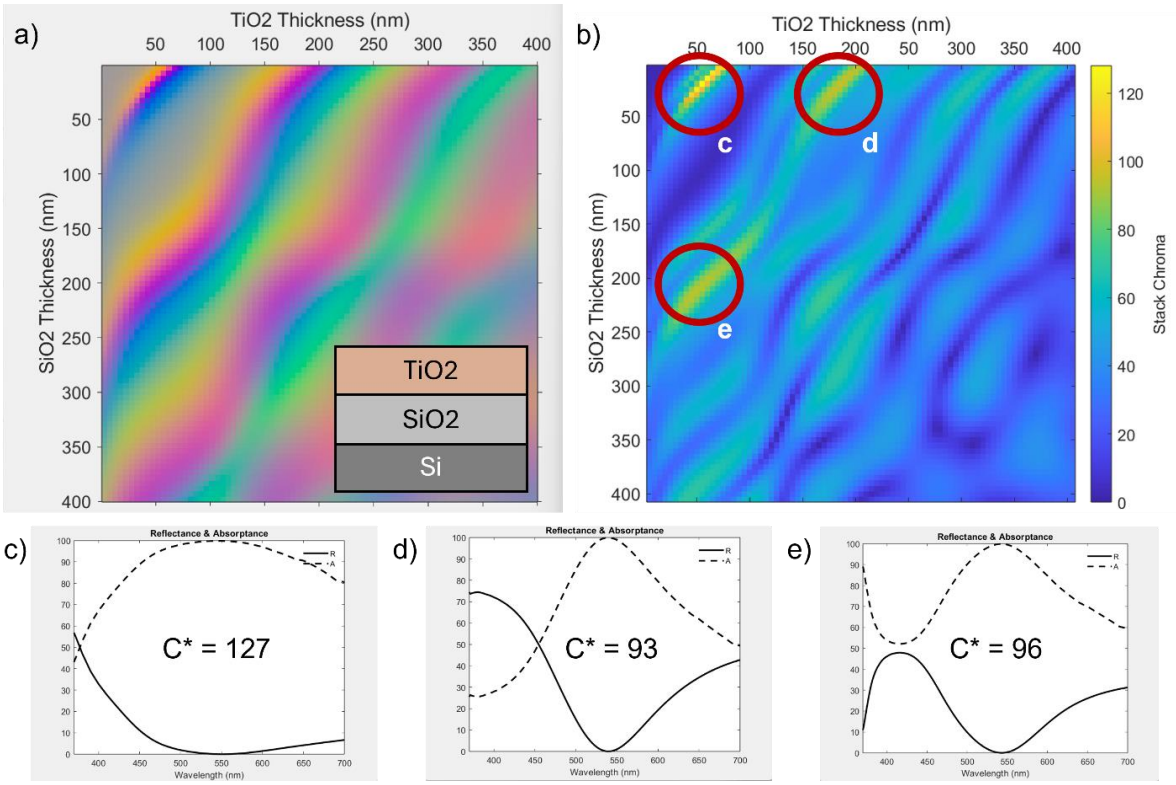


Figure 5. Structural color and chroma. TiO2 and SiO2 thicknesses ranged from 0 to 400 nm with the stack color shown in a) and the stack chroma shown in b). Three high-chroma areas were selected, and their reflection spectra are shown in c), d), and e). Chroma values were calculated based on CIELAB coordinates.

These results reveal important information about the relationship between reflection valleys (absorption peaks) and chroma. With each increasing resonance order, the reflection spectra features become narrower. For example, the lowest order absorption peak in Fig. 5c is much broader than the first order peaks in Fig. 5d and 5e. As a result, when the layer thicknesses are appropriate, the broad reflection valley of Fig. 5c results in a sharp reflection peak of purple light. The sharp reflection peak and low background reflection results in a great chroma. Fig. 5d and 5e have lower chroma than Fig. 5c due to broader reflection peaks. Although they have different peak amplitudes, they have nearly the same chroma. The relationship between peak shape and chroma likely relies on peak width, requiring further investigation.

Twelve simple tri-layer structural color coatings were simulated and plotted in Figure 6, six with reflection peaks at 550nm and six with reflection valleys at 550nm. The valleys and peaks were located at 550nm because it is the middle of the visible spectrum. Two material choices were used for the substrate, silicon and nickel, and two were used for the top layer, TiO_2 and copper. The L*a*b* values for each of these spectra were calculated with *Eqn. 1*-3 and plotted in Fig. 5c-d, showing linear trends for all coordinates. Chroma was calculated for each structure using *Eqn. 1-2*, included in Table 1.

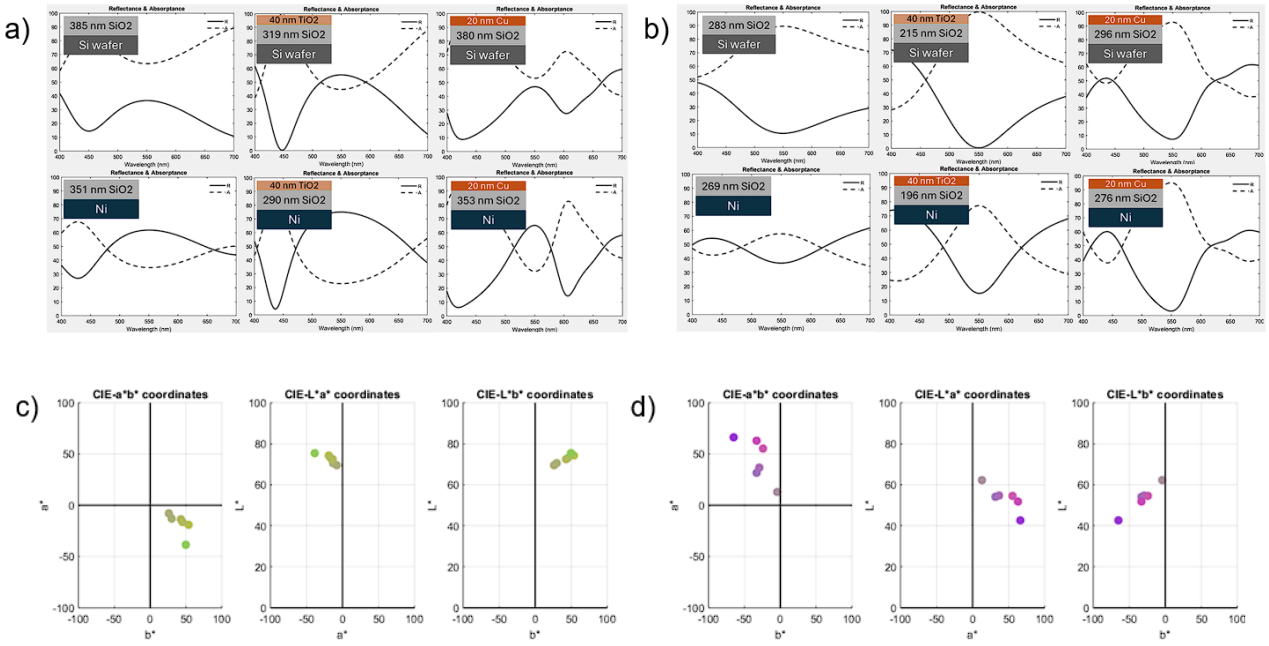


Figure 6. Reflection spectra of a) green and b) magenta structural colors. The calculated CIELAB values are included in c) and d), respectively.

Table 1. Calculated chroma values for each structure shown in Figure 6.

Coating	**Green Chroma**	**Magenta Chroma**
SiO_2/Si	45.7	32.7
SiO_2/Ni	13.6	27.3
TiO_2/SiO_2/Si	92.8	56.9
TiO_2/SiO_2/Ni	46.9	45.0
Cu/SiO_2/Si	60.3	47.9
Cu/SiO_2/Ni	71.1	62.9

From Table 1, the structures with the highest chroma were TiO_2/SiO_2/Si and Cu/SiO_2/Ni structures. This supports previous findings that HLA and Metal-Dielectric-Metal (MDM) are high color purity structures.[4,30,32,33,48] The HLA and MDM spectra in Figure 6 have narrow reflection peaks with low background reflection. This result agrees with Endler's assessment.[47] From Feng 2023, the largest resonances occur when the radiative loss equals the absorptive loss.[30] Thus, for a reflective Ni substrate, a highly absorbing thin Cu layer balances the losses. The Si substrate is already a good absorber, so the top reflection layer does not need additional absorption, making TiO_2 a suitable choice. Furthermore, we can see from both HLA (TiO_2/SiO_2/Si) structures in Fig. 6 that reflection valleys reach zero reflection, indicating great resonance.

1.3 Mechanisms for Achieving Structural Color

1.3.1 Introduction to Structural Color Mechanisms

As discussed previously, there are various methods to create color with structures. Thin film interference, for instance, allows for the tuning of color hues by changing the thickness of the cavity layer. The incorporation of reflective and absorptive layers enhances the resonance created within the cavity. Photonic crystals, which exhibit period variations in refractive index, are another approach to structural color generation.[15,49–51] Color-changing photonic crystals can be achieved with block structure polymers.[52,53] Diffraction gratings, consisting of thin, parallel lines, control optical resonance through their spacing.[11,12,18] These gratings are typically made using photolithography, which adds complexity to the fabrication process.

Each structural color generation method offers unique advantages and industrial applications. Thin films are particularly advantageous in manufacturing due to their ability to be deposited without requiring photolithography. Furthermore, a variety of deposition methods are available for thin films, allowing the process to be tailored to specific applications. For example, many industries use physical vapor deposition (PVD) to achieve great thickness and uniformity.[25,54,55] However, PVD requires flat substrates and high vacuum conditions, which can be limiting.

Solution processing is an alternative method that does not require high-vacuum conditions and can coat conformally.[30,31] However, solution processing relies on liquid phase source materials, which can be challenging for some materials like semiconductors. Chemical vapor deposition (CVD), a vapor-phase technique that relies on chemical reactions of precursor gases, offers excellent conformality and thickness control. Despite its advantages, CVD has material limitations due to the gaseous nature of its precursors. Overall, thin films stand out as a

straightforward and versatile method for generating structural color, supported by a wide range of deposition techniques.

1.3.2 High-Low-Absorber (HLA) and Metal-Dielectric-Metal (MDM) Structures

Many structural colors have been fabricated with simple thin film structures, such as pearlescent coatings and nanoscale dielectric layers on metal substrates.[56–58] However, these single-layered coatings typically have low quality factor and poor color purity.[59] Alternatively, high color purity can be achieved with simple tri-layer cavities. Two discussed extensively in this work are the HLA and Metal-Dielectric-Metal (MDM), shown in Figure 7. These structures are also known as asymmetric Fabry-Pérot cavities, in which the top layer is optically thin while the bottom is optically thick.[60] The thin layer allows light to transmit into the dielectric cavity while also acting as one of the cavity reflectors. The thickness of the cavity layer tunes the resonance wavelength, changing the color. Material selection for the top and bottom layers is important to achieve high-chroma coatings, requiring equal absorptive and radiative losses in the cavity.[30] For this reason, reflective substrates must be balanced with absorptive top layers, such as in MDM structures. Lossy substrates may not require additional absorption for critical coupling, so the top layer can be a lossless reflector such as in HLA structures.

To understand the physical mechanisms driving these optical resonances, we should examine the propagating electric field. The simplest resonance condition is for quarter wavelength destructive interference, shown in Figure 7. In this case, incident light is confined to the optical cavity as a standing wave, destructively interfering wavelengths that accumulate a pi phase shift. The confined wavelengths must be absorbed by the structure. For MDM structures, the top metal acts as a great absorber because it lies at the electric field maximum, in accordance with the Beer-Lambert Law.[61] However, for HLA structures, the bottom substrate layer absorbs

light. This is because light can penetrate lossy media up to the skin depth, resulting in a non-zero electric field within the material. The relative absorption in each layer is shown in Figure 7 by the red regions.

Destructive interference requires a total accumulated phase shift of pi, which can be calculated using the Fresnel equations, including contributions from propagation and reflection.[62]

$$r = \frac{n_d - (n + ik)}{n_d + (n + ik)} = \frac{(n_d - n)(n_d + n) + k^2}{(n_d + n)^2 + k^2} - i\frac{2n}{(n_d + n)^2 + k^2}$$

$$\phi_{reflection} = tan^{-1}\left(\frac{Im(r)}{Re(r)}\right)$$

$$\phi_{propagation} = \frac{2\pi}{\lambda_0} nd$$

$$\phi_{total} = \phi_{reflection,base} + \sum_i \phi_{propagation,i}$$

Eqn. 1-4

In *Eqn. 1-4*, r is the reflection coefficient for normal incidence light, n and k are the real and imaginary components of the substrate's refractive index, n_d is the dielectric refractive index, ϕ is the phase shift, λ_0 is the wavelength, and d is the dielectric layer thickness.

In the HLA structure, the dielectric layers are lossless and have no imaginary component ($k = 0$). In contrast, the MDM structure includes a top thin metal layer with a non-zero k, resulting in an attenuation factor. The total accumulated phase shift is calculated by adding the propagation phase shifts in the top two layers and the reflection phase shift from the lossy base layer. These calculations can be performed across all visible wavelengths to determine the resonant wavelength(s).

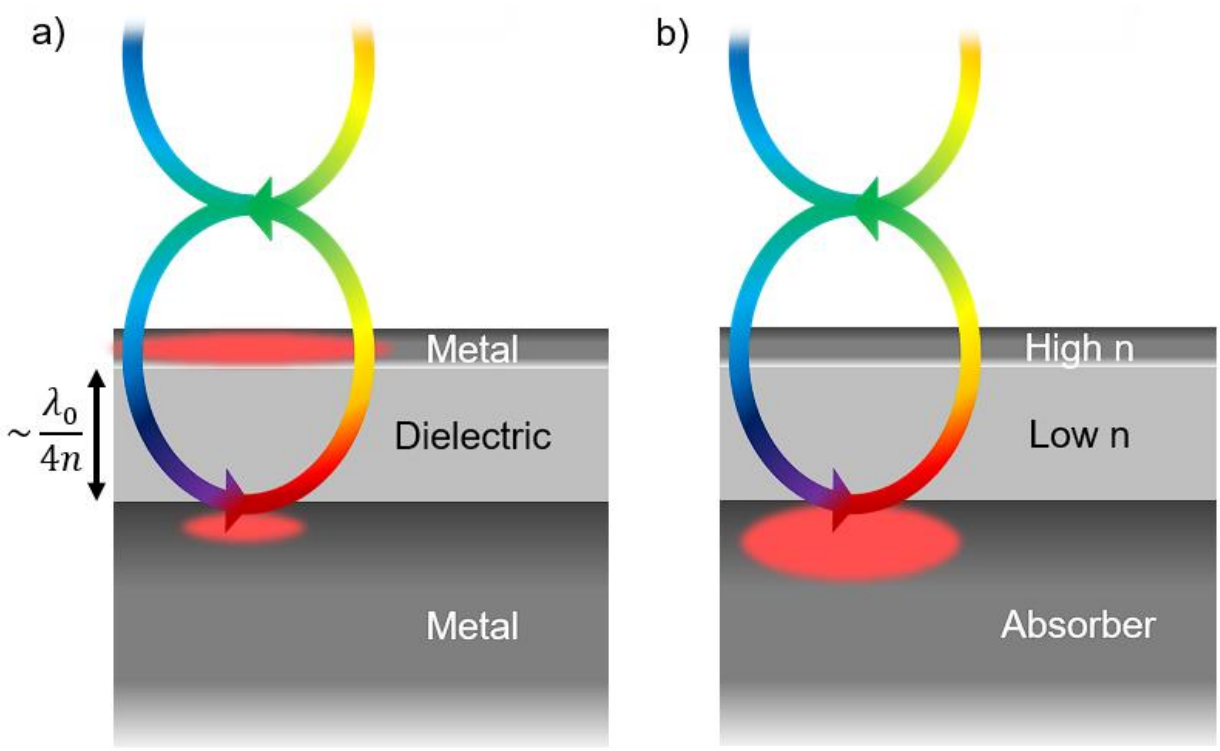


Figure 7. Light propagation and absorption in a) MDM and b) HLA structures.

While absorption in the top metal layer of MDM structures aligns with the Beer-Lambert Law, absorption in the base layer of the HLA structure requires further analysis. Two HLA structures were simulated using the Transfer Matrix Method with a TiO_2 / SiO_2 / Si structure, as shown in Figure 8. The SiO_2 cavity thicknesses were set to 30 and 220 nm, corresponding to first and second-order resonances, respectively. As illustrated in Figure 8(a,d), absorption peaks occur near a wavelength of 570 nm. From the layer absorption analysis in Figure 8(b,e), both HLA structures show that the base silicon layer is the primary contributor to optical absorption. Additionally, the electric field intensity profiles in Figure 8(c,f) reveal maxima in the TiO_2 layer and a node in the silicon absorbing layer. For the first-order resonance, a single electric field maximum is present, whereas two maxima are observed in the second-order resonance. These represent ¼ and ¾ wavelength resonance.

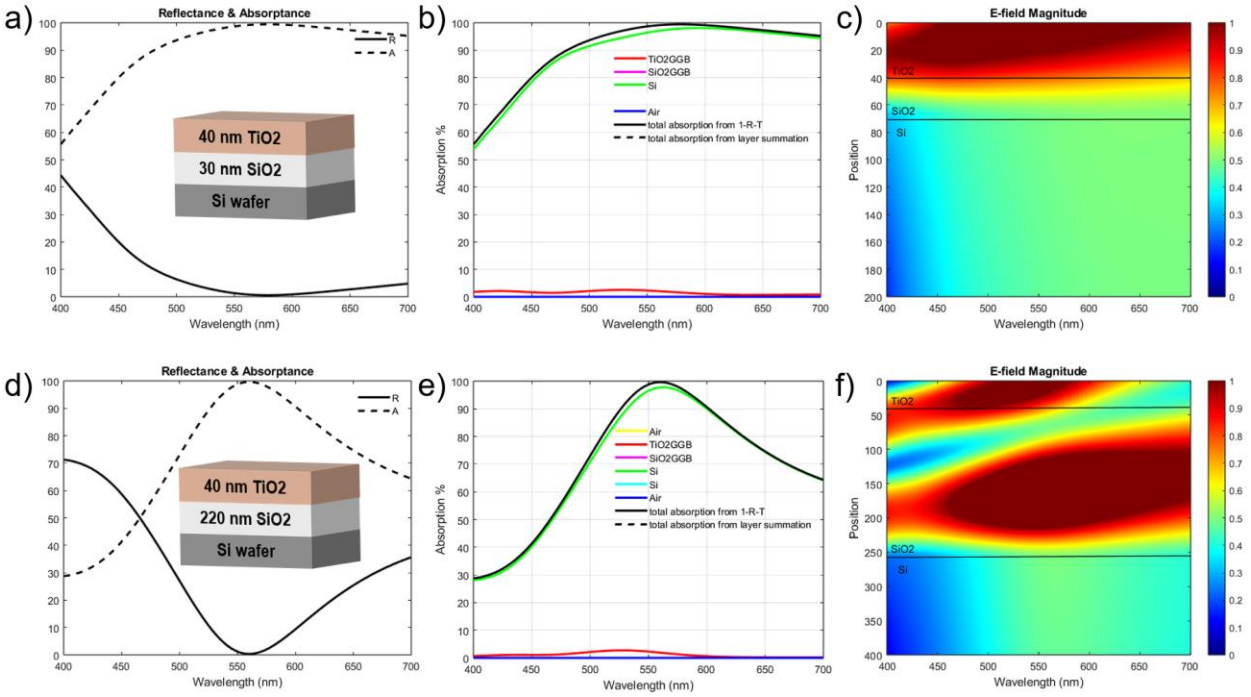


Figure 8. Absorption and electric field intensity in an HLA structure for a-c) first-order resonance and d-f) second-order resonance.

Phase analysis of the optical cavity clarifies the absorption mechanism in the base silicon layer. A schematic of the optical paths and accumulated phases is provided in Figure 9. Using *Eqn. 1-4*, the reflection and propagation phase shifts were calculated for these two paths at a wavelength of 579 nm. Since crystalline silicon permits visible light to penetrate its surface, there are phase shifts resulting from propagation and reflection within the silicon layer. Positioning the electric field node 25 nm into the silicon yields a total phase shift of pi for light exiting the cavity. This supports the findings in Figure 8, demonstrating that light must propagate approximately 50 nm through the silicon with a non-zero electric field, resulting in significant absorption within this layer.

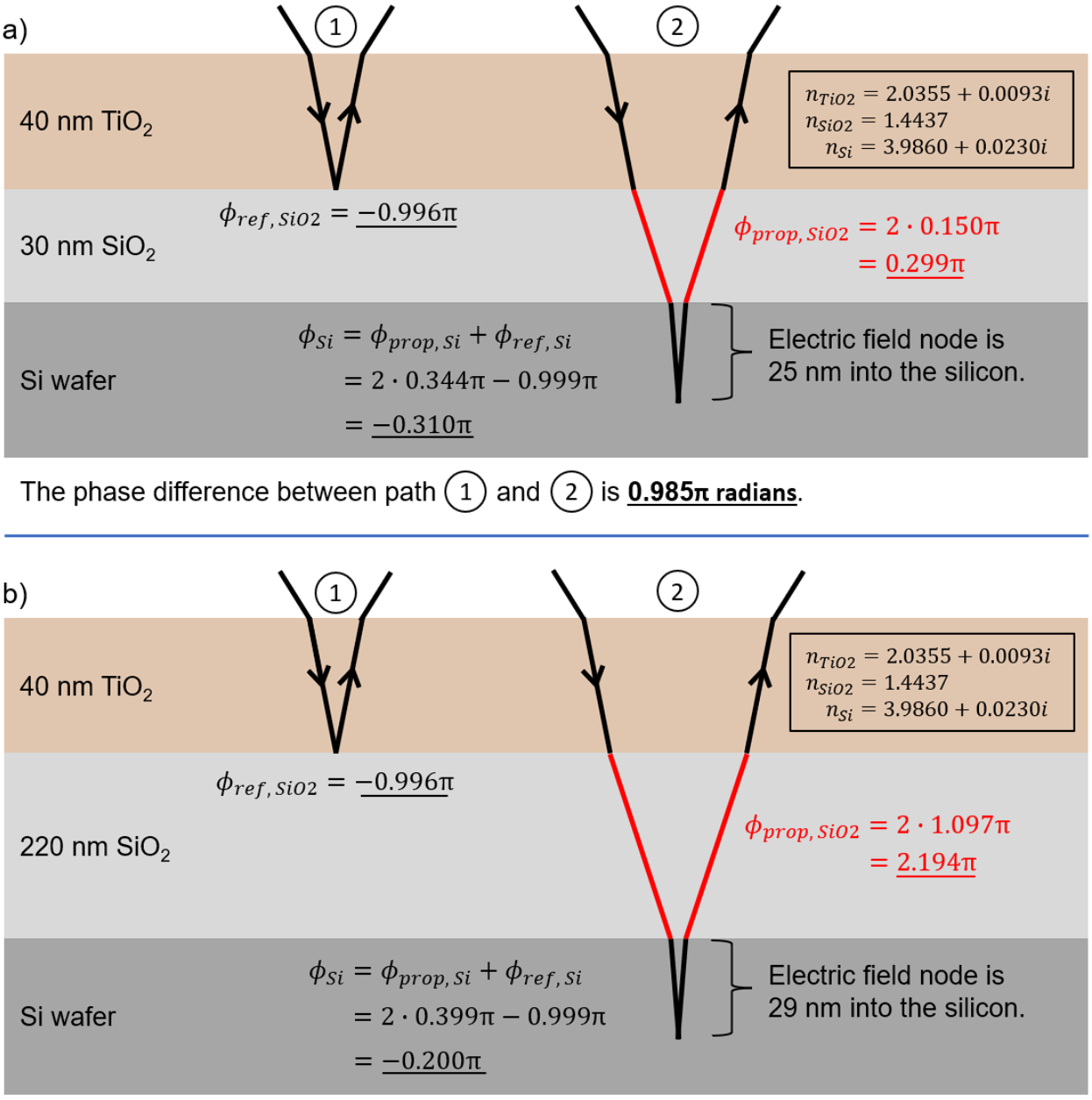


Figure 9. Phase analysis of a) first-order and b) second-order resonance light in an HLA cavity.

The MDM and HLA structures serve as important designs for investigating high-chroma coatings in this work. The HLA structure, with its ability to utilize abundant dielectric materials, is well-suited for exploring cost-effective and environmentally sustainable alternatives to traditional high-cost coatings. Its high vibrancy demonstrates the potential of mineral-derived thin films to achieve color comparable to those produced by the MDM structure. Meanwhile, the MDM structure, with its sharp reflection contrast and tunability, provides an ideal structure to test advanced structural color applications, such as patterning and conformal coatings. Together, these two structures offer complementary approaches to creating vibrant, functional coatings, supporting both fundamental research and practical applications.

1.4 Thesis Outline

1.4.1 Innovations in Additive Manufacturing for Functional Coatings

Chapter 2 highlights the use of abundant minerals as source materials for structural color coatings, reducing production costs and environmental impact compared to traditional high purity source materials. High-quality optical coatings were successfully deposited using impure starting materials, enabled by the inherent distillation behavior of electron-beam evaporation. This chapter also provides insights into the evaporation mechanism and the optical properties of the resulting thin films through X-ray Photoelectron Spectroscopy (XPS) analysis. Best practices for electron-beam evaporation are discussed in detail.

Chapter 3 explores advanced applications of structural color coatings, focusing on enhancing their functionality and versatility. Black structural color coatings were designed using a modified MDM structure to minimize visible light reflection. Thick TiO_2 coatings demonstrate reversible thermochromic behavior, showing their potential as temperature sensors. Additionally,

structural color flakes were fused to glass by baking with ceramic glaze, presenting a robust technique for integrating and protecting color filters in glass panels.

In Chapter 4, structural color coatings are patterned using area-selective atomic layer deposition (AS-ALD). Through patterning techniques such as photolithography and electrodynamic jet printing, polymer inhibitors were applied to selectively deposit ALD layers. This approach enables the creation of intricate structural color patterns and conformal color coatings on irregularly shaped objects.

1.4.2 Advanced Additive Techniques for Printed Electronics

This work also explores the use of additive manufacturing to print functional electronic devices and patterns. Chapter 5 focuses on printing carbon nanotubes (CNTs) as the channels of thin film transistors using a novel nozzle-free printing approach called Shock-wave Jet Printing (SJP). This technique uses laser-generated focused ultrasound (LGFU) to cause micro cavitation at the ink interface. For liquid inks, the micro cavitation produces micro jets of ink that were used to print high resolution patterns. The performance of these printed devices was compared to inkjet printing and yielded similar performance while avoiding the drawbacks of nozzle clogging and ink formulation.

Shock-wave Jet Printing can be applied to solid functional materials as well, discussed in Chapter 6. Many functional materials have limitations that prevent their use for devices and electronics, such as vacuum and temperature degradation. Alternatively, SJP is capable of printing patterns of solid material by ejecting particles from a transfer film. SJP acts as a typewriter in this scenario, punching clusters of particles in localized areas that are caught by the receiving substrate. This method has great potential to expand the use of functional materials for device printing.

Chapter 2 Harnessing Natural Minerals for Structural Colors

2.1 Introduction to Structural Colors from Natural Minerals

2.1.1 Motivation for Using Abundant Minerals in Structural Colors

Structural color coatings have gained significant attention in recent years due to their incredible vibrancy, durability, and environmental resistance, offering clear advantages over traditional organic pigment coatings.[4,15–29] These coatings produce color through physical structural resonances with light, resulting in robust color coatings that withstand UV radiation, humidity, temperature variations, and chemical exposure.[4,25,63] Advancements in machine learning (ML) have revolutionized the design process[55], enabling the design of optical coatings for nearly any application by referencing a large variety of material refractive indices.[64–66] ML-assisted design has the potential to transform industry and academic coatings by utilizing natural materials without refinement, encouraging long-term sustainability for large-scale industrial manufacturing of structural colors and lower material cost.

There are many layered structures that have been utilized for structural color applications.[25,55] The High-Low-Absorber (HLA) structure, composed of three dielectric layers with distinct refractive indices, is particularly well-suited for this goal, enabling the study of diverse thin films and their optical behaviors.[30] Traditionally, optical coatings have relied on high purity source materials deposited via sputtering or evaporation. While effective, these methods are primarily intended for electronic devices and require expensive, high purity metal starting materials, limiting the scalability of these coatings in high-volume manufacturing. Instead,

significant costs and waste can be avoided through the use of raw minerals found in nature as starting materials for structural color coatings. Natural minerals are abundant chemical compounds with diverse material properties. Technically, as long as the refractive index dispersions of these materials are obtained (e.g. by ellipsometry measurement), they can be readily included in our material database for deep learning-based structural color design. A custom-made laboratory electron beam (e-beam) evaporator was built to deposit such raw materials, separate from cleanroom tools to avoid contamination. E-beam evaporation is particularly advantageous for raw materials, as it can melt and refine solid targets containing mixtures and impurities, making it one of the few techniques suitable for such applications.

This chapter is adapted from Rorem et al., "Harnessing Natural and Abundant Minerals: A Step Toward Low-Cost Multilayer Structural Color Coatings" submitted to *Advanced Functional Materials* for review on Nov. 28, 2024. This work was done in collaboration with Yian Cheng and L. Jay Guo.

2.2 Fundamentals of High-Low-Absorber (HLA) Structures for Structural Color

2.2.1 Overview of the HLA Structure

Simple yet vibrant coatings can be achieved with three stacked thin films. The HLA design is one stack capable of producing vibrant coatings, with or without metallic layers, enabling the use of abundant dielectric materials.[30] For example, a silicon substrate can serve as the absorber in an HLA design, with an SiO_2 optical cavity layer and a 40 nm TiO_2 top layer acting as the high refractive index reflector. This thin TiO_2 film reflects light, but it must remain below a critical thickness to avoid acting as an optical cavity itself due to quarter-wavelength resonance beyond 40 nm.

The HLA structure was utilized in section 1.2.4 to demonstrate high-chroma coatings. As discussed in section 1.3.2, the absorbing silicon layer attenuates light while the TiO_2 reflector radiates it, resulting in evenly matched radiative and absorptive losses. This balance, known as the critical coupling condition ($\gamma_{rad} = \gamma_{abs}$), allows for zero reflection at the resonant wavelength.[30] The flexibility in material choice for the HLA structure enables a wide range of combinations, making it a versatile and cost-effective choice for producing vibrant coatings.

2.2.2 Comparison to MDM

Another example of a vibrant thin-film structure is the MDM design.[31,67] This structure comprises two metallic films sandwiching a dielectric layer, with resonant wavelengths controlled by the thickness of the middle dielectric. The bottom metal acts as a thick optical reflector, while the middle dielectric, typically a transparent material, determines the resonance. The top metallic film acts as a thin optical absorber, permitting light to enter the cavity. This design, also known as an asymmetric Fabry-Pérot cavity, is capable of producing high-chroma coatings due to the sharp contrast between the peaks and valleys of its reflection spectra. Adding an additional dielectric layer as an anti-reflection coating further enhances the purity of primary colors produced by the MDM structure.[68]

While highly effective, metallic films are significantly more expensive than dielectric films due to the costs associated with refining metals. For example, in this study, TiO_2 films were deposited using a ceramic powder sourced from rutile deposits. To refine titanium metal, this TiO_2 powder must undergo at least two reduction steps and one distillation step, significantly increasing production costs.[69] The high cost of metallic films encourages exploration into vibrant color coatings using abundant mineral thin films, which offer a more cost-effective solution without sacrificing chroma. The HLA structure, utilizing three distinct dielectric layers, offers a cost-

effective alternative while maintaining the ability to achieve the critical coupling condition, making it an excellent choice for producing high-chroma colors.

2.3 Selection and Processing of Raw Minerals for Structural Colors

2.3.1 Choosing Suitable Minerals for Each Layer in HLA

With the principles of the HLA structure established, we now focus on selecting and preparing suitable materials to achieve these designs with cost-effective, minimally processed minerals. For the HLA structure, high and low refractive index layers are required. These layers should be both lossless and abundant, making TiO_2 and SiO_2 ideal choices due to their refractive indices of approximately 2 and 1.4, respectively. Instead of using traditional 99.9% pure e-beam evaporation pellets, ceramic powders were selected as the source materials. Ceramic powders are raw minerals with minimal processing to achieve standard purities above 90%.[69] The TiO_2 and SiO_2 powders in this study were sourced from rutile and sand deposits, respectively.

The use of ceramic powders as minimally processed raw materials offers several compelling advantages. Economically, ceramic powders are significantly more cost-effective than highly refined materials, making them attractive for large-scale manufacturing. The abundance of natural minerals further supports this approach, providing a sustainable resource for thin-film deposition. From an environmental perspective, minimally processed materials reduce the ecological impact of the manufacturing process, decreasing both energy consumption and waste generation. The versatility of ceramic powders is another key benefit, as a wide range of oxides and minerals can be sourced. This flexibility allows for tailored material properties and broadens the scope of potential applications.

In addition to TiO_2 and SiO_2 layers, we focused on finding an absorbing layer to ensure the HLA design could work on any substrate. Two colorful minerals, scoria and blue topaz, were tested, but their evaporated thin films exhibited refractive indices nearly identical to SiO_2. This result indicated that the bulk absorbing properties of minerals do not always translate to their evaporated thin films. An effective absorbing film requires a bandgap below 3 eV, so we sought to evaporate minerals that fit this criterion. Two examples are CuO and Fe_2O_3, which have bandgaps of approximately 2 eV each.[70,71]

Ceramic powders for CuO and Fe_2O_3 were sourced from tenorite and hematite, respectively. While both minerals exhibit a black or gray appearance in bulk form, their true optical properties are revealed through their streak. Streak is produced by scraping the mineral on a ceramic tile, leaving a line of mineral powder that represents the true color, free from bulk crystalline resonances. CuO powder, for instance, is a dark black, while Fe_2O_3 powder is a dark red, indicating that these oxides possess optical absorbing properties that could be suitable for thin films.

2.3.2 Preparation and Processing of Minerals

Ceramic powders are sourced from natural minerals and undergo minimal processing to achieve repeatable compositions.[69] SiO_2 powder (>99% purity, sand), rutile TiO_2 powder (~95% purity, rutile), CuO powder (>99% purity, tenorite), and Fe_2O_3 powder (95% purity, hematite) were obtained from US Pigment Corporation.[72–75] The raw minerals are mined from natural deposits and crushed into finer particles for a more uniform size distribution. These particles then undergo beneficiation, a purification process to remove some impurities using methods like froth flotation, magnetic separation, or chemical leaching. Removed impurities include iron oxides, organic matter, and other trace minerals. The particles are then heat-treated around 1000C to

remove moisture and volatile impurities, as well as to enhance the oxide phases. Finally, the particles are milled to the desired grain size and packaged, with typical purities ranging from 90 to 99%.

In contrast, high purity materials for cleanroom deposition require significantly more investment to achieve 99.9% purity, especially metals which require reduction. Titanium, for instance, begins with the aforementioned purification to rutile TiO_2 powder.[76] TiO_2 is oxidized with chlorine gas in a fluidized bed reactor at 1000 °C to produce $TiCl_4$, which is then distilled. $TiCl_4$ is then heated with magnesium or sodium at 1200 °C for multiple days to reduce to a titanium metal sponge, which is then crushed, cleaned, and melted into ingots. This example illustrates how ceramic powders require significantly less processing and energy than high-purity materials. While these powders still require some purification, these steps ensure repeatable results in the laboratory while keeping processing costs to a minimum.

2.4 Deposition and Characterization of Mineral-Based Structural Color Films

2.4.1 E-Beam Evaporation Mechanism

Electron beam evaporation is a type of physical vapor deposition (PVD) where a kW-range electron beam gradually heats source material until it melts and eventually evaporates at a noticeable rate, known as the deposition rate. The vaporized molecules travel across a vacuum chamber and land on the target substrate. The crucible liner holds the source material and is water-cooled to prevent cracking. Consequently, the high temperature at the surface due to e-beam heating causes thermal gradients throughout the material and convection occurs in low-viscosity melts. Large temperature variations can induce pockets of rapid boiling, leading to a spitting effect. Therefore, gentle heating and sweeping the e-beam location are recommended practices for powders and materials with low thermal conductivity.

While the material undergoes significant temperatures changes, phase transitions, and movement due to convection currents, several reactions can occur. First, the e-beam can dissociate oxygen atoms from oxide molecules, as the electronegative beam repels anions like oxygens in insulators. This effect is more pronounced in certain materials like TiO_2 and less in others like SiO_2. Second, the source material can react with the walls of the crucible liner. Sometimes, the liner can reduce the source material by stealing oxygens or other anions. The material with the lower standard Gibbs free energy of formation can reduce the other, capturing its oxygens. Third, if a mixture is present, the components can exchange and react similarly. Such behavior obeys the Ellingham Diagram for oxides, shown in Figure 10.[77] Fourth, metal oxide materials can spontaneously reduce in high-temperature conditions when $T\Delta S > \Delta H$, where T is the temperature, S is the entropy, and H is the enthalpy.[78] With these potential reactions, various molecular species may coexist during e-beam evaporation.

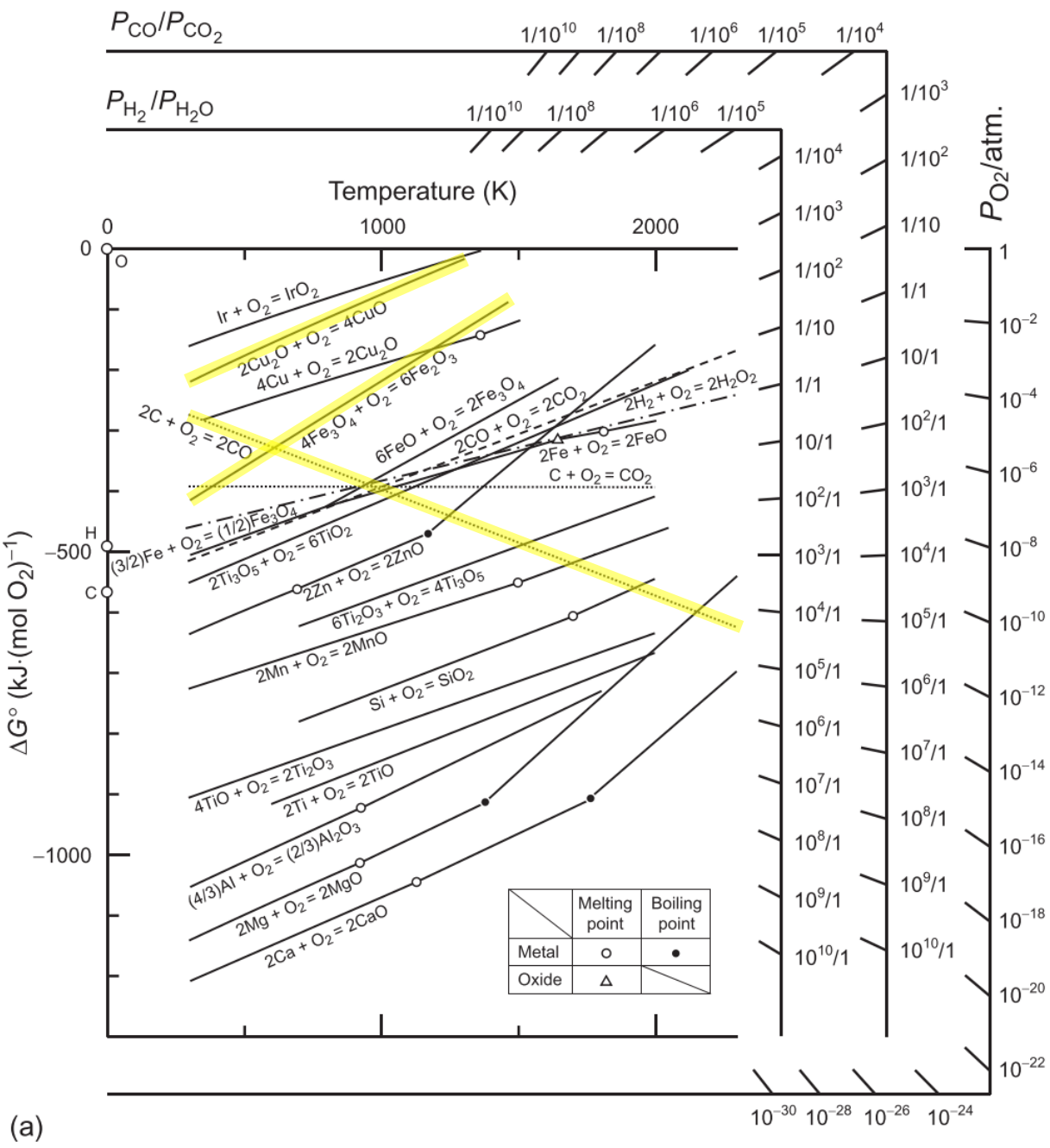


Figure 10. The Ellingham diagram for metal oxides. Relevant reactions are highlighted. Image adopted from Ref. 75.

2.4.2 Changes in Material Composition During E-Beam Evaporation

Some materials that dissociate into multiple molecular species during evaporation include CuO and Fe_2O_3.[32] After deposition, CuO thin films changed color when exposed to air, suggesting an oxidation effect. Since CuO is the most oxidized form of copper oxide, this observation indicates that multiple copper oxide species were present and that some CuO molecules were reduced during e-beam evaporation. Additionally, Fe_2O_3 powder changed composition during evaporation. The source powder became magnetic after melting and cooling, which suggests a significant presence of magnetite (Fe_3O_4). Similar to CuO, Fe_2O_3 was reduced by the e-beam. Moreover, combining CuO and Fe_2O_3 powders in a 1:1 molar ratio resulted in a redox reaction, reducing some of the CuO powder to copper metal. These results demonstrate the complex chemical interactions during e-beam evaporation and the potential for generating different materials.

The instability of sulfide-based minerals under e-beam evaporation conditions further justifies our focus on oxides.[79,80] For example, pyrite (FeS_2) was ground into a powder and subjected to e-beam heating in a vacuum. Even at half the power required to evaporate SiO_2, the pyrite dust became volatile. Particles scattered throughout the chamber, and a deposition rate of 1 A/sec was recorded. The deposited film was diffuse, with micro-scale particles visible under a microscope. Over the course of a week, the film largely disappeared, condensing into larger, sparse particles. These results highlight the inherent instability of sulfide minerals during vacuum deposition, making oxides a more suitable choice for achieving stable, high quality thin films.

Though the presence of multiple atomic species complicates the deposited film's composition and repeatability, e-beam evaporation also inherently refines materials through distillation. In the crucible liner, the molten source material is heated to a temperature yielding the

desired deposition rate. At this temperature, different molecular species exhibit varying vapor pressures, with the one possessing the highest vapor pressure dominating the deposition rate. This process, known as fractional distillation, is widely used in industries to separate liquid components from mixtures. The relative vapor pressures at high vacuum can often be predicted by comparing melting temperatures at standard conditions. Solutions and alloys can skew these results, but the fundamental principle remains valid. While these challenges highlight the complexity of working with raw minerals, they also underscore the unique ability of e-beam evaporation to refine and process materials, making it a valuable tool for scalable, cost-effective structural color production.

2.4.3 E-Beam Evaporation of Mineral-Based Films

A custom electron beam evaporation system was built for this work, with additional details provided in Appendix A. To ensure consistent and high-quality deposition results, several key practices should be followed. Maintaining a standard chamber pressure during deposition is important, as the presence of air molecules can impact the evaporation process and affect the deposited film density, thus altering the refractive index. Typical chamber pressures for evaporation in cleanroom settings are around $5 \cdot 10^{-4}$ Pa. Such a high vacuum is necessary for repeatable device-quality coatings, but a lower vacuum is acceptable for optical-quality coatings. For instance, in this work, all films were deposited at around $5 \cdot 10^{-2}$ Pa. A lower vacuum is advantageous as it reduces the need for expensive, high-quality turbo pumps. As long as the vacuum is sufficiently low for the tungsten filament to create a stable e-beam, it is acceptable for optical coatings.

When heating materials with low thermal conductivity, including all powders, gentle heating and e-beam sweeping can help prevent rapid boiling and minimize spitting. Proper preparation of the powders and crucible liners is essential to prevent contamination and ensure

uniform deposition. Many reactions can occur during the process, so careful material selection is required. In this work, graphite crucibles were used for consistency across all tests and due to their lower cost. However, a different crucible liner material may improve film quality for certain materials, such as the stability of the CuO film. Regardless of crucible liner material, the source material should be regularly refreshed to maintain a consistent height and composition in the liner. During evaporation, the e-beam sweep can result in deposition rate oscillations; thus, the sweep size and speed should be adjusted to minimize this, with values differing for each material based on their thermal conductivity.

For this study, the e-beam power was slowly ramped to a mid-power soak level to uniformly heat the material to a temperature near its melting point. Then, the power was slowly increased further to achieve the desired deposition rate. Substrates were positioned 30 cm above the crucible and rotated at 20 rpm to ensure uniform deposition. Once the desired deposition rate was reached, the shutter was opened, allowing evaporated molecules to deposit onto the substrates. The deposition parameters for various materials were as follows:

- **SiO_2, scoria, and blue topaz:** Deposited at 5 A/sec with 9.5% power.
- **TiO_2:** Deposited at 3 A/sec with 15% power.
- **CuO:** Deposited at 0.3 A/sec with 7.5% power.
- **Fe_2O_3 and hematite gems:** Deposited at 0.5 A/sec with 10% power.
- **CuO and Fe_2O_3 mixture:** Powders were mixed in a 1:1 molar ratio before deposition to promote a redox reaction during heating. The mixture was deposited at 3 A/sec with 9% power.

These results demonstrate the importance of adapting evaporation parameters for each material to achieve high-quality thin films while maintaining cost efficiency and environmental sustainability.

2.4.4 Characterization Techniques for Structural Color Films

Refractive indices and thicknesses of deposited films were measured using a Woollam M-2000 Ellipsometer in the Lurie Nanofabrication Facility, with measurements taken between 300 and 1400 nm at 65, 70, and 75 degrees. All measured films were deposited on 300 nm SiO_2 on Si wafer pieces. The thick SiO_2 layer creates an index contrast with the target film, enhancing the interference effects and thus the polarization changes. All films except SiO_2 were modeled with a B-spline model. E2 was forced positive if the imaginary part of the index was negative. The Kramers-Kronig relation was used if it improved the goodness of fit. SiO_2 was modeled with a Cauchy model.

XPS measurements were performed using a Kratos Axis Ultra DLD system with monochromatic Al kα source (10 mA, 12 kV) with a pass energy of 20 eV and a step size of 0.1 eV on a spot size of 700 μm by 300 μm. Spectra were recorded for the Cu 2p and Fe 2p regions, as well as the Cu LMM Auger peak. The obtained spectra were analyzed using CasaXPS software.

Reflectance spectra at normal incidence were obtained using an Ocean Optics Inc. HR4000CG-UV-NIR High-Resolution Spectrometer integrated with a white light source. Optical microscope images were obtained with a Keyence VHX-7000 microscope at 50x magnification with full coaxial lighting. The simulated reflectance spectra were calculated using the Transfer Matrix Method approach in MATLAB. Optical constant data for the layers were measured with ellipsometry.

2.5 Results: Optical Properties and Color Quality of Mineral-Based Films

2.5.1 Cost-effective Coatings with SiO_2 and TiO_2 Films

The first demonstration of cost-effective structural color films is presented in Figure 11. By utilizing an SiO_2 cavity layer on silicon substrate, topped with a 40nm TiO_2 film, a wide array

of colors was possible. By varying the SiO_2 film thickness from 170 to 350nm, we produced colors ranging from yellow to purple to green. Each color includes an optical microscope image of a 2x4mm area of the coating. Reflectance spectra, both measured and simulated, are also included. Simulations were performed with the transfer matrix method (TMM) and refractive index data for each film, gathered with ellipsometry. The CIEL*a*b* coordinates for these coatings, shown on the right, represent the lightness, chroma, and hue. The coatings show a spiral pattern in the a*b* coordinates, indicating that chroma decreases as SiO_2 thickness increases. This demonstration underscores the potential for vibrant color coatings with inexpensive starting materials. While the silicon substrate provided a good foundation for ellipsometry and spectrometer measurements, an alternative absorber layer will be needed for these coatings to be applicable on any flat surface.

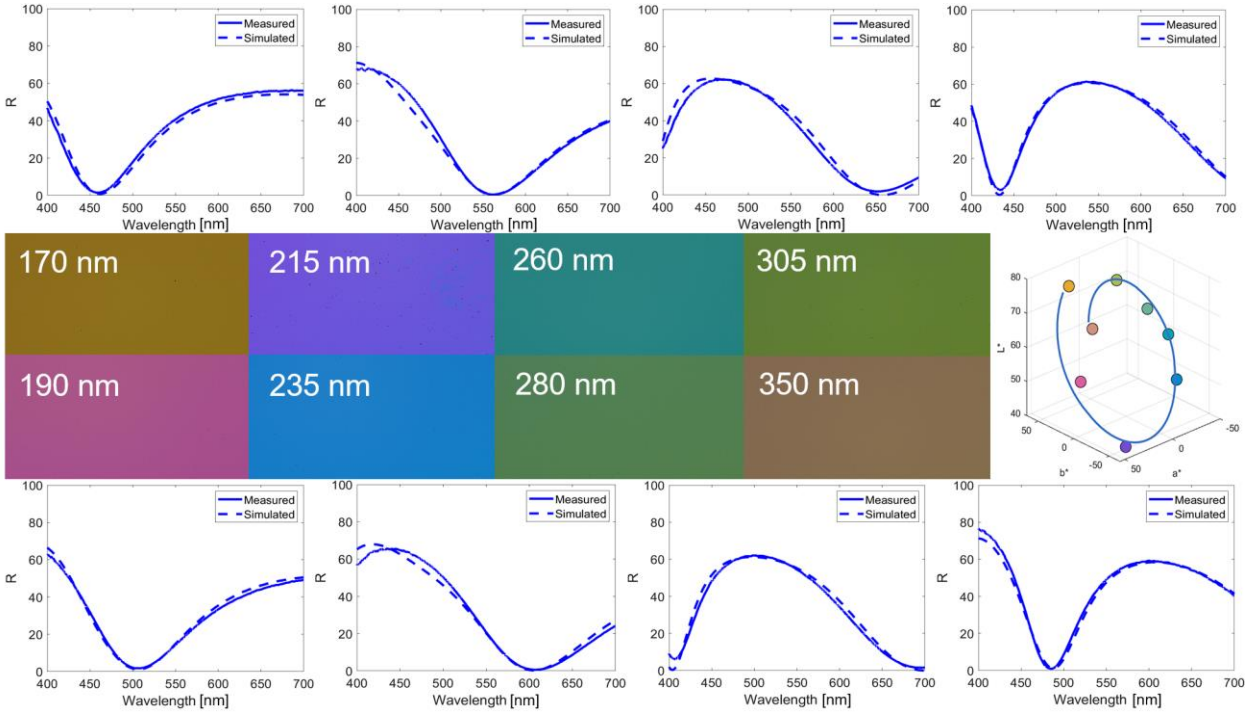


Figure 11. High-chroma, planar HLA coatings with varying cavity thicknesses. Optical microscope images, reflectance spectra, and calculated CIELAB coordinates are included.

2.5.2 SiO_2 Distillation with E-beam Evaporation

Although a silicon wafer is an effective absorbing substrate, it is also expensive and uncommon. To expand the applicability of the HLA structure, we need to identify a suitable absorbing film as the base so the structure can be deposited on glass, plastic, or any other common planar surface. In our search for absorbers to replace silicon, we explored various materials, but some had refractive indices that appeared similar to SiO_2. Figure 12a presents the refractive indices for some SiO_2-containing minerals we deposited, each film >30nm. This figure does not show the imaginary part of the refractive index because SiO_2 films are optically transparent, with all films having k=0. The refractive index of the ceramic powder SiO_2 (solid black) was compared to pure crystalline SiO_2 deposited in a cleanroom evaporator (dashed black).[81]

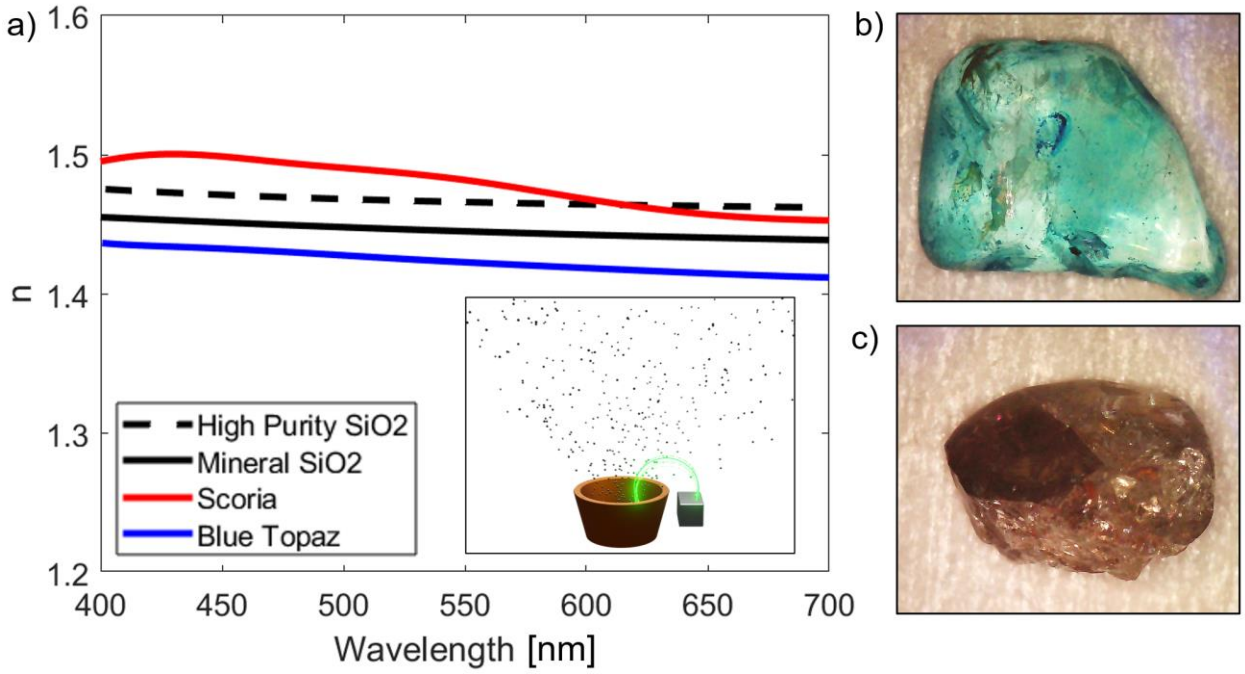


Figure 12. a) Refractive indices of SiO_2-containing minerals. b) and c) show blue topaz before and after deposition, respectively.

Additionally, two other materials, scoria and blue topaz, are included in Figure 12a. Despite their distinct bulk forms, brown-red for scoria and blue for topaz, their optical responses are nearly identical to SiO_2 when deposited as thin films via evaporation. Scoria, a lava rock composed primarily of the Earth's crust, is predominantly SiO_2. It exhibits a red/brown appearance due to the presence of metal oxides like Fe_2O_3, but these metal oxides do not significantly affect the refractive index of the deposited thin film. The physical explanation for this is that SiO_2 tends to sublimate near 1300-1400 °C[82], resulting in a higher vapor pressure compared to metal oxides like Fe_2O_3 which melt above this temperature. This is evident as SiO_2 requires significantly lower e-beam power, and thus a lower temperature, to achieve the same deposition rate as Fe_2O_3. Consequently, SiO_2 can be deposited from scoria without incorporating many impurities.

Blue topaz, an artificially colored gemstone with a transparent blue color like in Figure 12b, provides another example. Plain topaz is a white/gray aluminum silicate that is irradiated with a low-energy electron beam to create oxygen vacancies, resulting in the blue color due to crystal resonances. However, during e-beam evaporation, the crystal lattice deforms, and defects are removed as the topaz melts. As shown in Figure 12c, the blue topaz loses its blue color after deposition. The topaz crystals turned from blue to brown to white as they melted during e-beam evaporation. Not only does the gem lose its blue appearance, but any aluminum oxide species were also removed from the thin film during SiO_2 distillation. These results indicate that the primary factors determining the optical response of the deposited thin film are the mineral composition and vapor pressure, rather than the bulk appearance of the source material.

2.5.3 Optical Performance of TiO_2 Films

Next, we studied the optical behavior of TiO_2 ceramic powder, presented in Figure 13. TiO_2 is notorious in evaporator systems for having an inconsistent refractive index, mainly due to dissociation of oxygen atoms during heating. Reports on evaporated TiO_2 films also indicate variability due to the vacuum level of the chamber.[83–85] To verify these findings, multiple TiO_2 films were deposited at 3A/sec under various conditions, as depicted in Figure 13. In Figure 13a, the red curve represents TiO_2 deposited in a cleanroom e-beam evaporator using 99% pure TiO_2 pellets. The green and blue curves correspond to TiO_2 films deposited in our private evaporator; the green curve uses 99% pure TiO_2 pellets, while the blue curve represents ceramic powder under the same vacuum. The inset shows minimal absorption across the visible spectrum for all three samples. These indices show that the ceramic powder, despite a lower purity and higher vacuum pressure, can yield a similar refractive index to high purity, high vacuum deposition.

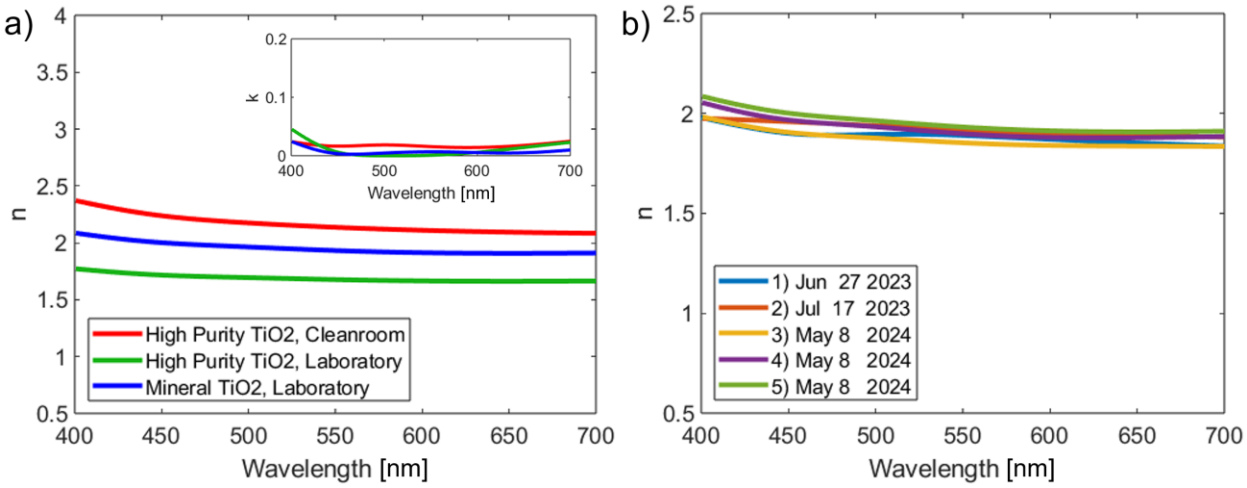


Figure 13. Refractive index data for TiO_2 films.

To assess optical stability, Figure 13b presents data from five samples measured at different points in time. The refractive index delta is about 0.1, primarily influenced by the vacuum level of the chamber and the age of the crucible melt. For example, sample 1 was deposited under higher pressure (~10^{-1} Pa) than the other five samples (~$5 \cdot 10^{-2}$ Pa). Samples 3 and 5 were deposited under the same vacuum conditions, but sample 3 used fresh powder, whereas sample 5 used an aged crucible. These results can be attributed to the vapor pressure of TiO_2 and other reduced titanium oxide species formed due to oxygen dissociation. Ti_3O_5 has a slightly lower melting point than TiO_2, making it slightly favored in the distillation process. Furthermore, Ti_3O_5 has a higher refractive index than TiO_2, which explains why sample 5 exhibits a higher index than sample 3. An aged crucible is likely to have experienced more oxygen dissociation. With this understanding, repeatable TiO_2 films were achieved maintaining a consistent vacuum pressure and refreshing the crucible source powder between runs.

2.5.4 Performance of Absorbing Layers from CuO and Fe_2O_3

Two other mineral materials were tested as absorbing layers and yielded surprising results: CuO and Fe_2O_3. Both were deposited from ceramic powders extracted from tenorite and hematite, respectively. The CuO powder was gently heated but could only achieve 0.3 A/sec before material began spitting. The refractive index of the CuO film is presented in Figure 14 for ~30nm thick films. As seen in Figure 14b, CuO exhibits strong absorption for a dielectric film, indicated by a k value greater than 1. After deposition, the films changed color over time in ambient conditions, and as they aged, the absorption waned to the level shown in Figure 14b. This color change appeared to be an oxidation effect, suggesting that the deposited film contained Cu_2O, which re-oxidized to CuO. The evaporation process likely dissociated oxygen atoms; to verify this, we measured the films using Xray Photoelectron Spectroscopy (XPS), discussed in section 2.5.5.

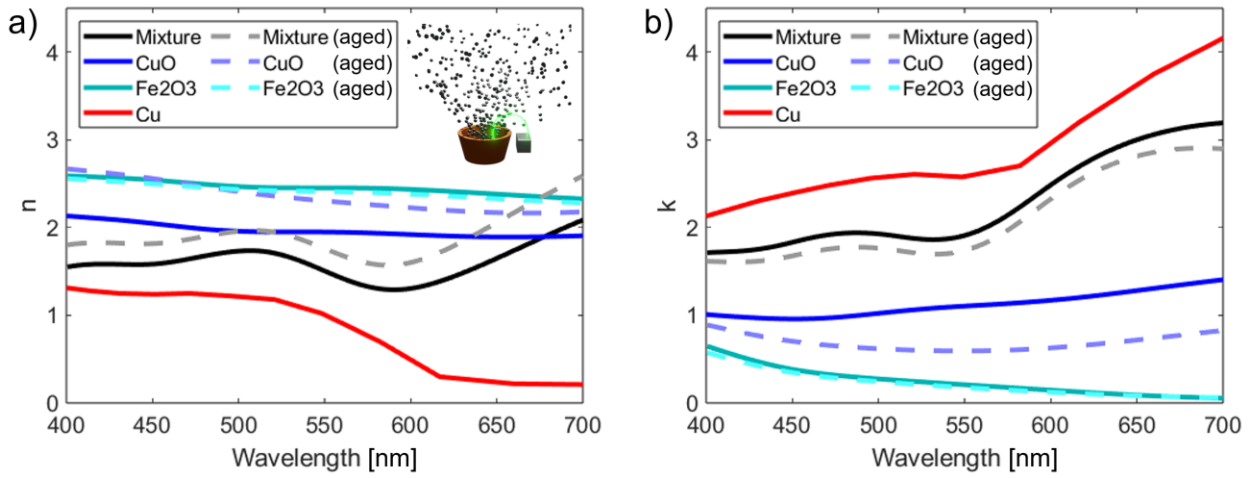


Figure 14. Refractive indices of evaporated absorbing films.

Next, we deposited Fe_2O_3 (hematite) from ceramic powder. While the Fe_2O_3 film remained stable in air, the solidified melt in the crucible became magnetic after cooling. Similar to CuO, Fe_2O_3 was gently heated until 0.5A/sec to avoid spitting. Figure 14 shows the optical response of the Fe_2O_3 thin film, which exhibits moderate absorption, though lower than CuO. The deposited Fe_2O_3 film did not change color over time, indicating its stability. As a test, a hematite gem was checked for magnetism and showed none. After grinding the gem into a powder, melting it during evaporation, and testing, it became magnetic. Additionally, the streak of the starting hematite was red, whereas the melt's streak was gray. These results indicate that the hematite reduced to magnetite, and the XPS analysis of section 2.5.5 will verify this. These results cast doubt on the stability and repeatability of both materials. However, combining minerals yielded promising advantages.

Lastly, we combined CuO and Fe_2O_3 powders in a 1:1 molar ratio. According to the Ellingham diagram,[77] mixing these two oxides should result in a chemical reaction that reduces the Cu atoms. During e-beam heating, these oxides may react, potentially reducing to metallic copper, Cu(0). As illustrated by the red curve in Figure 14b, metallic copper has high absorption,

making it an excellent candidate for the bottom absorbing layer in the HLA structure. The refractive index of the deposited film from the CuO-Fe_2O_3 mixture is shown in black in Figure 14. The curvature of the real and imaginary parts around the 550 nm region resembles the refractive index of metallic copper. The deviation is likely due to a presence of copper oxide species in the film in addition to the metallic copper

As the CuO-Fe_2O_3 mixture was heated, a molten liquid formed amidst some remaining solid powder. Visually, the viscosity of this liquid resembled molten copper, suggesting that the remaining solid powder is likely iron oxide. The mixture reached a stable deposition rate of 3A/sec at a lower temperature than needed to melt Fe_2O_3 alone, and the material did not spit even with a fast temperature ramp. If metallic copper is the dominant species in the crucible, its high thermal conductivity could be a significant factor for this stable high deposition rate. Additionally, metallic copper has a much lower melting temperature of 1083 °C in comparison to copper oxides, making it favored in distillation.[86] This mixture achieved a much higher stable deposition rate than either material individually, so mixtures may provide advantages for both the deposition process and the resulting film.

2.5.5 XPS Analysis of Metal Oxide Films

Films were prepared for XPS measurements to compare fresh and aged samples, as well as the hematite crucible and mixed absorber layer. Two films of both CuO and Fe_2O_3 were prepared five days apart and measured at the same time. Since XPS probes the top 10nm of a film, films were deposited with a thickness of 20-30nm. XPS results are shown in Figure 15.

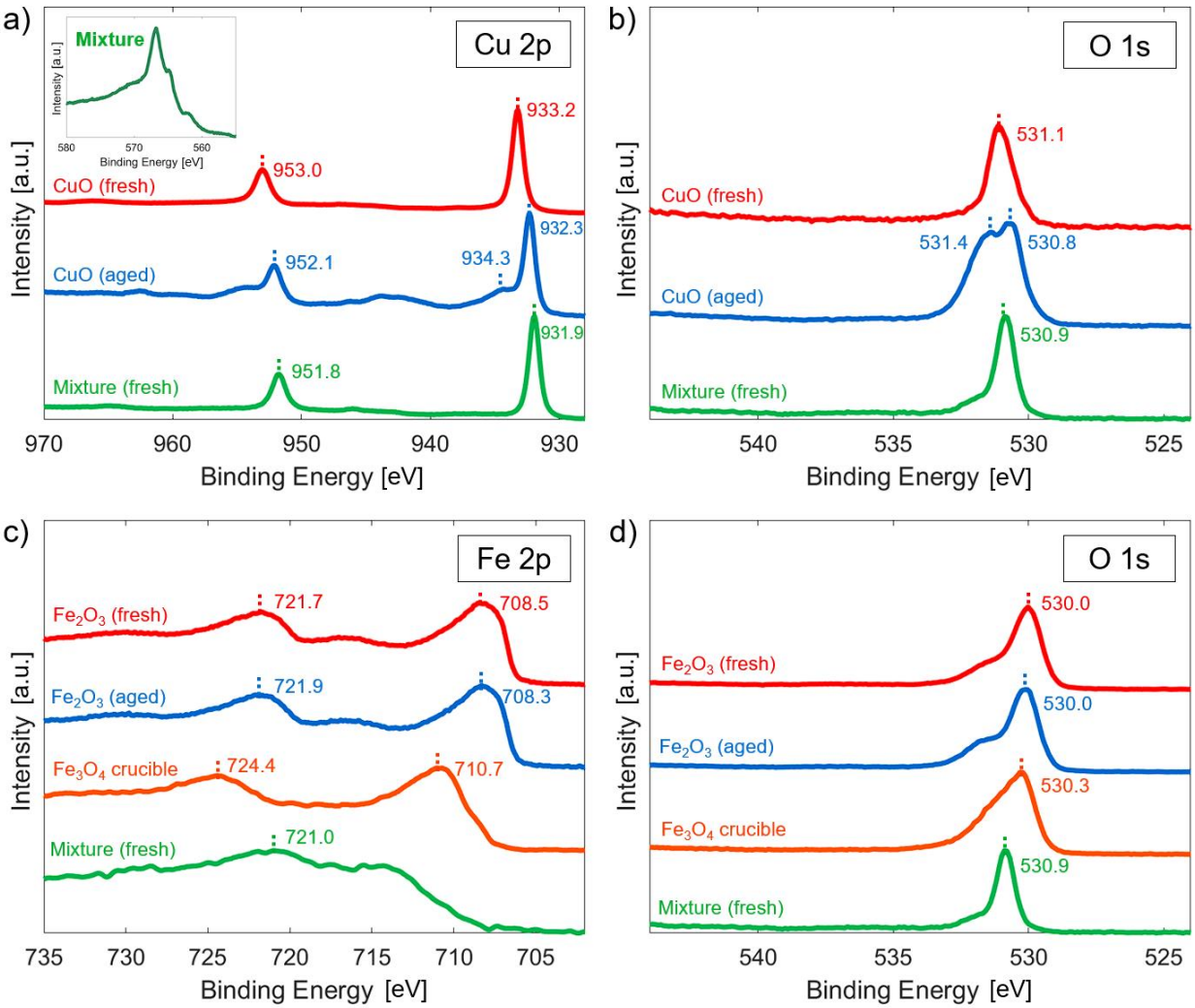


Figure 15. XPS spectra for the CuO, Fe_2O_3, Fe_3O_4, and mixture films.

From the CuO data shown in Figure 15a-b, the fresh film (red) deposited from CuO ceramic powder contained primarily Cu(I) and potentially Cu(0) atoms with no satellite peaks. The singlet oxygen peak indicated a uniform oxygen environment. The peak shapes and spacing matched reported Cu(I)/(0), but both the Cu 2p and O 1s peaks for this sample were approximately 1eV too high compared to reported values.[87] Since charge correction was accounted for by adjusting the carbon 1s peak to 285.0 eV, this peak shift indicated initial film stress. After aging for five days (blue), the film exhibited doublet 2p peaks with corresponding satellite peaks. Peak binding

energies were in agreement with reported Cu(I) and Cu(II) atoms, indicating a mixture of both oxidation states.[87] Analysis of peak areas revealed that the aged film consisted of 51% Cu(I) and 49% Cu(II) atoms. The O 1s peak for this sample showed a doublet, consistent with lattice oxygen and adsorbed hydroxyl bonds. In contrast to the fresh sample, the aged sample peak energies agreed with reported values, suggesting the film stress relaxed as it oxidized.

From these results, we concluded that the CuO powder evaporates primarily as Cu_2O and undergoes re-oxidization in ambient conditions. The physical explanation for this behavior is that Cu_2O has a melting point of 1235 °C while CuO's melting point is 1446 °C, giving Cu_2O a higher vapor pressure and making it more likely to distill from the mixture.[86] The initial film has stress that relaxes as oxygen is absorbed. Despite the variability in the initial oxidation state, the films eventually stabilize to the refractive index shown in Figure 14. The imaginary part of the index is flat across the visible spectrum, matching the conditions required for a black color like CuO powder demonstrates.

Fe_2O_3 spectra in Figure 15c-d show that both fresh and aged films have almost identical compositions. After comparing these results to reported Fe_2O_3 spectra, we determined that the films are nearly 100% Fe(III) with no lower oxidation states.[71,88,89] Although the deposited film is predominantly Fe_2O_3, the remaining solidified crucible melt showed some dissociation. XPS analysis in Figure 15c-d of the solidified melt revealed 2p peaks resembling magnetite (Fe_3O_4).[71,88,89] The reason that Fe_2O_3 evaporates alone despite the presence of Fe_3O_4 is that Fe_2O_3 has a melting temperature is 1565 °C, while Fe_3O_4 melts at 1597 °C.[86] Thus, Fe_2O_3 has a higher vapor pressure and is preferentially distilled. This result demonstrates that e-beam evaporation's distillation preferences can overcome small differences in melting temperature, thereby avoiding oxide dissociation in the deposited film.

XPS spectra for the CuO-Fe_2O_3 mixture (green) in Figure 15 indicate the presence of both Cu(0) and Cu(I) atoms, supporting the observed refractive index behavior. While Cu(0) and Cu(I) have indistinguishable 2p spectra, their Auger peak shapes differ. Metallic copper's Auger peak contains small tooth-like ridges, and these ridges are present in the mixed absorber LMM Auger spectrum inset in Figure 15a. This Auger spectrum appears like a mix of reported Cu(0) and Cu(I) spectra.[90] The O 1s peak was consistent with lattice oxygen for copper oxide films. Additionally, the iron XPS peak shape in Figure 15c was unfamiliar, making quantitative analysis difficult. However, given that the refractive index trends align with those of CuO and Cu, the presence of iron appears to be insignificant.

By combining these two oxide powders, we successfully deposited a metallic copper oxide layer with k values between 2 and 3. Since Cu(I) was present in the film, similar to the fresh CuO films, it oxidized with exposure to air. The impact on the refractive index was small in comparison to pure CuO, though, resulting in variations of 0.2 to the refractive index. Additionally, this film's resistance was measured to be 220 Ohms five months after deposition, further supporting the metallic stability. This result is significant because it demonstrates that e-beam evaporation can distill metallic copper from raw oxide powders. Instead of using expensive refined metal starting materials, the evaporation process can refine materials into metals during deposition.

2.5.6 High-Chroma Color with Abundant Minerals

The mixture of CuO and Fe_2O_3 ceramic powders provided a metallic copper oxide film that is an excellent candidate for the HLA absorber layer. We deposited a 100nm layer of this film on a glass substrate, followed by SiO_2 and a 40nm TiO_2 layer, as shown in Figure 16. The SiO_2 and TiO_2 layers were also derived from ceramic powders. The TMM simulations in Figure 16 closely approximated the measured reflectance spectra. The differences were primarily due to the real

refractive index of the absorbing layer, which fluctuated by about 0.2 between samples. These differences resulted in reflection variations by, at most, 10%. Overall, the chromas of these coatings were in agreement with those on silicon, exhibiting similar reflection peaks around 60%. In addition, three of these structures achieved critical coupling, demonstrated by their reflectance spectra reaching zero at the resonant wavelength. This work demonstrates that vibrant structural colors can be achieved using entirely ceramic powders, significantly reducing the cost of source materials for e-beam evaporation.

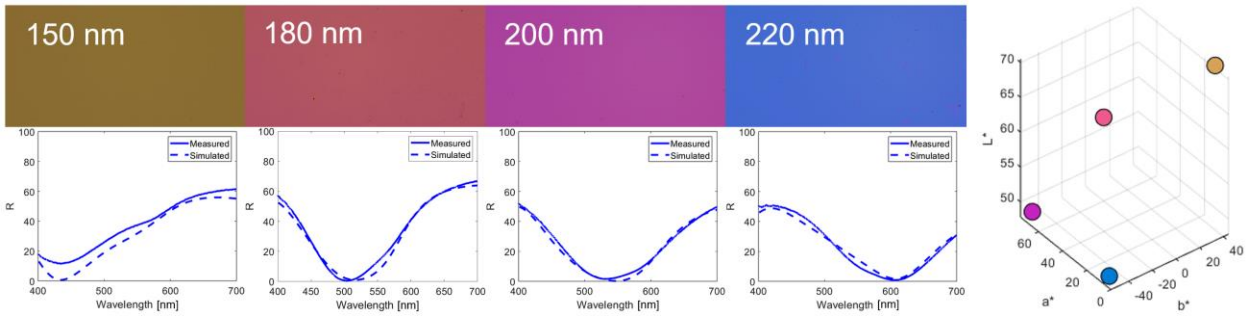


Figure 16. High-chroma HLA coatings from abundant minerals with a metallic copper oxide absorbing film.

2.6 Cost and Environmental Benefits of Mineral-Based Structural Colors

Material cost is a major expense in thin film deposition, but so is the deposition technique. Solution processing is significantly cheaper than physical vapor deposition (PVD) or chemical vapor deposition (CVD) techniques, but it requires starting materials in solution form.[31,91,92] CVD techniques require the starting materials to be in a gas state. The most common PVD techniques are sputtering, pulsed laser deposition, and evaporation. Sputtering uses Argon plasma to knock off atoms from a solid target, but raw materials cannot be easily formed into a sputtering target without significant expenses. Pulsed laser deposition ablates molecules from the target but is unable to deposit large areas and is slow.[93] Evaporation is the remaining option, using either resistive (thermal) or e-beam heating to melt the starting material.

E-beam evaporation is preferred since the e-beam can be swept over the surface of the starting material, ensuring even heating for a stable deposition. While e-beam evaporation is expensive due to high voltage and vacuum requirements, two methods were used to reduce these costs. First, a high deposition rate reduced the total processing time and thus the energy used for maintaining the vacuum level and high voltage filament. Second, repeatable films with good optical quality were deposited in pressures as high as $5 \cdot 10^{-2}$ Pa, reducing the need for powerful turbo pumps. Considering these improvements, along with the intrinsic distillation behavior, e-beam evaporation is a very advantageous deposition method for raw materials.

Chapter 3 Advanced Structural Color Applications

3.1 Introduction to Advanced Structural Color Applications

Structural color coatings offer a versatile and sustainable alternative to traditional pigment-based coatings, with applications ranging from decorative finishes to functional optical devices. This chapter explores three advanced approaches to enhancing the functionality, durability, and aesthetic versatility of structural color coatings.

The first section focuses on black structural color coatings using a multilayer thin-film structure designed to minimize optical reflection across the visible spectrum. By combining dielectric and metallic layers in a carefully optimized configuration, Dielectric-Metal-Dielectric-Metal (DMDM) structures achieve low reflectance, offering a sustainable alternative to traditional black finishes used in decorative and functional applications.

The second section discusses thermochromic structural color coatings, which use the thermo-optic effect to achieve reversible temperature-sensitive color changes. These coatings demonstrate potential for use with temperature sensors and integrated optical systems through tunable optical properties.

The final section examines the process of glass fusing structural color films, a method to enhance the durability of structural color coatings. This approach adapts glazing techniques from pottery, integrating structural color films into glass surfaces to create robust and aesthetically appealing coatings suitable for applications such as decorative windows and solar panel covers.

The conformal deposition of structural black coatings and the patterning of thermochromic layers were made possible through advanced additive manufacturing techniques,

which ensure high resolution and uniformity on complex surfaces. Together, these advancements highlight the versatility of structural color technologies to address practical challenges while expanding their use across industries.

3.2 Structural Black

3.2.1 Piano Black in Industry

Structural color coatings are known for their high color purity, which makes them ideal for creating visually striking appearances. These coatings can also be used to produce black coatings with minimal or no optical reflection. Black, especially piano black, is a highly desirable color for functional coatings, valued for its premium, glossy appearance. Piano black typically refers to a deep black coating with a slight reflection (around 10%) and is commonly used in decorative plastic components, such as those found in automotive interiors.[54] Current methods for achieving piano black include glossy spray paints made with organic pigments. However, these paints degrade over time, are wasteful, and pose hazards to workers due to their toxic chemical components. This highlights the need for alternative, safer, and more sustainable coating designs.[94]

Physical vapor deposition (PVD) methods offer a promising alternative, producing smooth, durable black coatings with greater longevity. For example, black coatings made using PVD with ceramic materials containing carbon, oxygen, and chromium have been demonstrated.[54] However, these coatings require a large thickness of 1 μm for a piano black appearance. Therefore, alternative materials are necessary for creating cost-effective, high-performance black coatings. One potential solution is the use of thin film stacks designed to achieve absorption resonance across the visible spectrum, enabling high absorption with minimal reflection.

3.2.2 Overview of the DMDM Structure

The Dielectric-Metal-Dielectric-Metal (DMDM) structure is a thin-film structure capable of achieving near-zero optical reflection. Similar to the MDM structure, the DMDM structure contains an asymmetric Fabry-Pérot cavity, with the addition of an anti-reflection dielectric layer on top. For optimal performance, the structure uses a reflective base layer, such as aluminum, combined with a thin, lossy metal layer like titanium. In this specific structure, the aluminum base is 100 nm thick, followed by an 86 nm SiO_2 cavity layer, a 10 nm titanium layer, and a 77 nm SiO_2 anti-reflection layer. A schematic of the structure, including the silicon substrate, is shown in Figure 6a. Because the structure is built on an optically thick aluminum layer, the underlying substrate can be any planar material.

3.2.3 Deposition and Characterization of Structural Black Films

The DMDM structure was fabricated using electron-beam evaporation in an Angstrom Engineering Evovac system. All layers were deposited at a rate of 3 A/sec during a single vacuum pump cycle at $5 \cdot 10^{-4}$ Pa. The reflectance spectrum of the resulting film was measured using an Ocean Optics Inc. HR4000CG-UV-NIR High-Resolution Spectrometer integrated with a white light source. The results, shown in Figure 17, include the reflectance spectrum and a camera image of the deposited stack, confirming its low reflection in the visible spectrum. Extending the spectrum into the ultraviolet range reveals that the structure is a strong reflector around 300 nm, while in the infrared range, reflectance gradually increases with wavelength. Such optical behavior is valuable for any coating to prevent UV damage. These results demonstrate the potential of DMDM structures to be used as durable, smooth black coatings. The combination of minimal

visible reflectance, excellent durability, and tunable optical properties makes them highly suitable for functional and decorative applications.

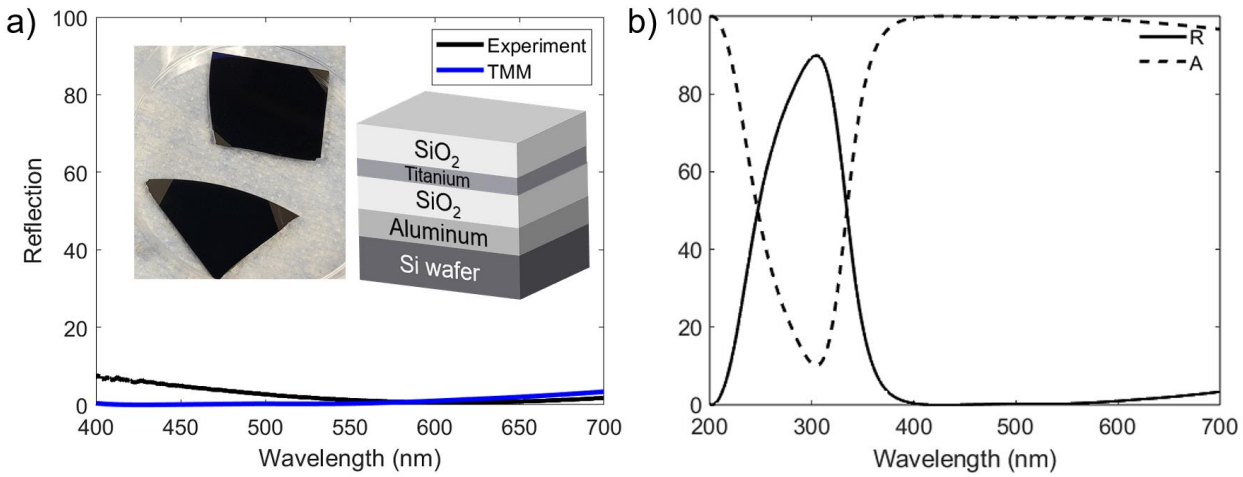


Figure 17. Structural black using the DMDM structure. Reflection spectra for a) visible wavelengths and expanded to b) ultraviolet wavelengths indicate near-zero visible reflection.

3.3 Thermochromic Structural Color Coatings

3.3.1 Overview of Thermochromic Coatings

Thermochromic coatings are materials that change color in response to temperature variations. These properties have numerous applications, such as in transition eyeglasses and smart windows, which reduce light transmission when heated by sunlight. Another familiar example is mood rings, which utilize liquid crystals made from organic polymers that change color with body temperature.[95] These color shifts serve not only as temperature indicators but also as mechanisms for aesthetic adaptation to different environments.

Several thermochromic materials are currently being studied. For instance, vanadium oxide has been embedded in glass or used as a thin film for thermochromic applications.[96,97] Similarly, polymer thin films, such as poly(3-alkylthiophenes), undergo phase transitions near room temperature.[98,99] However, both approaches have significant drawbacks. Vanadium oxide

is hazardous due to its carcinogenic properties, while poly(3-alkylthiophenes) are susceptible to oxidation and photodegradation, compromising the film's integrity.[100] Additionally, while color changes in these polymer films are reversible, they typically require heating or nucleation rather than responding to ambient temperature changes. For these reasons, alternative thermochromic materials are necessary for sustainable, safe, and long-lasting coatings.

3.3.2 Overview of the Thermo-Optic Effect

The primary mechanism underlying thermochromic behavior in inorganic materials is the thermo-optic effect, where a material's refractive index changes with temperature. Although all materials exhibit this effect to some extent, it is more pronounced in specific materials. The thermo-optic effect can be understood using the Lorentz-Lorenz equation:[101]

$$\frac{n^2 - 1}{n^2 + 2} = \frac{\rho(T)\alpha(\rho, T)}{3\epsilon_0}$$

Eqn. 3-1

where n is the refractive index, ρ is the material density, α is the polarizability, and T is the temperature. Taking the derivative with respect to temperature, the thermo-optic coefficient ($\frac{dn}{dT}$) is proportional to:

$$\frac{dn}{dT} \propto \frac{d\rho(T)}{dT}\alpha(\rho, T) + \rho(T)\frac{d\alpha(\rho, T)}{dT}$$

Eqn. 3-2

The first term, associated with thermal expansion, is typically negative because density decreases as temperature increases. The second term, related to polarization changes, is usually positive. The overall thermo-optic coefficient can be positive or negative, depending on the relative strengths of these effects. For example, SiO_2 has a small positive coefficient ($8 \cdot 10^{-6}$ K^{-1})[102] because polarization effects dominate over thermal expansion. In contrast, TiO_2 exhibits a

large negative thermo-optic coefficient ($-7 \cdot 10^{-4}$ K^{-1})[103] at room temperature, making it an intriguing material for studying strong thermo-optic behavior.

3.3.3 Deposition and Characterization of Thermochromic TiO_2 Films

Thick TiO_2 films (>200nm) were deposited using e-beam evaporation at a rate of 3 A/sec onto silicon substrates. When heated on a hot plate, the films displayed noticeable color changes, as seen in Figure 18a. The refractive indices of the films were measured using spectroscopic ellipsometry, with heating provided by a thermoelectric heater. These measurements indicated a thermo-optic coefficient of $-1 \cdot 10^{-3}$ K^{-1}. Reflectance spectra, obtained with an Ocean Optics Inc. HR4000CG-UV-NIR High-Resolution Spectrometer, confirmed a thermally induced shift in reflectance, as shown in Figure 18c. Simulations performed using the Transfer Matrix Method (TMM) in MATLAB (Figure 18d) accurately reproduced these shifts by reducing the refractive index of the heated film by 0.07, consistent with the measured thermo-optic coefficient. These results demonstrate that thick TiO_2 films follow the thermo-optic effect and exhibit predictable color changes with temperature.

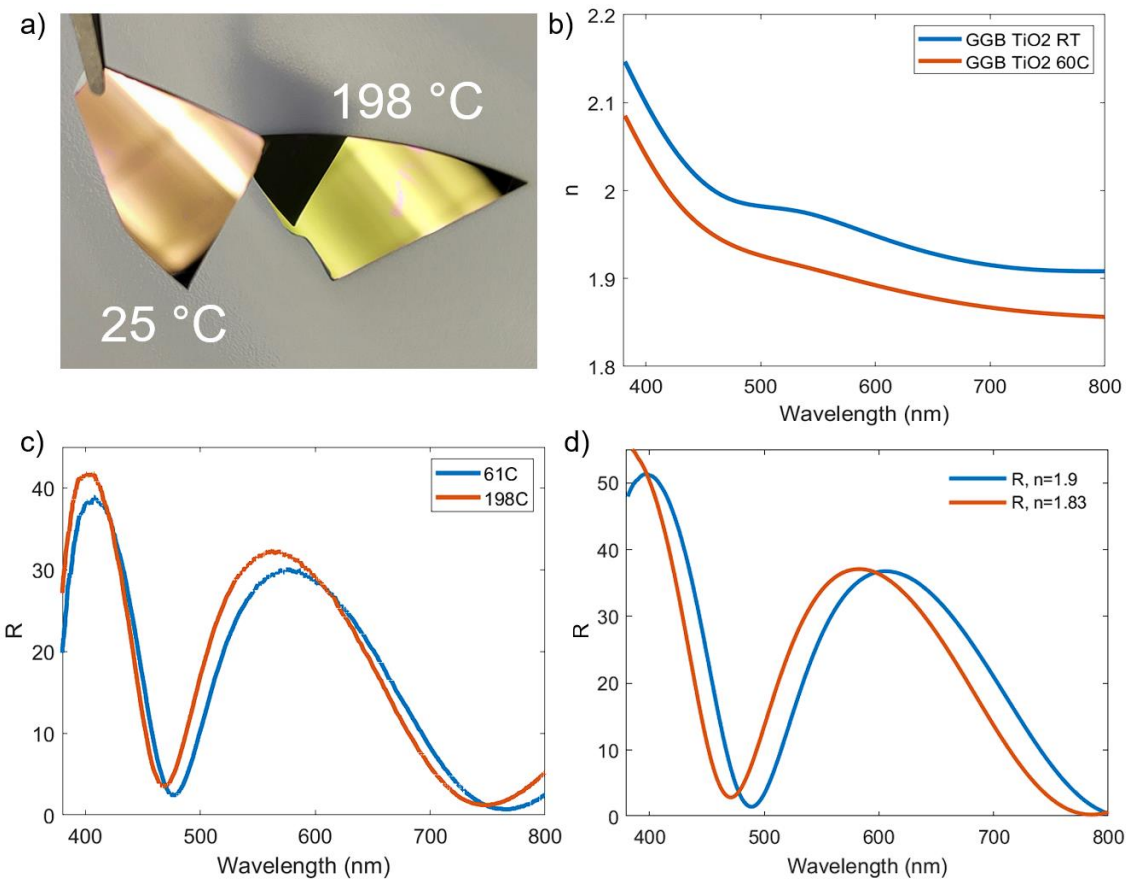


Figure 18. The thermo-optic effect in thick TiO_2 films. a) Camera images, b) refractive index data, c) measured reflectance spectra, and d) simulated reflectance spectra.

3.3.4 Thermal Sensing with Thermochromic Structural Colors

Although TiO_2 films exhibit a measurable thermo-optic effect, the reflectance shifts are relatively small. For example, a 100 °C temperature change shifts reflectance peaks by only about 10 nm, which does not result in a significant overall color change. However, if steep reflection slopes are present, even small shifts can lead to noticeable changes in reflectance at specific wavelengths. To enhance sensitivity, 200 nm TiO_2 films can be combined with an SiO_2 cavity layer, as shown in Figure 19. By tuning the thickness of the SiO_2 layer, the position of the reflection slopes can be adjusted to amplify the color change. Optical microscope images reveal clear color transitions with a 75 °C temperature shift, demonstrating the potential of this approach.

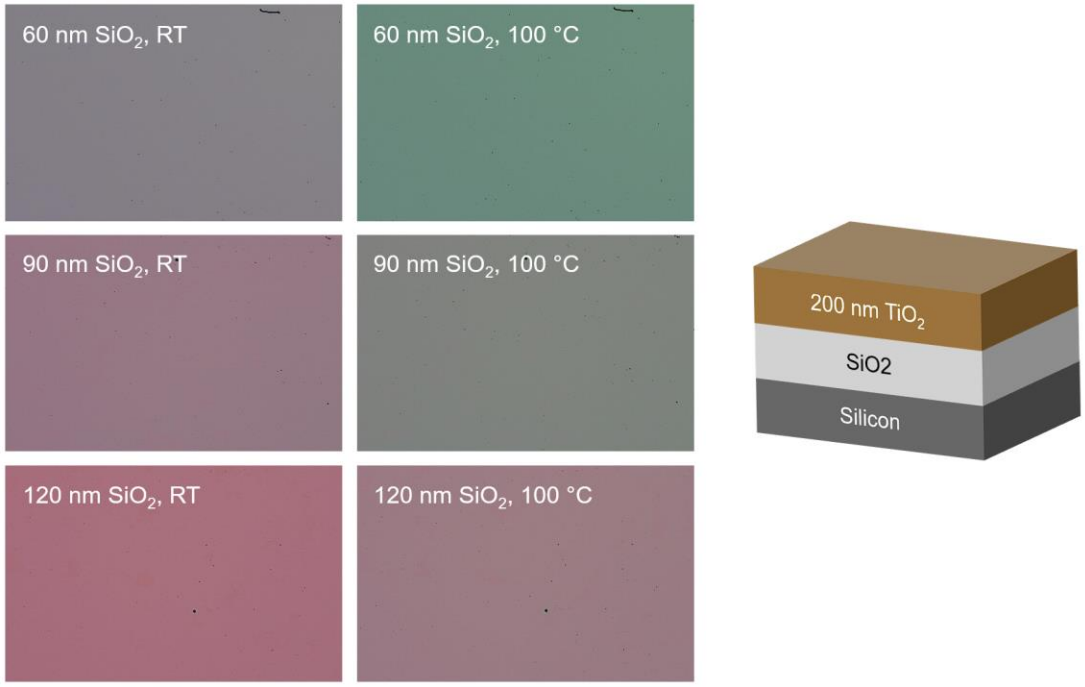


Figure 19. Color change in thick TiO_2 films, adjusted by tuning the SiO_2 layer thickness, between room temperature (RT) and 100 °C.

Such tailored coatings can serve as thermal sensors in electronic systems. For example, in integrated optics, where laser coupling is used to transfer information, a coating with steep reflection slopes at the operating wavelength can improve sensitivity to temperature variations as thresholds are crossed. Furthermore, when deposited on metallic substrates, these coatings can function as resistors in electronic circuits. The passing current heats the substrate, and the resulting color change provides a visual indication of the temperature for similar resistance components.

Two of these structures were deposited on 50 nm Ni layers, with SiO_2 thicknesses of 100 nm and 170 nm, resulting in gold and magenta coatings, respectively. The samples were heated on a hot plate, and their reflectance spectra are shown in Figure 20a-b. As indicated by the red lines, an operating wavelength of 532 nm exhibits a reflection change of approximately 10% when heated to 200 °C.

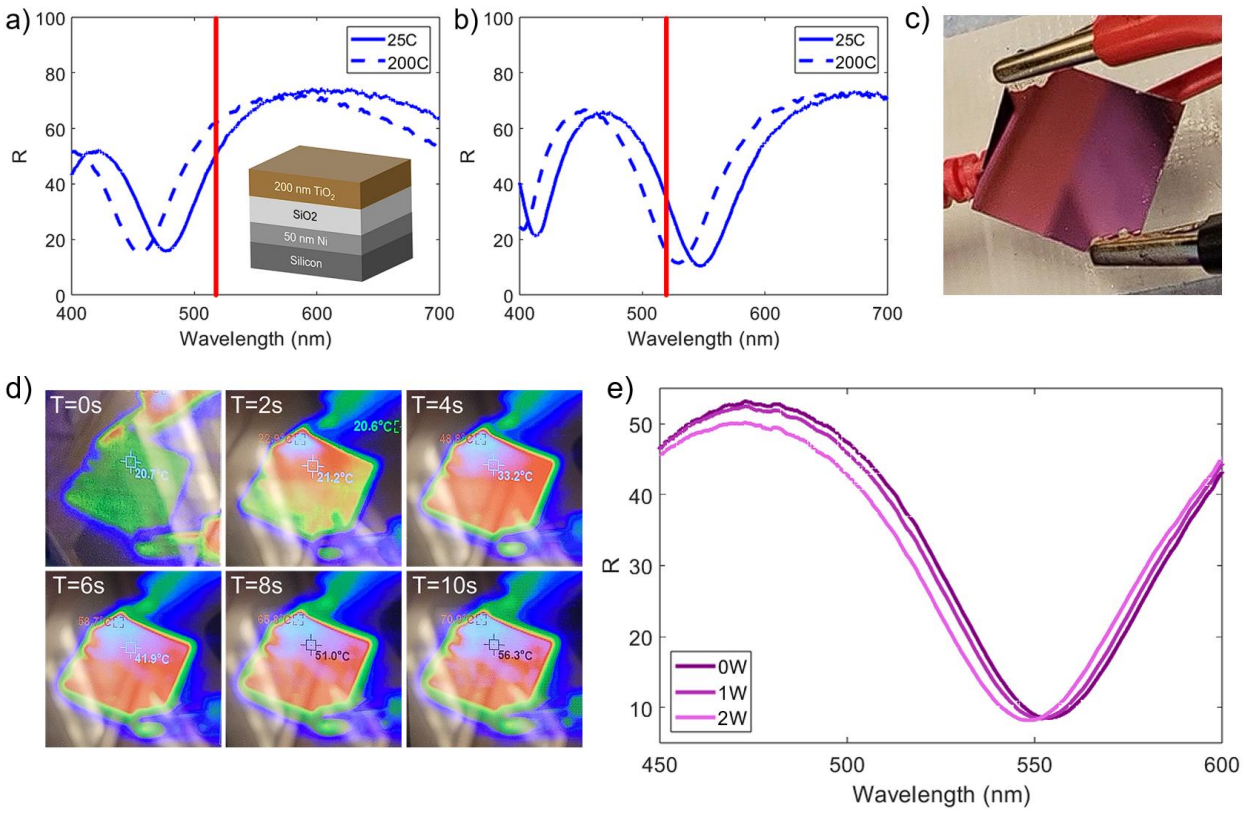


Figure 20. Thermochromic TiO_2 coatings used as temperature sensors. a) and b) show the temperature shift in two HLA structures with varying SiO_2 cavity thicknesses. c) is a camera image of the sample in b). d) and e) exhibit color change based on Joule heating.

The magenta sample was scratched at the corners to expose the underlying Ni layer, and silver paste was applied to ensure good electrical contacts. Power supply leads were connected, as shown in Figure 20c, and the temperature of the sample was measured on the backside using a TOPDON ITC629 infrared camera. The power supply output was 10V at 0.18A, delivering 2.2W of power to the Ni layer and raising its temperature by 25.4 °C in 10 seconds, as shown in Figure 20d. The shift in reflectance spectra was recorded in Figure 20e for 5V and 10V at 0.18A applied over 15 seconds, demonstrating that this structure can operate as a thermal sensor when integrated as a resistor.

The heating time is directly related to the heat capacity of the sample, which is the cumulative heat capacity of its layers: silicon, nickel, SiO_2, and TiO_2. By accounting for convection and radiation heat losses, the heating time can be calculated as follows:

$$C_{Total} = \sum_i C_{,i} = \sum_i \rho_i \, V_i \, c_i$$

$$Q_{heat} = C_{Total} \, \Delta T$$

$$P_{net} = P_{input} - Q_{conv} - Q_{rad} = VI - h \, A \, \Delta T \, - \sigma \epsilon A \left(T_{sample}^4 - T_{air}^4 \right)$$

$$t = \frac{Q_{heat}}{P_{net}}$$

(Assuming: $Bi = \frac{h \, d}{k} < 0.1$)

Eqn. 3-3

Here, C is the heat capacity, ρ is the layer density, V is the layer volume, c is the layer's specific heat, Q_{heat} is the energy gained as heat, T is the temperature, P is the power, V is the applied voltage (10V), I is the applied current (0.18A), h is the convective heat transfer coefficient (assumed to be 10 $W/m^2 \cdot K$ for natural convection), A is the total sample surface area ($1.3 \cdot 10^{-3}$ m^2), σ is the Stefan-Boltzmann constant, and ϵ is the emissivity of the sample (assumed to be 0.45 as an average of silicon and TiO_2).[86] By using standard material densities and specific heats, as well as $\Delta T = 25.4$ °C, the calculated heating time from *Eqn. 3-3* is 9.6 seconds, consistent with the Figure 20d. However, contact resistance was not factored into the calculation and is likely the source of this minor underestimation.

This calculation is a lumped capacitance model, which treats the substrate as a system with uniform temperature. Materials with a Biot number (Bi) below 0.1 can be reasonably approximated this way. The Biot number is calculated using the heat transfer coefficient ($h = 10$

$W/m^2 \cdot K$), the thickness (d), and the thermal conductivity ($k = 1$ W/m·K for glass). Both glass and silicon have Biot numbers below 0.1.

When the TiO_2-SiO_2-Ni coating is deposited on a 1 mm glass substrate instead of silicon, the heating time increases to 25 seconds due to the higher heat capacity of the glass. For a 0.17 mm glass cover slip, the heating time decreases to 4.2 seconds, and if the film is suspended without a substrate, the heating time reduces further to 0.011 seconds. These findings highlight the versatility of TiO_2-based thermochromic coatings for thermal sensing and their potential integration into advanced optical and electronic systems.

3.4 Glass Fusing Structural Color Films

3.4.1 Overview of Glass Fusing

While structural color coatings can be deposited on various substrates, they often require enhanced durability and scratch resistance for functional applications. Many thin film stacks can be easily scratched due to poor adhesion to the substrate, which can compromise their appearance. Methods to improve the durability of these coatings include encapsulation with clearcoat polymers, polycarbonates, or scratch-resistant dielectric top layers.[104,105] However, these methods typically require additional layers or structural changes, which can increase complexity and cost. An alternative solution is to fuse structural color coatings to glass, which preserves their vibrant colors while significantly improving durability. This method also serves as a potential technique for creating decorative windows or protective covers for solar panels.

The process of fusing glass draws inspiration from pottery. In pottery, before the clay is fired, a glaze is applied to the exterior. This glaze contains ground silica mixed with oxides to reduce the glaze melting point and sometimes produce color. The glaze offers both aesthetic and functional purposes by providing color and waterproofing the clay. During firing, the glaze melts

and bonds to the clay surface at temperatures around 700 °C. This concept can be adapted for glass fusing, as ordinary glass remains stable at these temperatures, and many structural color films can also withstand such heat. For the best results in fusing structural color films to glass, a thin, uniform, and transparent glaze layer is essential.

3.4.2 Spin Coating and Fusing Structural Color Flakes

To achieve a thin and uniform glaze layer, a white glaze powder that becomes transparent upon firing was spin coated onto glass slides. The glaze powder was first combined with water to form a 1.5 g/mL suspension, which was then sonicated in an ultrasonic bath to remove any clumps prior to spin coating. While the suspension was being sonicated, the glass slides were cleaned using acetone, isopropanol, then deionized water. The prepared glaze suspension was then spin coated onto the glass at 750 rpm for 60 seconds, yielding the coating shown in Figure 21a.

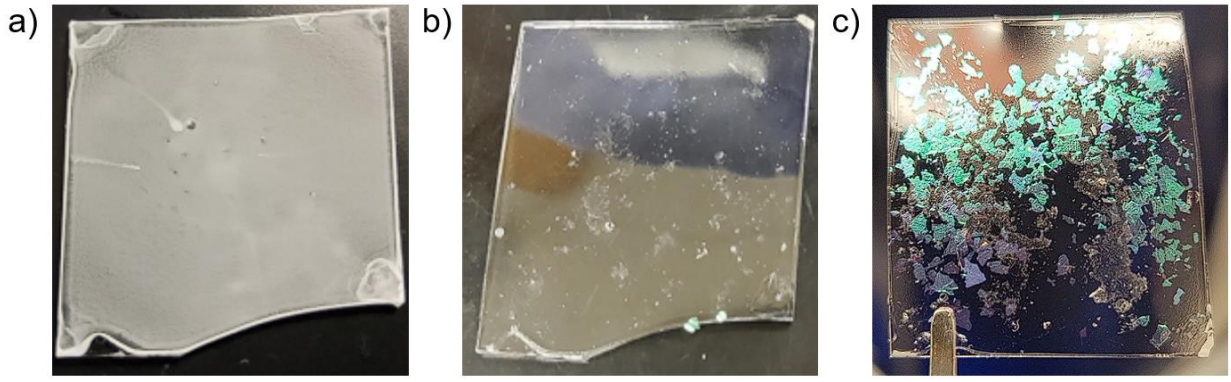


Figure 21. Clear glaze film a) before and b) after firing at 700 °C. c) Color flakes fused to clear glaze film.

Structural color films can be integrated into the glaze layer using multiple methods. For high-throughput manufacturing, the colored film can first be deposited onto a sacrificial layer, such as polyimide, and then placed onto the glaze layer. The sacrificial layer either burns away as ash during firing or is removed with solvents prior to baking. Alternatively, the structural

color film can be broken into flakes for easier application. To demonstrate this process, structural color flakes provided by Inlight Technologies were sprinkled onto the glaze layer. After baking at 700 ℃ for 60 seconds, the flakes fused to the glass surface, creating a durable and scratch-resistant coating as shown in Figure 21c. Even when scratched with a fingernail or tweezers, the flakes did not mar. This approach highlights the potential of glass fusing as a robust method to preserve and protect structural color coatings while enhancing the aesthetic appeal of glass surfaces.

Chapter 4 Patterning and Conformal Coatings with Area-Selective Atomic Layer Deposition

4.1 Introduction to Conformal Coatings and Patterning Techniques

4.1.1 Overview of Atomic Layer Deposition and Conformal Coatings

Traditional thin-film deposition methods often face tradeoffs between conformality, thickness control, and versatility in material selection. For example, physical vapor deposition (PVD) techniques struggle to deposit conformal films on complex 3D structures with high aspect ratios, while electrodeposition is limited to electrically conductive materials.

Atomic layer deposition (ALD) offers a solution to these challenges as a vapor-phase process that provides exceptional control over film thickness and conformality.[106,107] Studies have shown that ALD can produce uniform coatings on structures with ultra-high aspect ratios (>50,000:1)[108] and can conformally coat complex surfaces without variations in film thickness or composition.[109–113] Furthermore, many ALD processes operate at relatively low temperatures (typically below 250 °C), making them compatible with a wide range of materials, including flexible polymers or organic templates.[109,114,115]

Recent advancements in Spatial Atomic Layer Deposition (SALD) have further improved the throughput of ALD by several orders of magnitude, enabling compatibility with roll-to-roll manufacturing.[116–118] These attributes make ALD an ideal method to integrate with additive manufacturing processes such as 3-D printing, as it can conformally coat complex surfaces with sub-nanometer precision in composition, thickness and structure. However, the integration of ALD with additive manufacturing remains in its infancy.[119,120]

In addition to its advantages in conformality and material versatility, ALD enables precise control over coating properties at the nanoscale, which is crucial for applications that require intricate designs or patterns. Structural color coatings, in particular, benefit from such precision, as patterning plays a key role in expanding their aesthetic and functional applications.

This chapter is adapted from Rorem et al., "Integrating Structural Colors with Additive Manufacturing Using Atomic Layer Deposition", ACS Applied Materials & Interfaces, **14**, pg. 31099 – 31108, 2022. This work was done in collaboration with Tae H. Cho, Nazanin Farjam, Julia D. Lenef, Kira Barton, Neil P. Dasgupta, and L. Jay Guo.

4.1.2 Importance of Patterning in Structural Color Applications

Patterned structural colors offer many advantages, with one of the most straightforward being the ability to create multicolor designs for aesthetic purposes. By depositing different colors in distinct regions of a single coating, detailed designs are possible without relying on traditional pigments or dyes. Patterning vibrant structural colors enables the creation of visually striking, high-resolution patterns for fashion, interior design, and automotive surfaces. Furthermore, structural colors often exhibit angle-dependent appearance changes, producing interesting visual effects when combined with intricate patterns.

Beyond aesthetic appeal, precision patterning enhances the functionality of structural color coatings. High-resolution patterns are essential for fabricating photonic and optoelectronic devices such as diffraction gratings and color filters. Additionally, patterned structural colors are difficult to replicate, making them valuable for anti-counterfeiting measures and authentication technologies. Emerging applications further highlight their versatility, including wearable devices that integrate both aesthetic and functional displays or adaptive camouflage.

Achieving high-resolution patterns in structural color coatings requires advanced deposition techniques that allow selective control over material placement. Area-selective ALD (AS-ALD), combined with electrohydrodynamic-jet (e-jet) printing, provides a powerful approach to fabricate these patterns with nanoscale precision.

4.1.3 Principles of AS-ALD and E-Jet Printing

While the ability of ALD to uniformly coat the entire surface of 3D objects is beneficial in many applications, there are cases where selective deposition in specific areas is preferred. Selective deposition can be achieved through area-selective ALD (AS-ALD), which uses surface modifications to inhibit the ligand-exchange reactions between precursor molecules and surface functional groups.[121–131] Recent work has demonstrated that AS-ALD can be achieved using polymer inhibitors deposited through electrohydrodynamic jet (e-jet) printing.[4,132–134]

Although inkjet printing has been used to create multicolor prints on the same sample,[135] e-jet printing offers significant advantages over inkjet technology. Advantages include the ability to print a wider range of materials, such as viscous polymers, conductive nanoparticle suspensions, and biomaterials, as well as achieving sub-micron resolution in the x-y plane, which is far superior to the typical >50 μm resolution of ink-jet processes. Combining e-jet printing with AS-ALD enables additive nanomanufacturing with sub-100 nm resolution in the x-y plane and sub-nm precision in the z-direction.[136–138] Furthermore, while traditional printing methods are often limited by the availability of compatible inks, ALD provides a versatile range of functional materials, including metals, metal oxides, sulfides, nitrides, and polymers, with tunable electronic, optical, and mechanical properties.[139]

The optical properties of additively manufactured parts are typically limited by the source materials used, such as inks or powders. While some surfaces can accommodate paints or dyes,

these processes are often unable to conformally coat high-aspect-ratio geometries, require specific chemical compatibilities, and are susceptible to fading or delamination in ambient environments. To overcome these challenges and separate the geometric properties of a printed object from its optical response, structural colors are integrated with additive manufacturing through ALD-based surface modifications. This approach offers a durable and precise solution for creating vibrant, high-performance coatings on complex geometries. By combining AS-ALD with additive manufacturing, this work demonstrates a scalable approach for conformal coatings on irregular geometries and intricate patterns, advancing the capabilities of AM for photonics and electronics.

4.2 Materials and Process Parameters in AS-ALD for Structural Colors

4.2.1 Materials Selection for Multilayer Structural Color Coatings

To demonstrate the ability to tune structural colors using ALD, ZnO films were deposited with varying numbers of ALD cycles on a silicon substrate.[4] The multilayer structure consisted of a Ni bottom layer and a Cu top layer, with ZnO as the dielectric in between, representing an MDM structure. As discussed in sections 1.2.2 and 1.3.2., the MDM structure is a simple, vibrant coating. ZnO was chosen as the dielectric layer due to its wide bandgap (3.3 eV), relatively flat refractive index (~2), and reliable ALD deposition process. Cu was selected as the top metal layer because of its well-characterized ALD process, ease of tunability, and favorable optical absorption properties for MDM structures.[25] The base layer was a 50 nm Ni film deposited by e-beam evaporation onto a silicon substrate. Ni was selected for its high reflectivity and broadband optical properties, although, as demonstrated later, this process is adaptable to various substrates and metals.

A cross-sectional scanning electron microscopy (SEM) image of a representative MDM structure fabricated by ALD is shown in Figure 22a, with a schematic representation in Figure 22b. This particular structure had a dielectric thickness of 120 nm and a Cu top layer thickness of 20 nm, both precisely controlled by adjusting the number of ALD cycles. The flat and uniform boundaries between layers highlight the precise thickness control and conformal interfaces achievable with ALD.

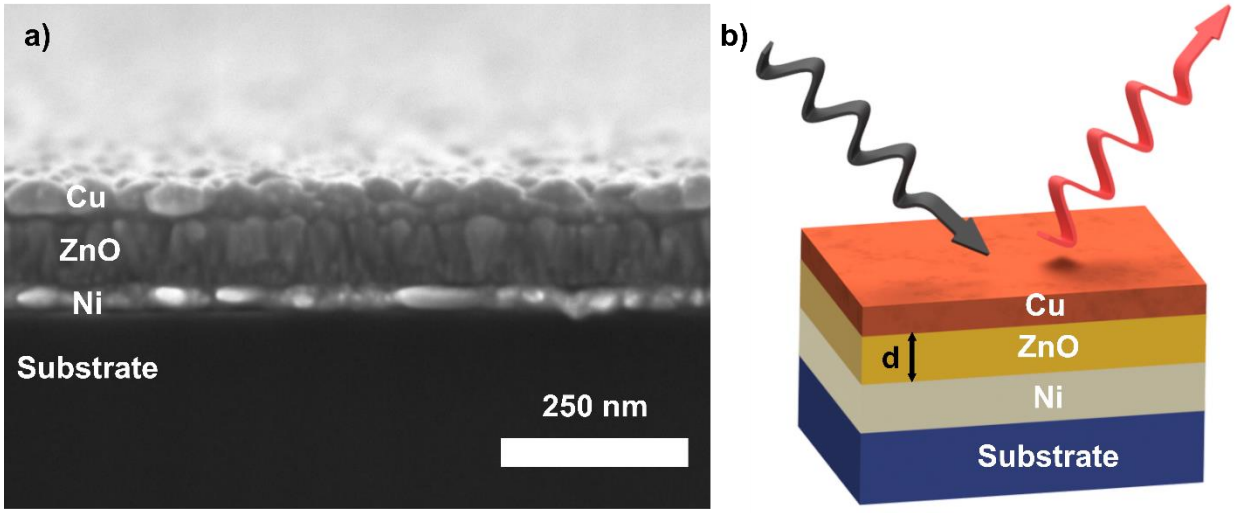


Figure 22. a) Cross-sectional SEM image of a deposited MDM structure and b) a schematic representation.

4.2.2 Process Parameters and Control in ALD

A custom-built, hot wall, cross-flow thermal Atomic Layer Deposition (ALD) reactor was used to deposit ZnO on the substrates. Diethylzinc (DEZ, Sigma-Aldrich, ≥52 wt% Zn basis) served as the metalorganic precursor, and deionized (DI) water was used as the oxidant. Both precursors were maintained at room temperature. The deposition temperature was set to 130 °C, with Argon (Ar) as the carrier gas at a flow rate of 70 sccm. Each ZnO deposition cycle consisted of a 0.05-second DEZ pulse followed by a 30-second purge, a 0.1-second DI water pulse, and

another 30-second purge. This cycle was repeated until the desired ZnO thickness was achieved. The average growth rate on silicon substrates was measured to be 2 Å/cycle.

Cu ALD films were deposited using a Veeco Fiji G2 flow-type ALD system with $[Cu(^{s}Bu\text{-}amd)]_2$ as the Cu precursor and hydrogen plasma at 300 W. The precursor source temperature was maintained at 110 °C using a bubbler setup. Depositions were performed at 185 °C with Ar as the carrier gas at a flow rate of 110 sccm. Each Cu ALD cycle included a 3-second Cu precursor pulse, an 8-second purge, a 10-second hydrogen plasma exposure at 300W, followed by another 8-second purge. The average growth rate for Cu films was measured to be 0.2 Å/cycle.

Fine-tuning deposition parameters is crucial for achieving consistent film thickness and conformality in ALD. Carefully controlled precursor pulse times, such as those for DEZ and DI water in ZnO deposition, ensure that surface reactions reach saturation, because incomplete saturation can result in uneven film thickness. Purging with Ar between precursor pulses removes residual molecules and by-products, preventing unwanted reactions. Additionally, maintaining the deposition temperature within an optimal range – high enough to facilitate surface reactions but below the precursor degradation temperature – ensures uniform growth and preserves film integrity. These examples illustrate the importance of precise parameter control in ALD.

4.3 Deposition of Conformal Structural Colors with ALD

4.3.1 Planar MDM Structures with ALD

The MDM structure described in section 4.2.1 was deposited with a range of ZnO thicknesses, as shown in Figure 23.[4] This range of ZnO thicknesses produced structural colors spanning the full visible spectrum. The ZnO layer thickness was gradually increased from 40 to 160 nm, while the top Cu layer remained at a constant thickness of 20 nm. Each color in Figure

23a is accompanied by its corresponding measured and simulated reflectance spectrum. The simulations, performed using a transfer matrix method (TMM), calculated the reflectance spectra for the tri-layer structure. To show the change in RGB values as a function of ZnO thickness, a CIE chromaticity plot is included in Figure 23b.

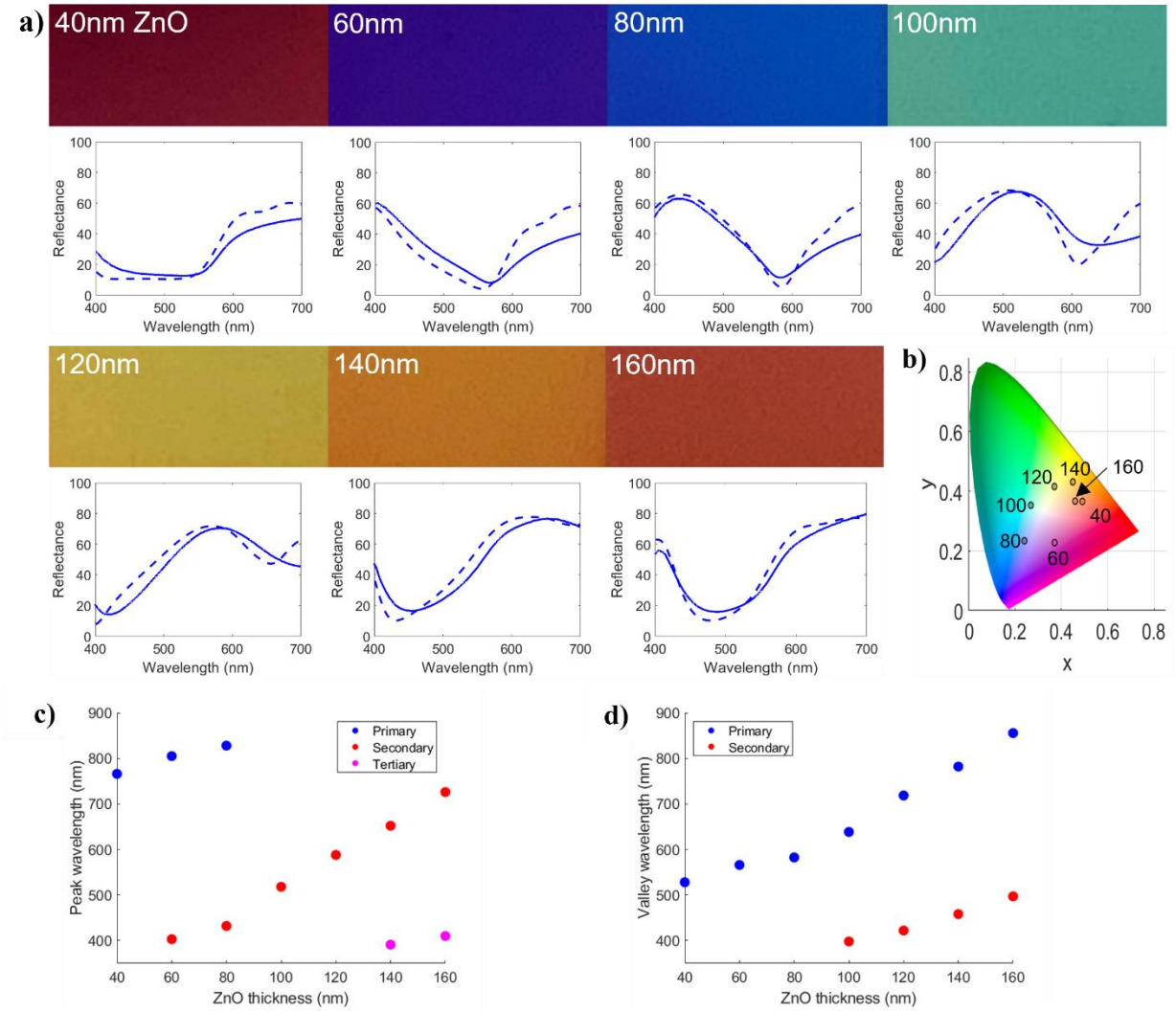


Figure 23. a) Structural colors produced by planar MDM stacks with varying ZnO thicknesses, including measured and simulated reflectance spectra. b) RGB values plotted on a chromaticity diagram. c) Reflection peaks and d) valleys as a function of ZnO thickness.

Figure 23 demonstrates that a full color cycle can be achieved by adjusting the dielectric layer thickness. For example, with a ZnO thickness of 40 nm, the sample exhibited a red color; at 100 nm, it shifted to green; and at 160 nm, it returned to red. The simulated and measured spectra

agreed well across the range of ZnO thicknesses. Most spectral peaks exhibited reflectance magnitudes of 70-80%, providing a strong contrast compared to the reflectance valleys at 10-20%. While slight deviations between the simulated and measured spectra were observed in the red wavelengths for ZnO thicknesses up to 120 nm, the overall spectral shapes remained consistent. These deviations are likely due to surface roughness in the ALD-deposited Cu top layer, which results from its well-studied island nucleation and growth mode on oxide.[140,141]

The CIE chromaticity plot in Figure 23b maps the RGB values derived from the simulated spectra, forming a complete revolution around the plot's center as the ZnO thickness increased from 40 nm to 160 nm. The sub-nanometer precision in ZnO thickness enabled by ALD allows for additional color points across the visible spectrum to be fabricated, further expanding the range of achievable structural colors. Although this study focused on ZnO thicknesses between 40 and 160 nm, similar cyclic color behavior is expected for larger dielectric thicknesses.

To further explore the relationship between color and ZnO thickness, the resonance peaks and valleys from Figure 23a were plotted in Figures 20c and 20d. These plots extend beyond the visible spectrum to provide additional data points. Both figures show that the resonance peaks and valleys shift linearly with increasing ZnO thickness, demonstrating that desired colors can be precisely achieved by selecting the appropriate peak or valley wavelength using this linear relationship.

As the dielectric layer thickness increased, the resonance peaks and valleys shifted toward longer wavelengths. Eventually, the primary extrema moved beyond the spectrometer's measurement range, and new secondary extrema appeared at shorter wavelengths. For example, the primary peak at 500 nm for a 100-nm-thick ZnO film shifted to 650 nm when the ZnO thickness was increased to 140 nm, eventually disappearing beyond the visible spectrum at greater

thicknesses. In the same spectrum for the 160 nm ZnO film, a secondary peak emerged at shorter wavelengths. Across the thickness range studied, primary, secondary, and tertiary resonance peaks were observed, along with primary and secondary valleys. Overall, the MDM structures deposited with ALD exhibited a linear relationship between reflectance peaks and valleys and ZnO thickness, illustrating precise and tunable control over structural color.

4.3.2 Conformal Structural Colors on Metal 3D-Printed Objects

To demonstrate the capability of ALD to apply structural color to non-planar, complex surfaces, MDM structures were deposited onto 3D-printed metal figurines of a wolverine, with an overall height of 15mm (Figure 24). The figurines were printed using Ultrafuse 17-4 PH stainless steel, which served as the base metal layer for the MDM structure. To produce a blue color on the surface, an 80 nm thick ZnO film was deposited. For yellow, a 120 nm thick ZnO film was deposited. These results align with those from Figure 23, showcasing the versatility of this technique to "paint" structural color onto various substrates.

After the deposition of the dielectric ZnO layer, a 20 nm Cu layer was added using ALD. Vibrant blue and yellow colors were observed on the 3D-printed structures, with uniform color coverage across all curved surfaces, as shown in Figure 24. As pictured in Figure 24c, the ALD coating conformally covered the microscopic porous surface features characteristic of metal 3D printing. This result highlights the advantages of conformal gas-phase deposition for applying color to additively manufactured objects, including the ability to uniformly coat complex surface topographies that would be extremely difficult to cover with traditional paints.

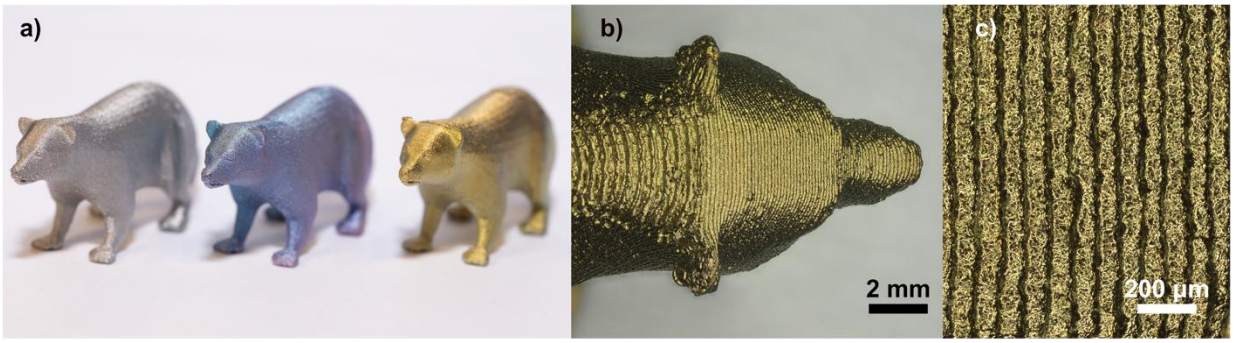


Figure 24. a) 3D-printed metal objects coated with MDM structures, including uncoated (left), 80 nm ZnO (middle) and 120 nm ZnO (right) samples. b-c) Optical microscopy images showing surface details.

To further assess the conformality of the MDM structures, 600 ALD cycles of ZnO and 1,000 ALD cycles of Cu were applied to etched Si trenches, as shown in Figure 25a-d. The coatings, measuring 120 nm thick ZnO and 20 nm thick Cu, uniformly covered the entire trench height, including both convex and concave surface features. Additionally, a 40 mm diameter glass dome and a polyimide sheet were colored using a Fabry-Pérot cavity with a 60 nm thick ZnO layer, as shown in Figure 25e-f. When comparing the reflectance spectra of the glass dome and polyimide with respect to a planar Si substrate, all samples exhibited similar absorption resonances at 566 nm. These results demonstrate the exceptional capability of ALD to impart structural color onto a wide range of substrates, including high-aspect ratio, non-planar, and flexible surfaces.

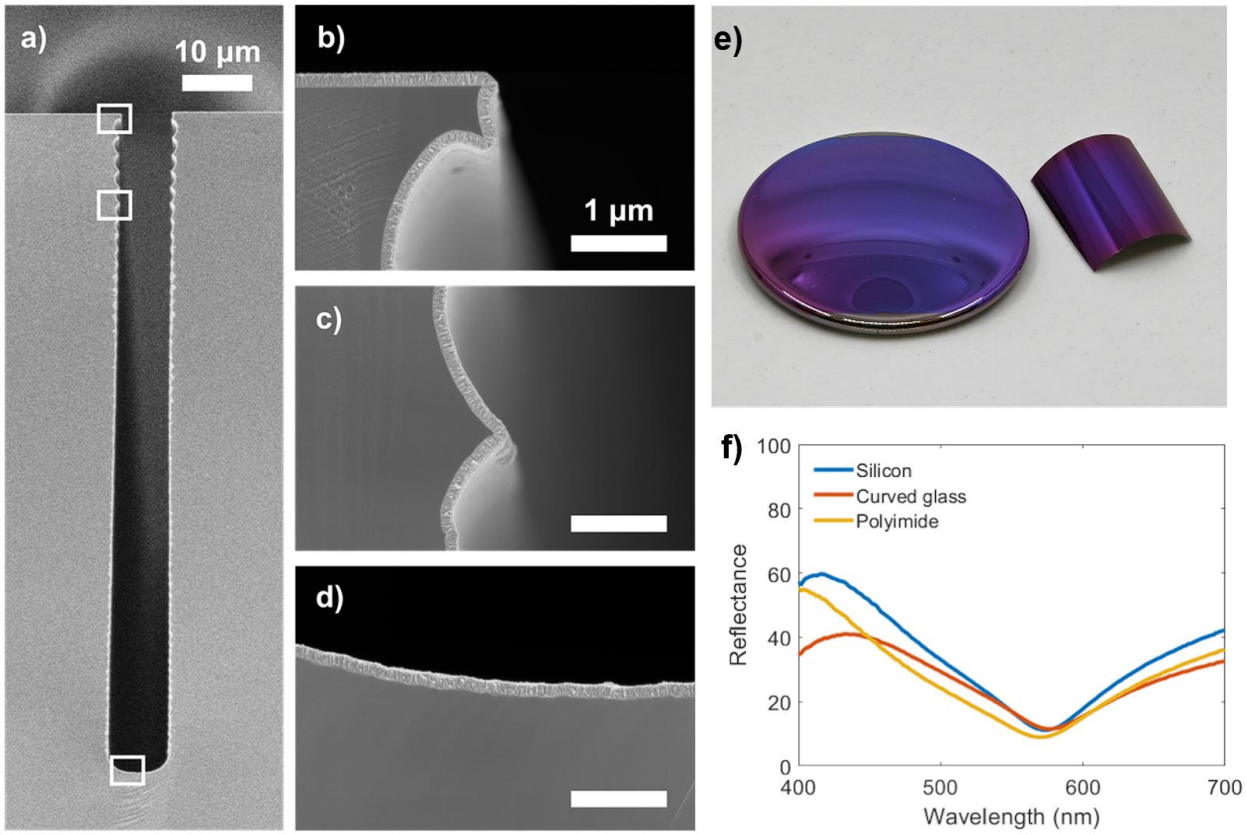


Figure 25. Conformal ALD coatings including a-d) SEM images of trench coatings and e-f) MDM coatings on curved glass and polyimide.

4.4 Techniques for Patterning Structural Colors with AS-ALD

4.4.1 Patterning with Polymer Inhibitors in AS-ALD

In addition to achieving full substrate coverage, ALD offers the unique capability to selectively deposit structural colors in predetermined patterns. To demonstrate this, a polymer inhibitor layer was used to create patterned structural colors with AS-ALD, as illustrated in Figure 26. Previous studies have shown that polymers with surface functional groups that inhibit ligand-exchange reactions with ALD precursors can effectively suppress nucleation and growth.[121,123,142–146] This method provides a novel approach to integrate structural colors with additively manufactured materials: polymer inhibitors can be 3D-printed onto specific regions of a substrate,

locally preventing ALD growth. By selectively depositing ZnO films in unmasked areas, the thickness, and therefore the color, of the films can be tuned to create intricate, multicolor patterns on a single substrate.

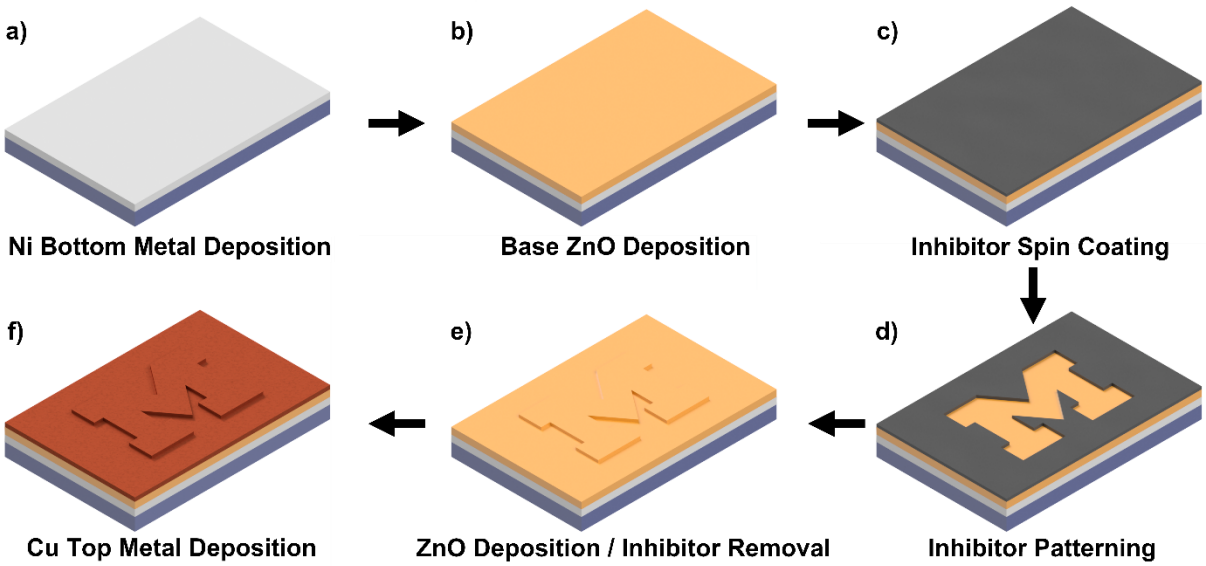


Figure 26. a-f) Process Flow for Patterning Block “M” structure with Area-Selective Atomic Layer Deposition.

To demonstrate the feasibility of this approach, the letter ‘M’ was patterned to produce a yellow core surrounded by a blue background. This process began with the deposition of a Ni metal layer on a Si substrate, followed by the deposition of 90 nm of ZnO to create the blue background color. Next, SPR 955 photoresist was spin-coated onto the ZnO layer and patterned using photolithography to locally expose the “M" area by removing the polymer inhibitor. An additional 30 nm of ZnO was then deposited onto the exposed area to generate the yellow core. Finally, the polymer inhibitor was removed with organic solvents, and the entire sample was coated with a 20 nm Cu layer using ALD.

The resulting pattern exhibited vibrant yellow and blue regions, as shown by the optical microscopy image in Figure 27b. X-ray photoelectron spectroscopy (XPS) analysis of the inhibited area (Figure 27d) confirmed that the ZnO deposition was completely inhibited, as no Zn 2p peaks were observed in the core scan. In contrast, the unmasked areas showed Zn 2p core spectra with the expected stoichiometry for ZnO growth.

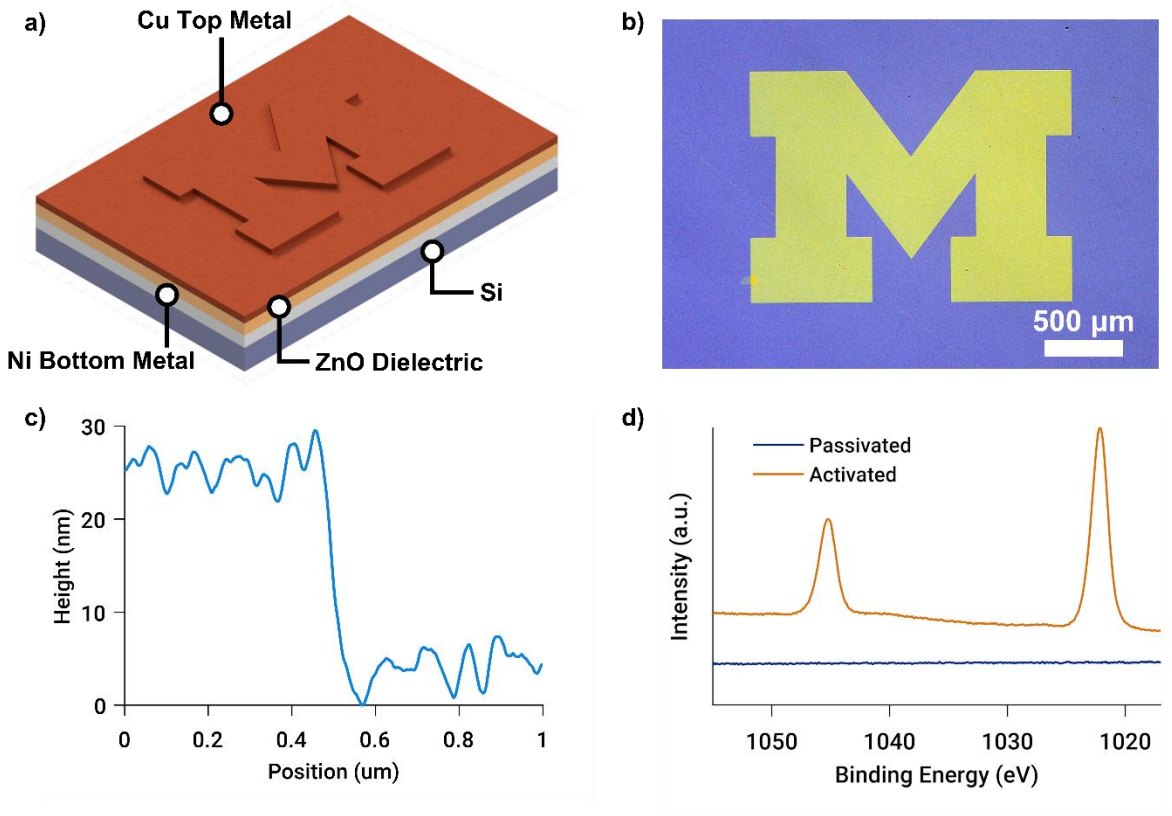


Figure 27. Patterned structural color coating with AS-ALD including a a) schematic and b) optical microscope image. c) AFM step analysis and d) XPS Zn characterization confirm difference in composition between masked and unmasked areas.

To analyze the morphology of the patterned films, atomic force microscopy (AFM) was performed across the boundary between the yellow ‘M’ and the blue background, as shown in Figure 27c. A distinct step edge was observed, with the step height matching the expected ZnO thickness based on ellipsometry measurements. Furthermore, the reflectance colors of the

patterned regions were consistent with the predicted values: the dielectric thicknesses of the blue and yellow regions were approximately 90 nm and 120 nm, respectively.

It is important to note that this is not a traditional lift-off method, which typically leaves sidewalls along pattern boundaries. Instead, by selecting a polymer that inhibits ALD growth, this is a fully additive process where the ALD film is deposited only in the unmasked regions, resulting in a clean step-edge without sidewall residue. This demonstration shows the potential of AS-ALD for patterning structural colors. The following section explores the application of this technique in an additive 3-D printing process.

4.4.2 Patterning Polymer Inhibitors with E-jet Printing

Although the pattern in section 4.4.1 was created using photolithography, the use of printed polymers to pattern structural colors is a versatile method that enables the integration of area-selective structural colors with 3D printing techniques. In particular, previous work has shown that electrohydrodynamic jet (e-jet) printing can be combined with AS-ALD to selectively deposit functional materials with sub-micrometer linewidths – significantly below the resolution of ink-jet printing – while maintaining the sub-nanometer precision of ALD in the vertical (z) direction.[132–134,147] Here, this approach is extended to demonstrate additive nanomanufacturing of structural colors.

To showcase the use of e-jet printing in structural-color patterning, polyvinylpyrrolidone (PVP) inks (5 wt% PVP in DMSO) were printed onto Si substrates to selectively modify ZnO thicknesses with AS-ALD, as shown in Figure 28. Before e-jet printing, a blanket ZnO film was deposited using ALD to create the desired font color, based on the palette shown in Figure 28b. To alter the background color, a PVP inhibitor layer was e-jet printed onto this blanket film, preserving the ZnO thickness underneath the printed regions. Additional ALD ZnO cycles were

then performed, selectively modifying the thickness – and thus the color – of the unprinted background regions, as shown in Figure 28. The font color was determined by the initial ZnO blanket film thickness, while the background color was tuned by adjusting the thickness of the subsequent ZnO deposition. This process successfully produced red, blue, and yellow text with sub-10 μm resolution in linewidth, as shown in Figure 28. The images highlight the successful patterning of ZnO, demonstrating precise control over both font and background colors.

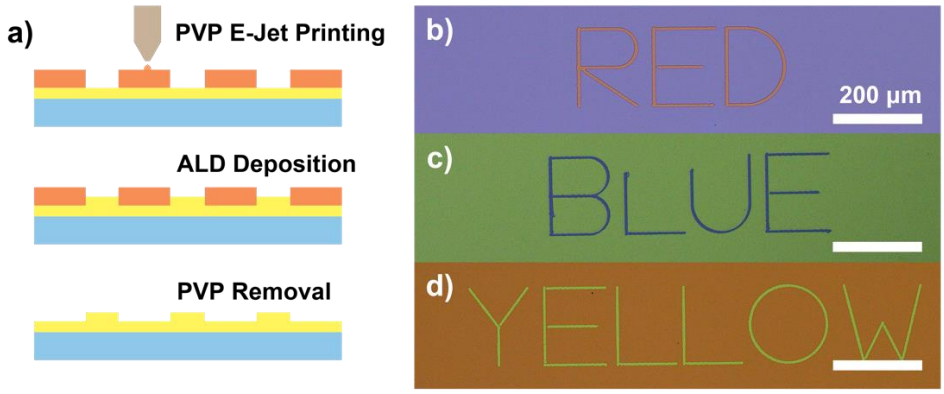


Figure 28. Structural color patterning with e-jet printing and AS-ALD, including a a) schematic process flow and b-d) optical microscope images.

E-jet printing experiments were conducted using a custom-built setup at the University of Michigan, integrated with a Nanosurf Nanite atomic force microscope (AFM). The setup included an X-Y-Z nanopositioning stage, a voltage amplifier, a function generator, a camera and light source for nozzle alignment and jetting visualization, and a nozzle mount to hold micropipette nozzles. The ink consisted of 5 w% PVP in DMSO, filtered through a 0.22 µm pore size filter to prevent nozzle clogging. Micropipette nozzles with a 2 µm opening (provided by World Precision Instruments) were used, with a 20 µm offset from the substrate. Pulse printing was employed to create the patterns, using a high voltage of 370 V, a low voltage of 255V, and a pulse duration of 90 µs. The printing process operated at a frequency of 100 Hz and a stage speed of 1mm/s.

4.5 Characterization and Evaluation of ALD-Coatings

4.5.1 Optical and Structural Characterization of AS-ALD Coatings

The optical and structural properties of the ALD coatings were characterized to assess their quality and suitability for structural color applications. These measurements provide crucial insights into the film's thickness, composition, surface morphology, and optical behavior.

Spectroscopic ellipsometry was conducted using a J. A. Woollam M-2000 ellipsometer with a Cauchy model, covering a wavelength range of 400-1600 nm and utilizing three angles of incidence (65°, 70°, and 75°) to determine the thickness and refractive indices of the ALD films. Refractive indices were then used in TMM simulations included in Figure 23. X-ray Photoelectron Spectroscopy (XPS) was performed with a Kratos Axis Ultra XPS system, using a monochromatic Al source (10 mA, 12 kV) with a pass energy of 20 eV and a step size of 0.1 eV on a spot size of 700 µm by 300 µm. The XPS spectra were analyzed with the CasaXPS software to evaluate the elemental composition and chemical state of the coatings.

Scanning Electron Microscopy (SEM) images were obtained with an FEI Helios 650 Nanolab SEM at 2 kV and 100 pA to observe the surface structure and morphology, as seen in Figures 19 and 22. Atomic Force Microscopy (AFM) was performed using a MFP-3D Origin+ AFM from Asylum Research to assess the surface roughness and topography, as seen in Figure 27. Reflectance spectra at normal incidence were measured using a thin-film measurement spectrometer (Ocean Optics Inc. HR4000CG-UV-NIR High-Resolution Spectrometer) integrated with a white light source to evaluate the optical performance of the coatings, as seen in Figures 20 and 22.

These characterizations establish a baseline for understanding the structural and optical properties of the ALD coatings. The following section focuses on assessing the durability of the color of these films, which is critical for their use in long-term applications.

4.5.2 Assessing Color Durability in Conformal Coatings

One significant advantage of structural color coatings over traditional organic-based paints is their enhanced thermal stability, resulting from the use of entirely inorganic materials. While the materials in this study may not outperform the most thermally stable pigment-based paints, dielectric materials like Al_2O_3 remain stable at temperatures up to 800 °C.[148] Additionally, with appropriate material selection, these coating can act as protective barriers against thermochemical reactions, such as oxidation in humid environments. However, the MDM structure in this study has a Cu top layer, which is particularly prone to oxidation in ambient air, especially at elevated temperatures. To address this limitation and improve the thermal stability of the structural color, an Al_2O_3 overcoat layer was added as a protective barrier for the Cu layer, forming a DMDM structure.

Beyond its protective properties, the Al_2O_3 overcoat introduces an optical effect that enhances color saturation. When the Al_2O_3 thickness is designed to be one-quarter of the reflection valley wavelength, it acts as an anti-reflection layer that couples with the resonant wavelength of the cavity. Anti-reflection coatings optimize light absorption at the desired wavelength while minimizing absorption at the reflection peak wavelength, resulting in more vibrant and saturated colors.[68,149] For example, an SiO_2 anti-reflection coating was used in section 3.3.2 to maximize absorption across the visible wavelengths, resulting in a black coating. To demonstrate this effect with conformal ALD coatings, the colored wolverine figurines in Figure 24 were coated with

corresponding Al_2O_3 thickness: the blue figurine was coated with 91 nm, and the yellow figurine with 65 nm of Al_2O_3.

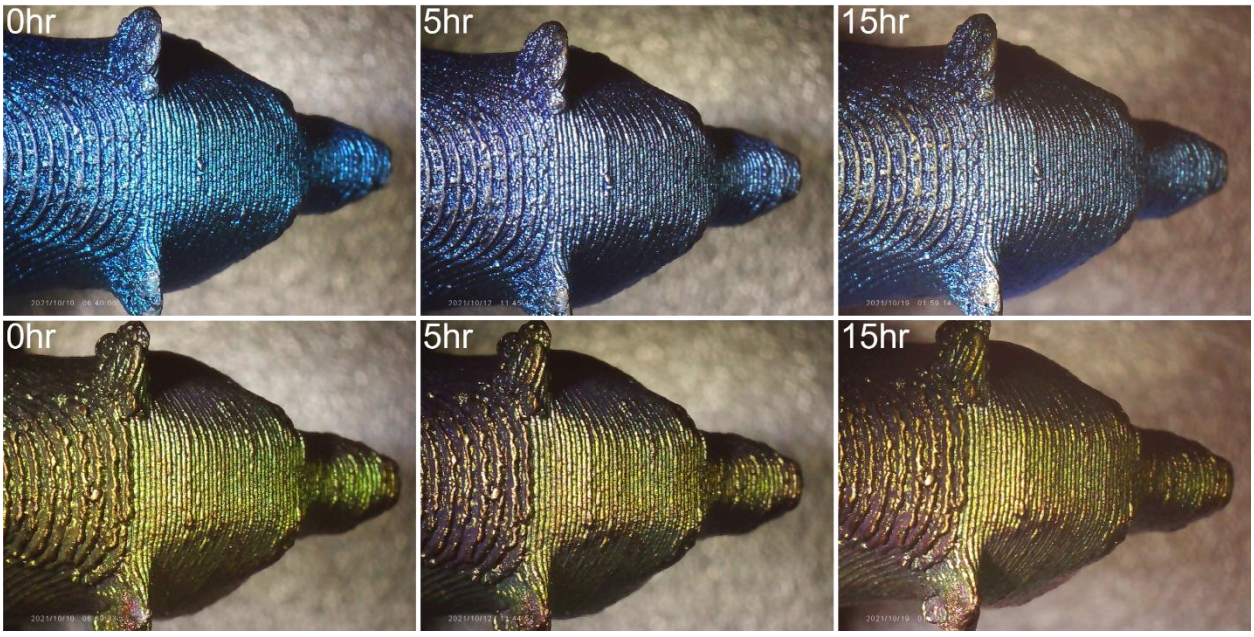


Figure 29. Thermal stability of blue and yellow wolverine figurines in ambient air at 300 °C. Both figurines were coated with a protective anti-reflective Al_2O_3 layer.

To evaluate the thermal stability of the DMDM structures, the coated wolverine figurines were baked at 300 °C in ambient air for 5-hour intervals, for a total duration of 15 hours. Optical microscopy images in Figure 29 show the surface colors of the figurines as-deposited, after 5 hours of thermal treatment, and after 15 hours thermal treatment. Both figurines retained their bright, vibrant colors without any evidence of peeling or delamination, even after 15 hours of exposure to high temperatures.

Further testing was conducted using planar stainless steel substrates coated with analogous MDM and DMDM structures, and their reflectance spectra were measured under high-temperature conditions, as shown in Figure 30. The results show a clear distinction: MDM structures without an Al_2O_3 overcoat exhibited spectral changes and surface degradation due to oxidation, while the

DMDM structures with an Al_2O_3 layer retained their optical properties and showed subtle signs of oxidation. These results demonstrate the ability of DMDM structures to maintain vivid structural colors under conditions that are incompatible with most organic paints.

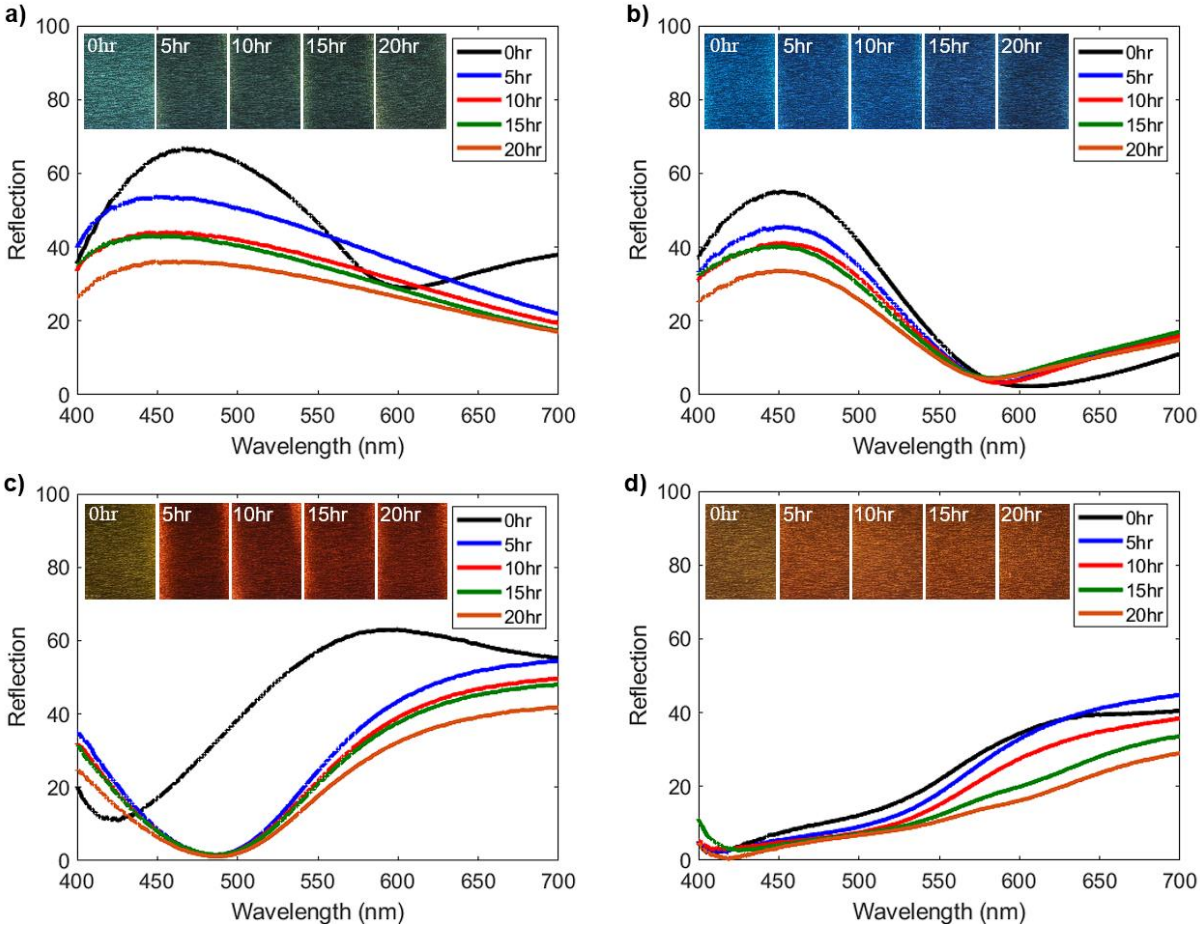


Figure 30. Measured reflectance spectra for planar a-b) MDM and c-d) DMDM structures during 300 °C baking, demonstrating a higher DMDM endurance.

4.6 Brief Overview of SALD and Its Potential for High-Throughput Coating

4.6.1 Introduction to Spatial ALD (SALD) for High-Throughput Coating

Spatial ALD (SALD) is an emerging technique designed to achieve high-throughput thin-film deposition over large areas.[131,150] Unlike conventional ALD, which relies on sequential exposure of the substrate to precursors within a vacuum chamber, SALD continuously exposes the substrate to spatially separated precursors, enabling film growth at atmospheric pressure. This setup significantly reduces deposition time while maintaining the precise thickness and conformality characteristic of ALD. These features make SALD highly attractive for industrial-scale applications, where the ability to efficiently coat large substrates is critical.

SALD also complements AS-ALD by enabling the uniform deposition of coatings over large areas, which can then be selectively patterned using AS-ALD techniques. This combination creates opportunities for the scalable production of functional coatings with both uniform and patterned regions, ideal for applications such as displays, sensors, and decorative surfaces.

4.6.2 High-Throughput Characterization of Film Thickness

One innovative aspect of SALD is the ability to utilize the structural colors of deposited films as a rapid and non-invasive method to characterize film thickness and uniformity. By selecting thickness ranges that produce distinct color variations, the deposited film's color can serve as a visual indicator of thickness variations. A charge-coupled device (CCD) camera can be used to record the film during or after deposition, capturing the color of each pixel of the substrate. The observed RGB values from the CCD camera are then compared to a pre-calculated reference of simulated RGB values for a range of thicknesses, enabling precise thickness determination at each pixel.

This approach allows for real-time or post-deposition analysis of film thickness and uniformity over large areas. Regions with inconsistent thicknesses can be easily identified based on color deviations, reducing the need for more time-intensive techniques like spectroscopic ellipsometry. The ability to rapidly characterize films makes SALD particularly appealing for industrial applications where large-scale production and quality control are paramount.

Chapter 5 Printing Thin Film Transistors with Shock-wave Jet Printing

5.1 Introduction to Carbon Nanotubes (CNTs) in Electronics

5.1.1 Overview of Printed Electronics

Over the last decade, advancements in printed electronics have transformed traditional rigid electronic components into flexible, bendable, stretchable, and lightweight printable forms capable of conforming to or wrapping around objects.[151–155] These innovations have fueled the growing adoption of printed electronics and their integration with conventional electronics, resulting in flexible hybrid electronic (FHE) systems. FHE systems are crucial for the development of emerging technologies such as the internet-of-things (IoT) and wearable devices.[156] Printed electronics have enabled applications that are unattainable with rigid components, including wearable computing, flexible optoelectronics, personal health monitoring systems, environmental monitoring, RFID, sensors, smartwatches, electronic tattoos, and energy harvesters.[157–169]

This technological progress is driven by several factors. First, printed electronics are highly cost-effective due to their additive manufacturing process, which operates at low temperatures and does not require vacuum systems.[167] Second, they are compatible with a wide range of substrates, enabling the development of flexible and large-area hybrid electronic systems.[168] Finally, printed electronic sensors have demonstrated functionality across diverse applications, including pressure, biosensing, temperature sensing, and more.[169–174] One of the most compelling aspects of printed electronics is their ability to produce sensors and systems that meet the high-throughput and low-cost manufacturing demands of IoT technologies.

Carbon nanotubes (CNTs), with their unique electronic, thermal, and mechanical properties, have emerged as an exceptional material for flexible and wearable electronics. CNTs enable the creation of advanced sensors, transistors, and other electronic components suitable for diverse applications. As demand grows for scalable and high-resolution printing methods, CNTs continue to play a pivotal role in pushing the boundaries of printed electronics, meeting the needs of emerging technologies in IoT and wearable systems.

This chapter is adapted from Seva, Rorem et al., "Nozzle-Free Printing of CNT Electronics Using Laser-Generated Focused Ultrasound", Small Methods, **8** (10), pg. 2301596, 2024. Sarah Seva and I contributed equally to this work, which was done in collaboration with Karthik Chinnathambi, David Estrada, L. Jay Guo, and Harish Subbaraman.

5.1.2 Challenges in Traditional CNT Printing Methods

Inkjet printing and aerosol jet printing are widely used for a range of applications due to their unique capabilities.[156,172,174,175] However, both techniques are limited by nozzle clogging, which is a common issue.[176] Nozzle clogging can occur for several reasons, including agglomeration and sedimentation caused by van der Waals forces, the large lateral dimension of the nanomaterials (especially the elongated structures of 1D nanomaterials), and solvent evaporation at the nozzle.[159–161,163,177] To address these challenges, researchers have explored various methods, such as dispersing nanomaterials through sidewall functionalization or using organic solvents.[178] However, these methods often introduce new issues. For example, sidewall functionalization can shorten 1D materials and damage tube walls, which reduces the electrical performance of printed materials.[162,176]

Drop-on-demand (DoD) piezoelectric inkjet printing (IJP) is a widely used technology in microelectronics research. It enables precise pattern formation by ejecting small fluid droplets

directed to specific locations using computer-aided design (CAD) patterns.[179] This process relies on a piezoelectric actuator, which generates a pressure wave to displace ink through the nozzle, forming droplets with high accuracy.[180–183] While IJP is simple and effective for printing nanomaterials, it presents several challenges. To prevent nozzle clogging and ensure dispersion, the ink must have low surface tension, low viscosity, and a uniform incorporation of nanomaterials. CNTs, in particular, tend to agglomerate and sediment due to strong van der Waals forces, exacerbating the risk of nozzle clogging.[179–187]

Efforts to improve CNT dispersion have included surface functionalization for organic solvents and the use of dispersants in water-based ink. While functionalization improves dispersion, it can negatively affect CNT conductivity.[187] Organic solvents offer an alternative by adsorbing onto the CNT surface through hydrophobic interactions, mitigating van der Waals forces.[187] However, these solvents limit CNT concentration to approximately 0.1 mg/mL and pose challenges due to their volatility, which can lead to ink evaporation and further clogging.[188] As a result, ink concentration must be limited, requiring an increase in the number of print passes.[186] Additionally, sonication is often required to separate CNTs and avoid agglomeration. However, sonication can introduce defects into the CNTs, further compromising the performance of printed thin-film transistors (TFTs).

Nozzle clogging remains a significant limitation in inkjet printing, particularly for 1D nanomaterials with longer dimensions. Strict conditions, such as low precipitation and small particle sizes, are required in ink formulation to address these issues. For instance, the nozzle diameter in Dimatix inkjet printers is 21.5 μm, with a rule of thumb suggesting that only particles smaller $1/50^{th}$ of the nozzle diameter (approximately 0.43 μm) can be reliably printed.[189,190] This limitation poses challenges for printing semiconducting single-walled carbon nanotubes (S-

SWCNTs) with lengths ranging from 300 nm to 5 μm, as shown by the histogram in Figure 31. With a maximum printable length of 430 nm, it is estimated that more than 75% of the CNTs are broken during the IJP process. This size restriction, combined with limited ink concentration due to nozzle clogging, underscores the need for alternative printing methods to overcome these challenges.

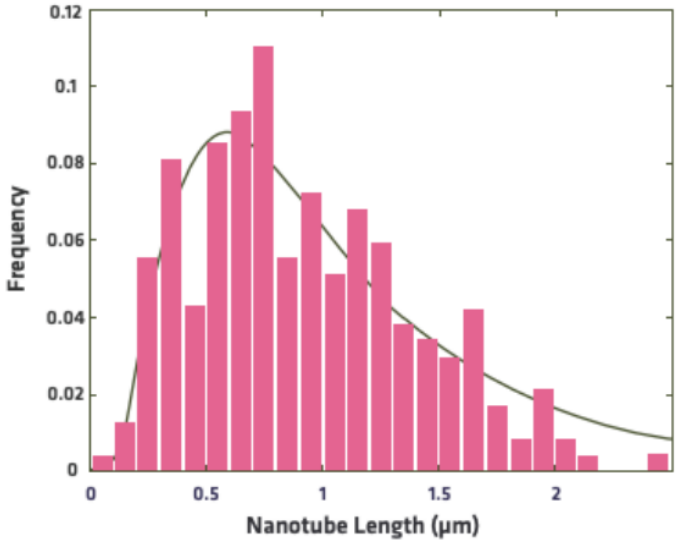


Figure 31. Histogram of CNT length in purchased CNT ink, provided by NanoIntegris Inc.

5.2 Fundamentals of Shock-wave Jet Printing (SJP) for CNTs

5.2.1 Principles of SJP

While promising demonstrations of nozzle-free jetting schemes have been reported, [191,192] practical applications are challenging for multiple reasons.[193–196] Such challenges include slow speed, uncontrolled high-speed jets, and laser-induced spherical bubble-based jetting which requires optically transparent liquid and thermally stable materials to avoid high-temperature annealing-induced material property changes.[194,196,197] Shock-wave Jet Printing (SJP) is a novel, nozzle free printing technology that addresses many challenges in traditional materials printing

techniques.[191,192] Unlike conventional methods, SJP achieves high-speed liquid microjetting through a nonthermal process that eliminates the need for nozzles, reducing issues such as clogging and restrictions on ink viscosity. This technology uses focused acoustic pulses, less than 100 ns in duration, generated by a pulsed Nd:YAG laser beam and geometrically focused with a photoacoustic (PA) lens, as shown in Figure 32d.[198] These acoustic waves create a high-pressure jet that ejects ink or material from a liquid interface onto a substrate with exceptional precision.

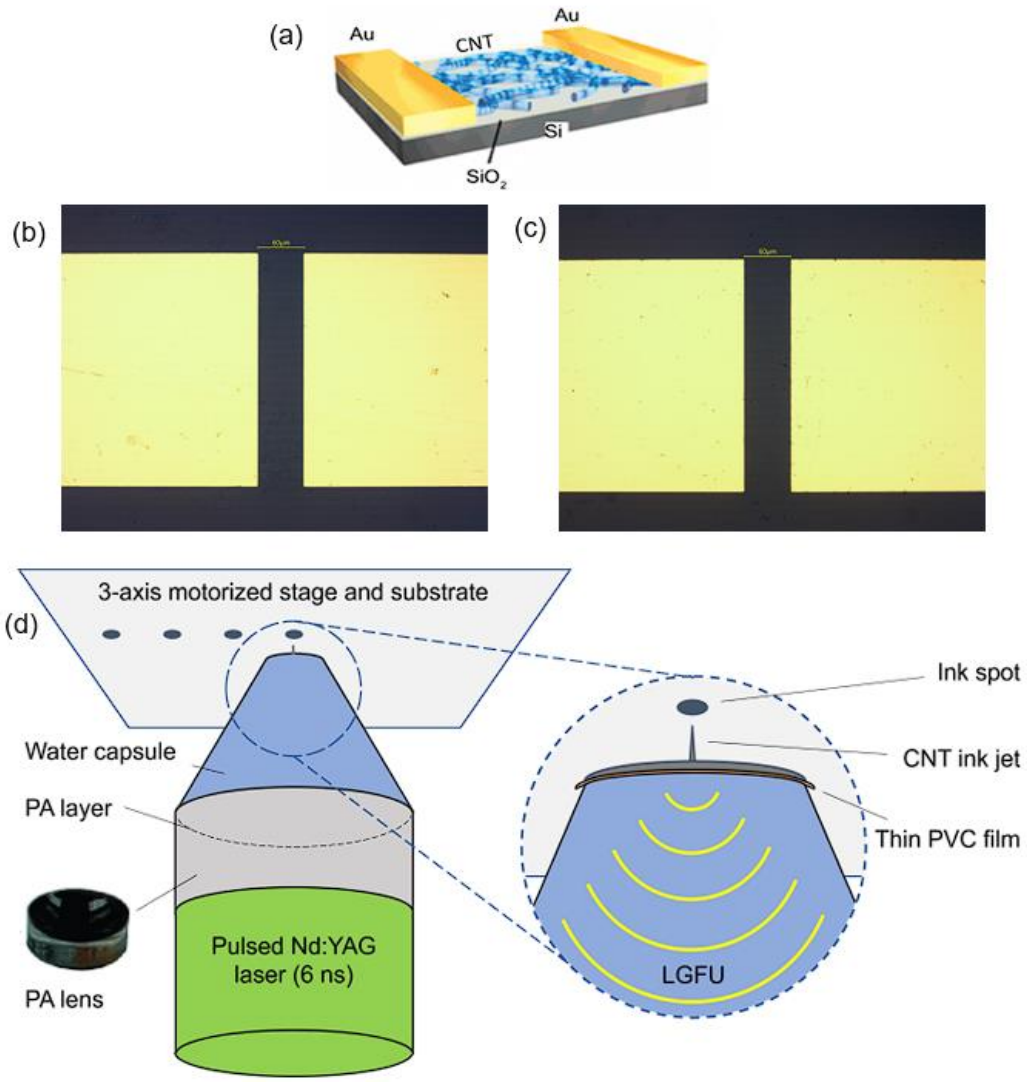


Figure 32. SJP printing setup including a) CNT transistor schematic, optical microscope images of b) IJP and c) SJP devices, and d) SJP schematic.

SJP demonstrates the capability to eject liquids and solid particles up to 100 μm in size, making it suitable for diverse printing applications. While inkjet printing (IJP) and aerosol jet printing (AJP) can achieve resolutions of a few microns and 16 μm, respectively, these methods often require optimized ink formulations and encounter clogging issues.[199,200] SJP's nozzle-free approach overcomes these limitations, providing a robust alternative for high-resolution printing, as shown in Figure 32a-c. The experimental setup and device fabrication details, including photolithographic patterning and post-printing processing, are further described in Appendix B and section 5.3.

5.2.2 Advantages of SJP for CNTs

SJP offers significant advantages for printing carbon nanotubes (CNTs), particularly when compared to traditional nozzle-based techniques. Its nozzle-free design eliminates clogging, a common issue in inkjet and aerosol jet printing caused by nanomaterial agglomeration, sedimentation, or high ink concentrations. By removing the need for nozzles, SJP accommodates inks with a wide range of viscosities and particle sizes, enabling the use of CNT-based inks without the strict formulation requirements of traditional printing methods.

Another key advantage of SJP is its ability to achieve high-resolution patterning with fewer passes, reducing ink usage and improving efficiency. The high-speed liquid microjets generated by SJP allow precise deposition of CNT lines with minimal spreading, even for water-based inks. This precision ensures that CNT patterns maintain their structural integrity, which is critical for applications such as back-gated transistors. In contrast, inkjet printing requires low-viscosity inks and multiple passes to achieve similar results, often at the expense of material conductivity due to defects introduced during ink preparation.

SJP's ability to print larger particles and higher-viscosity inks enhances its versatility for CNT printing, making it particularly suitable for advanced electronic applications. By utilizing its nonthermal process, SJP avoids high-temperature annealing that could damage sensitive materials, further supporting its use with CNT-based inks. SJP expands the capabilities of additive manufacturing by enabling precise, high-resolution deposition of CNTs without the limitations of nozzle-based techniques, making it a scalable approach for advanced electronics. These features position SJP as a promising tool for high-performance, efficient, and reliable CNT printing in emerging electronic devices.

5.3 SJP Setup and Process Parameters

5.3.1 Overview of the SJP Mechanism and Equipment

The SJP mechanism relies on laser-generated focused ultrasound (LGFU) to create high-speed microjets. This process induces cavitation in water by generating a high negative pressure amplitude (>20 MPa), exceeding the homogeneous nucleation threshold of water. The jet height and resolution are controlled by the intensity of the pressure wave and the alignment of the acoustic focal point relative to the ink surface. The system, illustrated in Figure 32d, uses a photoacoustic (PA) lens coated with a carbon black composite embedded in polydimethylsiloxane (PDMS), which efficiently converts light into focused sound energy. The acoustic waves transmit through a water capsule to the ink interface, with a thin PVC film separating the water and ink to prevent mixing.

A receiving substrate is placed in the jet's path using a 3D translation stage, which enables precise placement of the deposited droplets. The substrate is heated to accelerate solvent evaporation from the printed ink. This setup achieves a resolution of 20-30 μm for water-based inks on glass substrates.[191] Jets and deposited droplets are observed with a shadowgraph system,

where synchronized light pulses illuminate the ink surface, delayed by 220 μs relative to the Nd:YAG pulse to account for propagation delays. Additional experimental details are provided in Appendix B.

5.3.2 Process Parameters and Optimization

The SJP system's performance is highly dependent on optimizing process parameters. Laser energy was set at 150 mJ per pulse and attenuated with an ND 0.2 filter to protect the PA layer from damage. Further attenuation reduced jet strength, while a frequency of 20 Hz was found to be optimal for creating continuous patterns at a translation speed of 50 μm/sec. The ink used was NanoIntegris CNT ink with a concentration of 0.01 mg/m, placed atop the PVD film in the water capsule. The ink height was carefully adjusted to approximately 10 μm above the ultrasound focal point to ensure consistent jetting behavior.

A key challenge with this system is managing ink evaporation, which directly affects the ink height and, consequently, jetting performance. The system is sensitive to ink height variations within about 100 μm. As evaporation caused the ink level to drop, the substrate was periodically lowered to maintain a working distance near 250 microns. When jetting performance declined, the ink height was replenished. Using this approach, consistent jets measuring 20 x 500 μm were produced at 20 Hz, depositing droplets onto the substrate with high precision. Further experimental setup details and device fabrication processes are available in Appendix B.

5.4 Printing CNT Transistors with SJP

5.4.1 Design and Fabrication of CNT Transistor Structures

CNT thin-film transistors (TFTs) were fabricated using a combination of photolithography, PVD, and CNT printing. P-type silicon wafers with a 90 nm SiO_2 layer were patterned using

photolithography, as detailed in Appendix B. A 10 nm titanium adhesion layer and a gold contact layer were deposited onto the patterned photoresist, after which the photoresist was removed through a lift-off process. The samples were then cleaned and treated with oxygen plasma and poly-L-Lysine to improve CNT adhesion.

During the CNT printing process, the sample was inverted and mounted on a 3D-translation stage. A heating pad was applied to the backside of the sample to encourage solvent evaporation. After aligning one of the source-drains with the center of the jet, the sample was lowered to approximately 250 μm above the ink height. The Nd:YAG laser was activated, ejecting ink droplets across the source-drain area. To ensure uniform coverage of the channel, a spiral printing pattern was used to fill the target area. Upon completion, the sample was raised to visually confirm alignment. If necessary, the ink was replenished, and the sample was either lowered for additional printing passes or translated to the next device.

After printing, the samples were dipped in hot DI water for 10 seconds to remove surfactants, which can interfere with the CNT network and degrade device performance. Finally, the samples were annealed, completing the fabrication process and preparing the devices for electrical characterization.

5.4.2 Morphological Comparison of IJP and SJP Devices

Figures 30a and 30b show scanning electron microscopy (SEM) images CNT channel devices printed using IJP and SJP, respectively. Both images highlight the uniform coverage of random CNT networks within the channel areas. Although the same CNT ink was used for both methods, the resulting films exhibit clear differences.

The IJP-printed device demonstrates uniform CNT coverage across the channel but requires 10 printing passes to produce functional transistors for channel dimensions of 2 – 300 μm

in length and 300 μm in width. In contrast, the SJP-printed device achieves functional transistors with only a single printing pass for the same channel dimensions, although the CNTs are more sparsely distributed. The shorter CNT lengths in IJP-printed films (consistent with earlier estimates based on nozzle size limitations) necessitate additional printing passes to form fully connected percolating paths between the source and drain electrodes. This results in a much denser CNT network and higher CNT ink consumption compared to SJP.

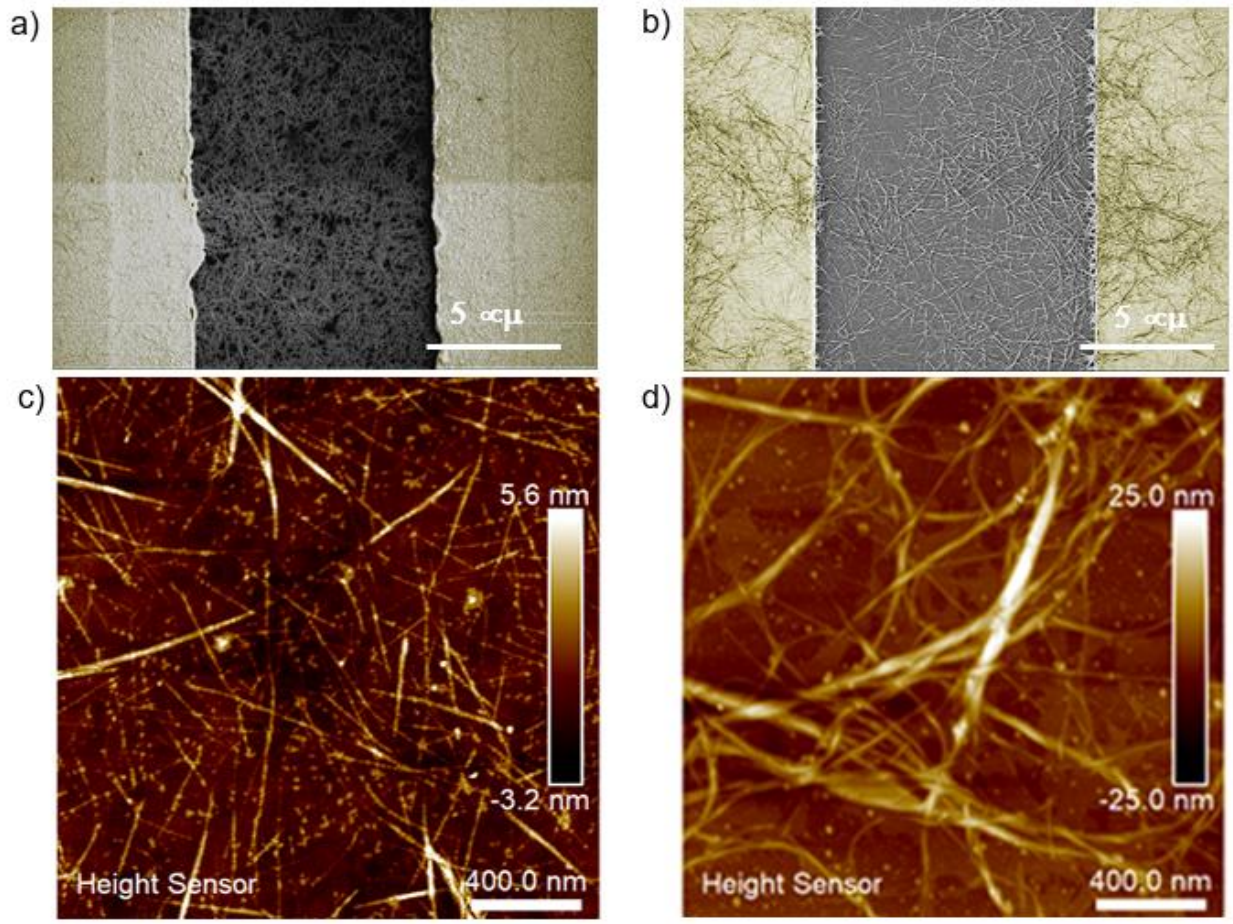


Figure 33. a-b) SEM and c-d) AFM images of IJP-printed (left) and SJP-printed (right) CNT TFTs.

In the IJP-printed devices, the dense CNT network is not clearly visible on the metal contacts, likely due to the smaller tube lengths. Conversely, SJP-printed devices feature significantly longer CNTs, as evident in Figure 33b. These longer CNTs span larger distances between the gold electrodes, enabling sufficient percolating conduction paths with just one printing pass.

Atomic force microscopy (AFM) images of CNT channels, shown in Figures 30c and 30d for IJP and SJP, respectively, further illustrate these differences. The denser CNT network in IJP-printed devices results in a surface roughness of 1.44 nm, whereas SJP-printed devices exhibit a higher surface roughness of 2.8 nm due to larger CNTs. Both SEM and AFM analyses confirm that SJP devices have a sparser CNT distribution compared to IJP devices.

5.4.3 Electrical Comparison of IJP and SJP Devices

The I-V measurements in Figure 35 highlight the effectiveness of the SJP printing. For IJP-printed devices, no semiconducting channel was formed between the source and drain electrodes with one or five printing passes, except for the 2 µm channel-length device printed with five passes. This limitation arises because CNTs are shortened to match the size of the nozzle during IJP. For this reason, IJP devices were printed with 10 passes. In contrast, SJP printing produced functional transistors across the entire range of channel lengths, from 2 to 300 µm, with just one printing pass.

The transistor transfer characteristics, represented as drain current (I_d) vs gate voltage (V_g), were measured for the fabricated CNT-TFTs. A gate voltage sweep from -20 to 20 V was applied to the heavily doped silicon substrate (serving as the global back gate), while a drain bias (V_d) of 1 V was maintained. Mobility (µ) was extracted using the equation:

$$\mu = \frac{g_m L}{W C_{ox} V_d}$$

Eqn. 5-1

where g_m is the peak transconductance (dI_d/dV_g) obtained from the forward sweep of the transfer curve, L is the channel length, W is the channel width, and C_{ox} is the oxide capacitance per unit area (ε_{ox}/t_{ox}). It is important to note that mobility calculations using parallel plate capacitance underestimate μ, especially for low-density CNT networks, as some areas of the channel remain uncovered by CNTs. Furthermore, forward sweep measurements tend to overestimate mobility due to hysteresis in transfer characteristics, which is attributed to charge trapping by hydroxyl groups adsorbing on the SiO_2 surface or charge injection into the substrate.[201] Despite these limitations, the parallel plate capacitance model and forward sweep measurements provide a convenient way to compare results with existing literature.[202,203] While direct measurement of gate capacitance offers more accurate mobility estimations, it introduces additional complexities.[204–206]

CNT networks rely on percolating paths to enable charge carriers to travel between electrodes. In these devices, the gold electrode's work function aligns with the CNT valence band, promoting the injection of holes during operation. CNTs have a delocalized π-electron system with a high density of states near the valence band, providing many states and pathways for efficient hole transport. The intrinsic carrier mobility, μ_i, for a single CNT can be calculated using *Eqn. 5-1* and achieve device mobilities exceeding 100,000 cm²/V·s.[207,208]

When multiple CNTs are connected in series, the effective mobility decreases due to scattering and contact resistance at the junctions. This relationship is described by the equation:

$$\mu_{eff} \propto \frac{1}{R_{Total}}$$

$$R_{junction} = R_0 e^{\eta\theta}$$

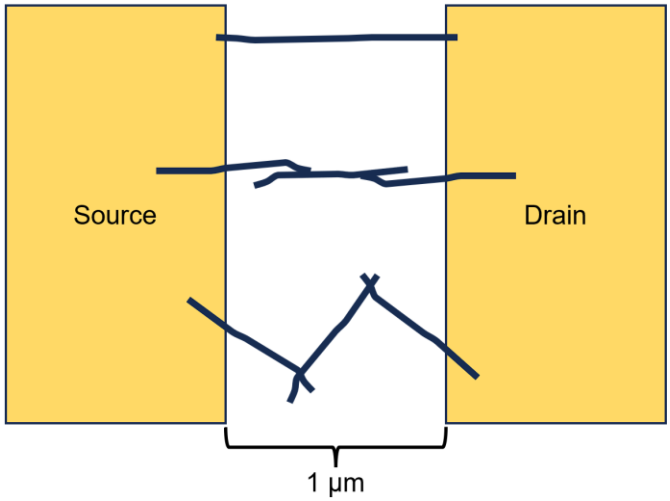
$$R_{Total} = NR_{CNT} + (N-1)R_{junction}$$

$$\mu_{eff} = \frac{\mu_i}{N + (N-1)\frac{R_{junction}}{R_{CNT}}}$$

Eqn. 5-2

where μ_{eff} is the effective mobility, $R_{junction}$ is the junction resistance, η is the scattering coefficient of the CNT junctions, θ is the angle between the CNTs, R_0 is the resistance at $\theta = 0$, R_{CNT} is the intrinsic resistance of the CNT, and N is the number of CNTs in the percolating path. R_{CNT} scales with the length of the CNTs. The angular scattering term, $e^{\eta\theta}$, was based on percolating path models in 1D materials like CNTs.[209,210] Charge transport relies on wavefunction overlap at CNT junctions, represented by the exponential term. In this case, 180° junctions will yield the largest resistance term.

Some simplified cases, illustrated in Figure 34.1 using *Eqn. 5-2* and standard values for the scattering coefficient, contact resistance at $\theta = 0$, and intrinsic resistance, demonstrate the significant impact of junctions on mobility. As shown in Table 2, the effective mobility decreases by orders of magnitude as the number of junctions and scattering sites increases. Based on these values, the CNT networks in this study likely have ~10 junctions. These findings highlight that networks with fewer junctions and shorter percolating paths achieve higher measured mobility.



$$R_0 = \sim 10^6\ \Omega$$
$$R_{CNT,\,1\mu m} = \sim 10^5\ \Omega$$
$$\eta = 0.5\ rad^{-1}$$
$$\mu_{eff} = \frac{\mu_i}{N + (N-1)\frac{R_0 e^{\eta\theta}}{R_{CNT}}}$$

Figure 34. A schematic of simple CNT networks and effective mobility parameters.

Table 2. Calculated hole mobility values (cm^2/V.s) using *Eqn. 5-2* for different percolating paths.

# of CNTs	μ (0° junctions)	μ (90° junctions)	μ (180° junctions)
1	100000 (control)	-	-
2	8300	4200	2000
3	4300	2100	1000
5	2200	1100	500
10	1,000	500	200

To compare the electrical performance of IJP and SJP printed CNT-TFTs, transfer characteristics and I_d-V_d family plots were analyzed. Figure 35a presents representative transfer characteristics for IJP and SJP devices with a channel length of 60 μm and width of 300 μm. Both devices show good gate modulation, with noticeable hysteresis attributed to charge trapping. However, IJP devices exhibit approximately twice the current of SJP-printed devices, as shown in Figure 35c and 35d, respectively, a result of the denser CNT network created by the multiple printing passes in IJP. Furthermore, the I_d-V_d plots reveal that drain current saturation occurs at a lower V_d for IJP devices compared to SJP.

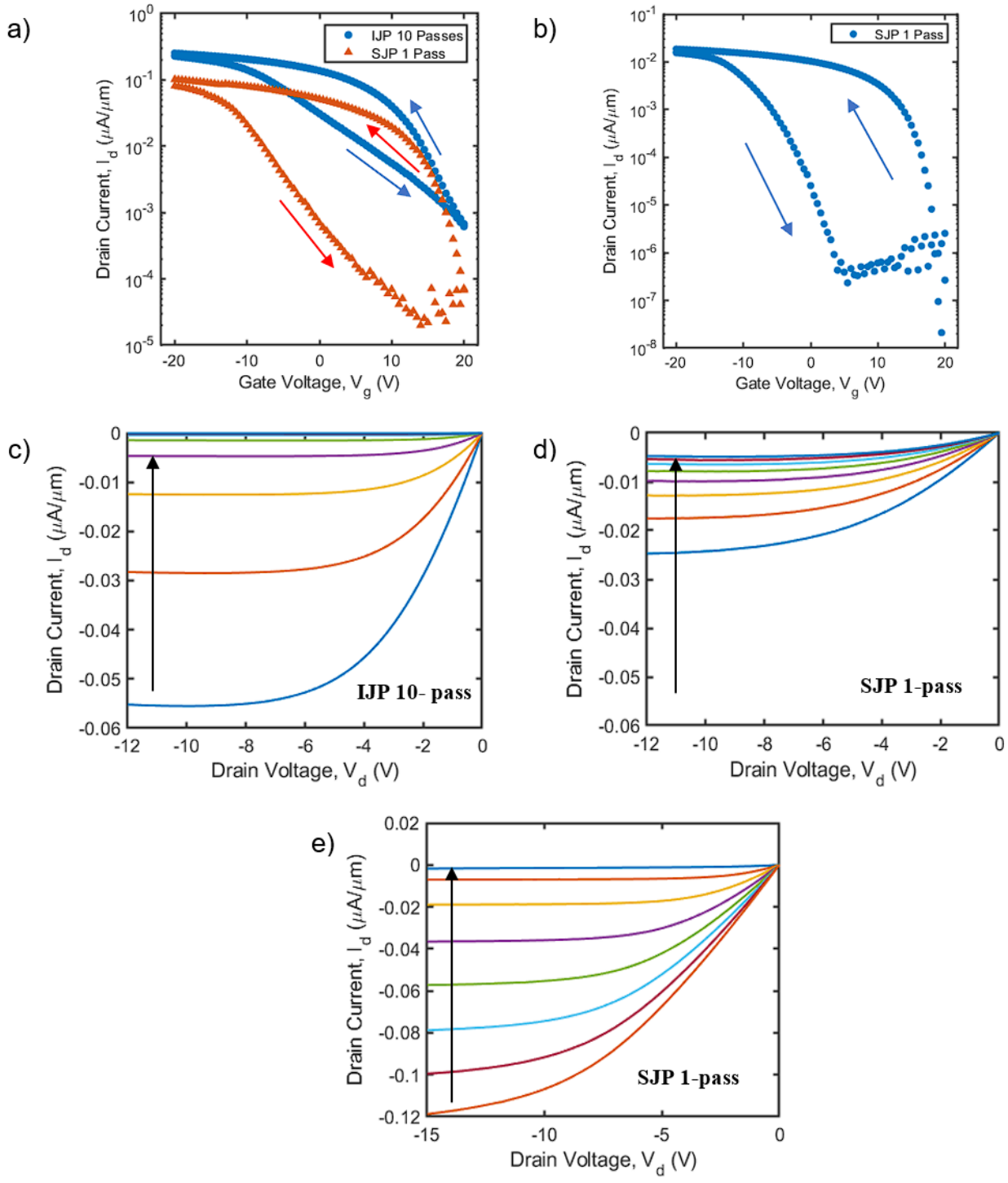


Figure 35. a-b) Transfer characteristics of the CNT-TFT devices for a drain bias of 1V. c-e) I_d-V_d family plots.

For devices with a 60 µm channel length, the extracted mobilities are ~23 $cm^2/V{\cdot}s$ for IJP and ~12 $cm^2/V{\cdot}s$ for SJP, with I_{ON}/I_{OFF} ratios on the order of 10^2 and 10^3, respectively. However, the difference in CNT surface coverage observed in Figure 33 must be considered when comparing electrical performance. A Python-based surface coverage analysis revealed that IJP devices achieve over 90% coverage, while SJP devices cover only 32% of the channel area, as seen in Figure 36.[211–213] Since CNT coverage directly impacts mobility, the channel width in the mobility equation was adjusted to reflect the actual surface coverage. Assuming IJP provides 100% coverage, the effective channel width for SJP was scaled proportionally, resulting in corrected mobility values. After this adjustment, the mobility for SJP devices with a 60 µm channel length increases to ~36 $cm^2/V{\cdot}s$, compared to ~23 $cm^2/V{\cdot}s$ for IJP devices.

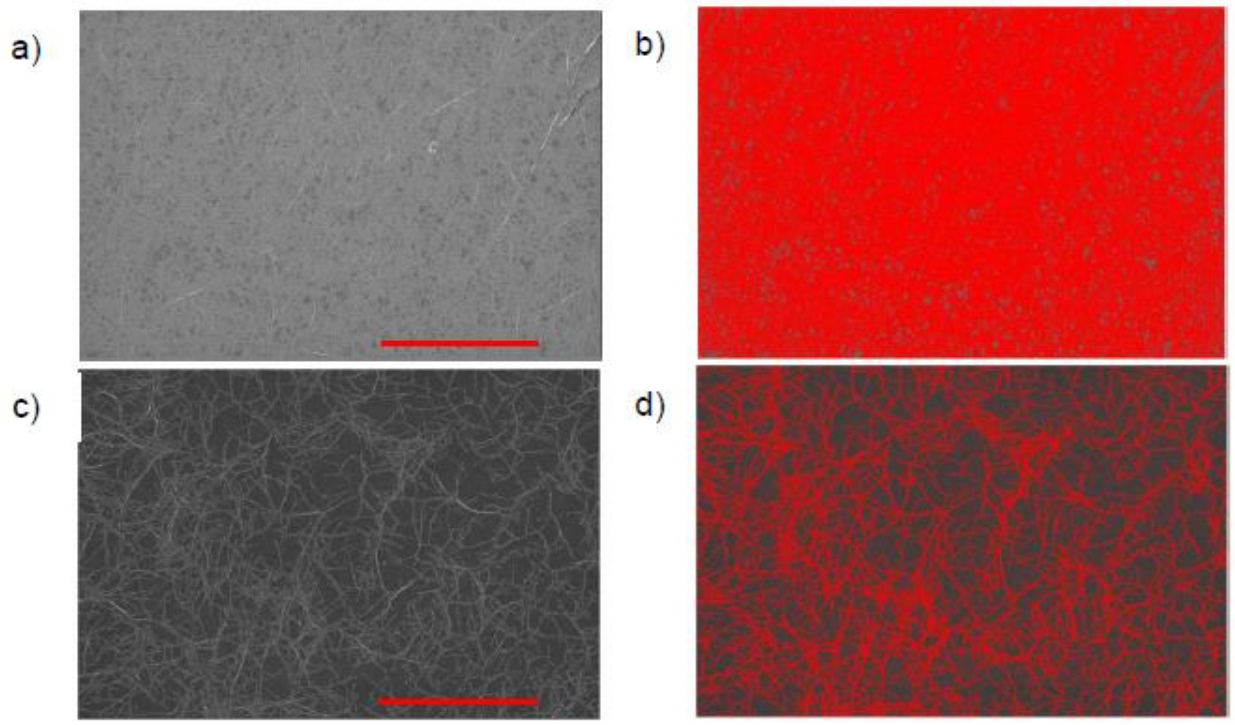


Figure 36. SEM images of representative CNT networks printed by a) IJP (10 passes) and c) SJP (1 print pass). False colored versions are included in b) and d) to extract surface coverage.

This correction aligns with expectations, as SJP preserves the original CNT length, reducing the need for cross-connections between CNT strands. The maximum mobility observed for SJP-printed devices is ~135 cm²/V·s, compared to ~22 cm²/V·s for IJP devices with the same channel length. The I_{ON}/I_{OFF} ratios for SJP and IJP devices are 10^3 and 10^5, respectively. In summary, while IJP devices initially exhibit higher apparent mobility and denser CNT networks due to multiple printing passes, the nozzle-free SJP process demonstrates superior efficiency, preserves CNT length, and achieves higher corrected mobility, highlighting its potential for scalable and high-performance CNT-TFT fabrication.

5.4.4 Printing Unsonicated Ink with SJP

To evaluate the impact of nozzles, unsonicated CNT ink that had been stored for several months, resulting in sporadic clots of tubes, was used. For IJP, this stored ink caused severe nozzle clogging, making printing impossible without filtration or sonication. In contrast, SJP successfully printed the unsonicated ink, and the resulting devices exhibited satisfactory device performance. The transfer characteristics and I_d-V_d family plot, shown in Figures 31b and 31e, demonstrate that these devices achieved a mobility of 10.8 cm²/V·s and an I_{ON}/I_{OFF} ratio of approximately 10^6, values that are acceptable for printed electronic applications.

Despite the successful use of unsonicated ink with SJP, the presence of CNT clots in the ink was noticeable without filtration. These clotted CNTs may have formed pseudo-isolated CNT channels, like nanomesh structures or strip patterns described in previous studies.[214,215] Similar to nanomesh formation, the devices exhibited a reduction in both on- and off-currents, an increase in the I_{ON}/I_{OFF} ratio, and improved transconductance. Reducing the separation between nanoholes in nanomesh structures has been shown to enhance the I_{ON}/I_{OFF} ratio by up to six orders of

magnitude, attributed to a lower probability of metallic CNT subnetworks bridging the source and drain electrodes.[216,217]

In another study, a stick percolation model was used to explain improved device performance resulting from strip patterning.[214,215] This model suggested that increasing the density of semiconducting CNTs beyond the threshold for metallic CNT percolation effectively eliminated current conduction through metallic pathways. This mechanism may similarly explain the performance enhancement observed in SJP-printed devices using unsonicated ink. In summary, SJP demonstrates its robustness by successfully printing operational devices with aged, clumped ink while IJP was unable to print any functional devices.

5.5 Characterization and Performance of SJP-printed CNTs

5.5.1 Compositional and Structural Characterization

The absence of a nozzle and the reduction in sonication during SJP printing result in longer CNT lengths, which can enhance device performance by reducing carrier scattering and improving current conduction.[218,219] Raman characterization, shown in Figure 37, revealed similar D-peaks for IJP and SJP at 1340 cm^{-1}, indicating structural defects and disorder. The G-peak at 1590 cm^{-1}, associated with in-plane vibration, was more prominent for IJP, likely due to the higher CNT density achieved from 10 printing passes. These results confirm the expected morphology of SJP-printed CNTs, as evidenced by the measured maximum effective mobility of ~135 $cm^2/V.s$.

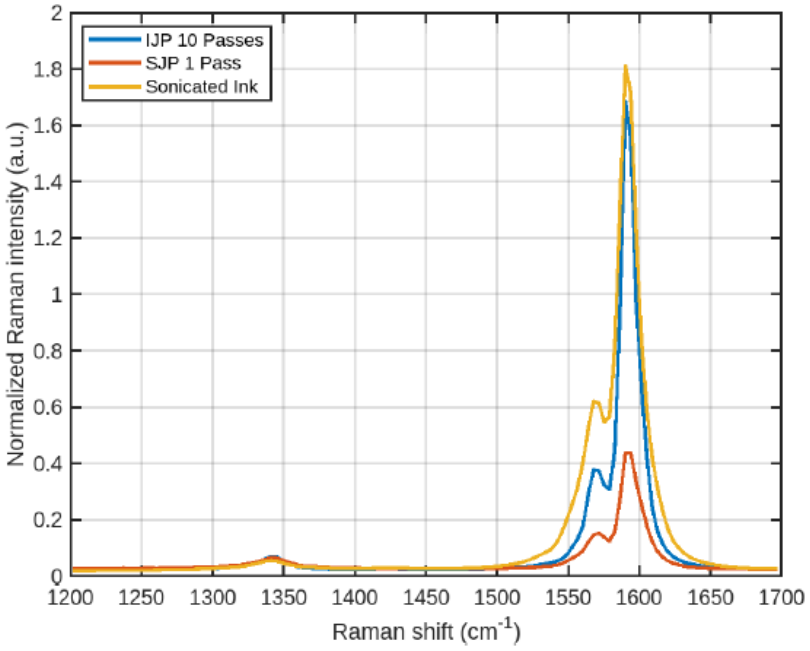


Figure 37. Raman spectra of sonicated ink, as well as IJP and SJP-printed devices.

SJP demonstrates promising electrical performance, even with a single printing pass and lower surface coverage. This can be attributed to the underlying printing mechanism of SJP, where high-speed liquid microjetting deposits a significant volume of CNT ink with better adhesion to both the substrate and the metal contacts compared to IJP. Similar pressure-dependent deposition behavior has been observed in plasma jet printing, where increased precursor flow resulted in thicker films.[220] In contrast, IJP's smaller print volume (2.4 pL per drop, with an individual dot size of 30 µm) and inconsistent adhesion after the first pass led to non-uniform layering between successive print passes. The shorter lengths of IJP-printed CNTs, as shown in Figure 33a and 34a, further complicate the formation of strong interfaces with the source and drain electrodes in bottom-contacted devices. As a result, multiple IJP passes are required to establish electrical connectivity between CNT strands.

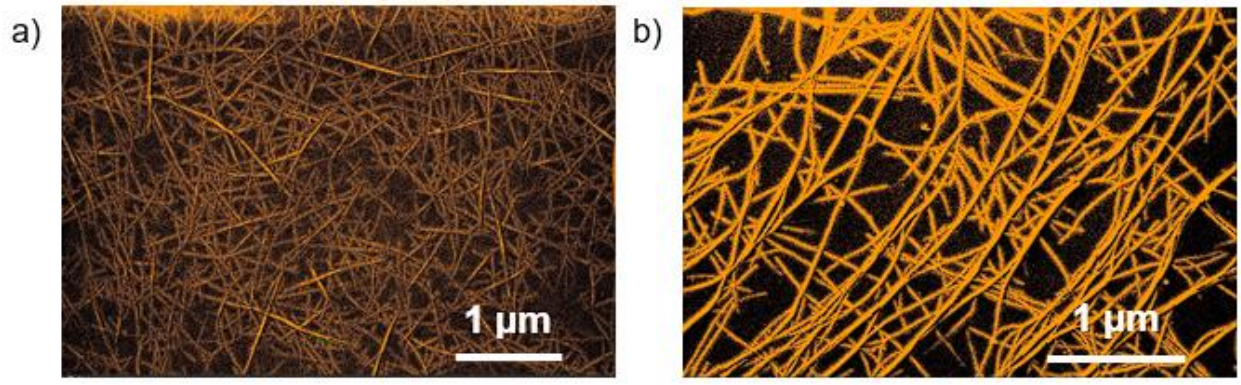


Figure 38. Magnified SEM images of a) 10 print pass IJP channel and b) one print pass SJP channel.

Additionally, IJP printing processes can damage CNTs due to the sonication and nozzle diameter constraints, while SJP avoids these limitations. SEM images clearly demonstrate this difference: the zoomed-in image of an IJP-printed CNT channel in Figure 38a shows broken CNTs that rely heavily on CNT-CNT junctions for conduction between source and drain contacts, whereas SJP-printed CNTs in Figure 38b span the entire image, forming longer, continuous networks. This confirms that SJP can print CNTs with tube lengths matching the full length histogram of the commercially available CNT ink (Figure 31), minimizing CNT damage and improving electrical performance.

5.5.2 Electrical Performance and Reliability Testing

The logarithmic I_{ON}/I_{OFF} versus extracted mobility is plotted in Figure 39a. The trend for IJP-printed CNT-TFT devices appears random, consistent with observations reported in recent literature.[158] In contrast, SJP-printed devices follow the trend typically observed in synthesized random CNT network thin-film transistors.[212,221] Figures 35b and 35c show the mobility and I_{ON}/I_{OFF}, respectively, under varying printing conditions for channel lengths ranging from 2 to 300 µm, with the channel width fixed at 300 µm. Vertical bars represent the range of data points

for each channel length, and mean values are connected for each type of printed device. Unless otherwise specified, all devices were fabricated using sonicated ink.

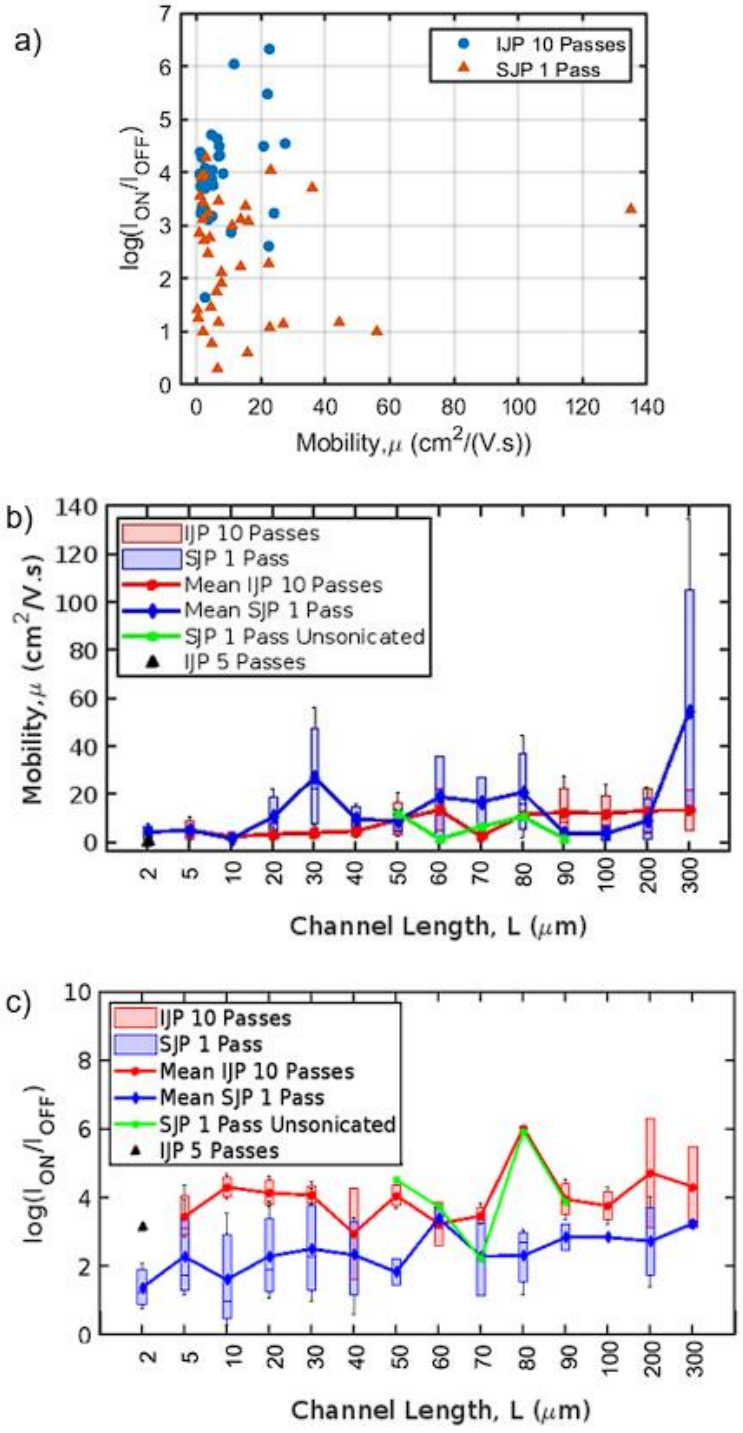


Figure 39. a) I_{ON}/I_{OFF} with respect to mobility for both printer types. b) Mobility and c) log (I_{ON}/I_{OFF}) versus channel length for various printing tests.

For IJP devices, mobility showed a minor increase with increasing channel length, aligning with previously reported results.[217] However, SJP devices showed no clear trend for channel lengths below 100 µm. Beyond 100 µm, mobility exhibited an increasing trend, with SJP demonstrating superior mobility for devices with a channel length of 300 µm, the maximum length studied. While SJP devices achieved better mobility at 300 µm, the variability (as indicated by the standard deviation) was five times larger than that of IJP devices.

Devices printed with unsonicated ink followed a distinct mobility trend, falling between sonicated SJP and IJP devices. The I_{ON}/I_{OFF} versus channel length showed an increasing trend for IJP devices, whereas SJP devices displayed a relatively flat response. Across the channel length range of 2 to 300 µm, I_{ON}/I_{OFF} values for IJP-printed CNT-TFTs outperformed those of SJP devices printed with sonicated ink. However, SJP devices printed with unsonicated ink exhibited a trend comparable to IJP devices, albeit with limited data points. The higher I_{ON}/I_{OFF} values in unsonicated ink-printed SJP devices may be attributed to clotted CNTs forming additional CNT-CNT junctions, creating a denser CNT network compared to devices printed with sonicated ink.

These findings highlight the potential of SJP to overcome key challenges such as nozzle clogging, while expanding the application space for random CNT networks and other nanomaterial films in areas such as optoelectronics, flexible electronics, sensors, and radio frequency (RF) communications.

Chapter 6 Shock-wave Jet Printing of Solid Functional Materials

6.1 Introduction to Solid-State Printing and Functional Materials

6.1.1 Overview of Functional Solid Materials in Advanced Manufacturing

Functional solid materials, such as organic molecules, polymers, and crystalline structures, are vital for developing next-generation devices, including OLED displays, photodetectors, and sensors. Among these, organic molecules play a particularly important role in enabling advanced optoelectronic technologies, with applications in high-performance and flexible displays. For example, OLED displays are rapidly transforming the display industry, offering the potential for flexible and immersive augmented reality systems in daily life.[222,223] Materials like Br1A/Br1 cocrystals and diketopyrrolopyrrole (DPP8) are notable for their emissive properties, stability, and phase versatility, which make them excellent candidates for integration into these systems.[224–227]

Polymers and crystalline solids further enhance the functionality of these materials by providing mechanical durability, thermal resilience, and electrical conductivity, enabling their use in a wide array of advanced electronics. As manufacturing technologies evolve, these materials remain at the forefront, supporting the development of increasingly efficient, compact, and multifunctional devices capable of meeting the demands of modern industries.

This chapter is based on work done in collaboration with Mira Diab El Harakeh, Jinsang Kim, and L. Jay Guo.

6.1.2 Challenges in Traditional Printing of Solid Materials

Conventional manufacturing methods, such as thermal vacuum evaporation, have long dominated the production of high-performance devices like OLED displays but face significant limitations. Thermal vacuum evaporation, while effective for producing long lasting and efficient OLEDs, results in substantial material waste due to isotropic sublimation during deposition.[228,229] Additionally, the high deposition temperatures required for thermal vacuum evaporation can degrade sensitive organic materials, limiting the range of compatible materials for high-performance devices. Nozzle clogging in the linear sources of thermal evaporators further complicates the consistent deposition of organic materials.[230]

Another issue with thermal evaporation is the reliance on fine metal masks (FMMs) to create RGB pixels for large-area displays. These masks are prone to deformation during fabrication, adding to manufacturing complexities.[231] Additionally, display resolution is limited to approximately 8K (254 μm linewidth) when using FMMs with thermal deposition techniques. Companies like LG Display have sought to address these issues by incorporating color filters on white OLEDs to avoid FMM-related challenges.[232]

These challenges underscore the urgent need for innovative additive manufacturing techniques, such as shock-wave jet printing. This approach eliminates nozzle clogging, reduces material waste, and preserves the functional integrity of organic materials. Such advancements have the potential to significantly impact the display and optoelectronics industries, enabling more efficient and scalable manufacturing processes for next-gen technologies.

6.2 Fundamentals of Shock-wave Jet Printing for Solid Materials

6.2.1 Mechanism of Solid Material Ejection via Shock-wave Jet Printing

Shock-wave jet printing (SJP) is an advanced technique that uses laser-generated focused ultrasound (LGFU) to eject materials with precision and control. While SJP was previously demonstrated for liquid inks, its principles can be expanded to eject clusters of solid materials. In this process, a pulsed laser, such as an Nd:YAG laser, generates acoustic waves by striking a photoacoustic (PA) lens coated with a composite of soot embedded in polydimethylsiloxane (PDMS). These acoustic waves are focused through a water capsule and directed to a transfer layer holding the solid material. The high-pressure shock waves are generated through cavitation at the focal point.[196,197] When cavitation occurs just below the transfer layer, the resulting shock waves eject clusters of material onto a receiving substrate. The experimental setup is illustrated in Figure 40 and described in further detail in Appendix B.

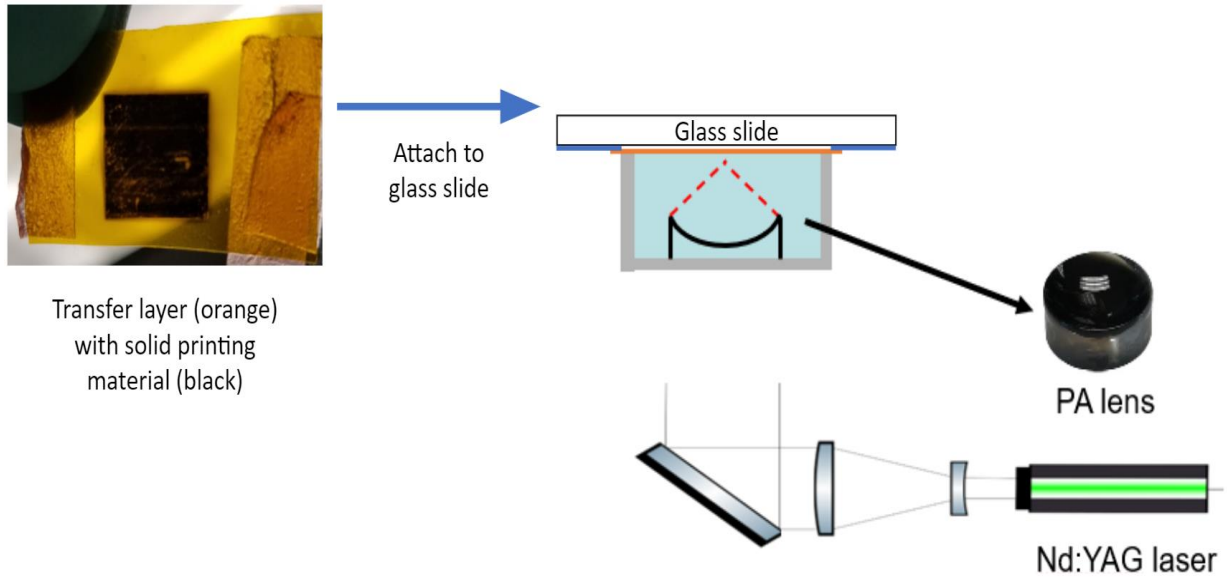


Figure 40. The SJP experimental setup with a thin transfer layer (orange).

The transfer layer, typically made from mechanically stable films like polyethylene terephthalate (PET) or polyimide (Kapton), is designed to withstand the localized stresses during printing. Parameters such as the distance between the acoustic focal point and the transfer layer, laser energy, and pulse duration are optimized to ensure consistent material ejection without causing degradation, as described in section 5.3.2. This nozzle-free, non-contact mechanism minimizes clogging risks and preserves the structural integrity of delicate solid materials. The receiving substrate can also be modified, for instance, with a PDMS coating, to enhance material retention and achieve high-resolution patterns with micron resolution. By extending SJP to solid-state materials, this work demonstrates a novel additive manufacturing approach capable of depositing functional layers with exceptional precision and material integrity.

6.2.2 Advantages of SJP for Solid-State Materials

SJP offers several key advantages over traditional methods for depositing solid-state materials. The most significant benefit is its nozzle-free design, which eliminates the risk of clogging, a common issue in ink-based techniques, particularly for complex or clotted materials. This feature expands the range of materials that can be used, including thermally sensitive organics, supercooled liquids, and crystalline solids, which often degrade under the high temperatures required for methods like thermal vacuum evaporation.

In addition to its broad material compatibility, SJP achieves exceptional resolution, producing features as small as 20–30 μm on a wide variety of substrates.[191,198] Its non-thermal process ensures that the structural and functional properties of the materials remain intact, making it particularly valuable for applications in optoelectronics and sensors. Furthermore, the high-speed nature of SJP, enabled by rapid laser pulses, reduces material waste and improves efficiency. These advantages position SJP as a transformative technology in advanced

manufacturing, providing a scalable and cost-effective alternative for integrating solid functional materials into next-generation devices.

6.2.3 Selection of Functional Materials for SJP

The selection of functional materials for SJP is guided by their thermal stability, phase behavior, and compatibility with the receiving substrate. Materials must endure the high-pressure shock waves generated during the process while maintaining their structural and functional integrity. Organic molecules, including diketopyrrolopyrrole (DPP8) and Br1A/Br1 cocrystals, are excellent candidates due to their emissive properties, thermal resilience, and phase versatility. For example, DPP8 can exist as a supercooled liquid or crystalline solid, shown in Figure 41, providing opportunities to study phase-dependent behavior during printing.

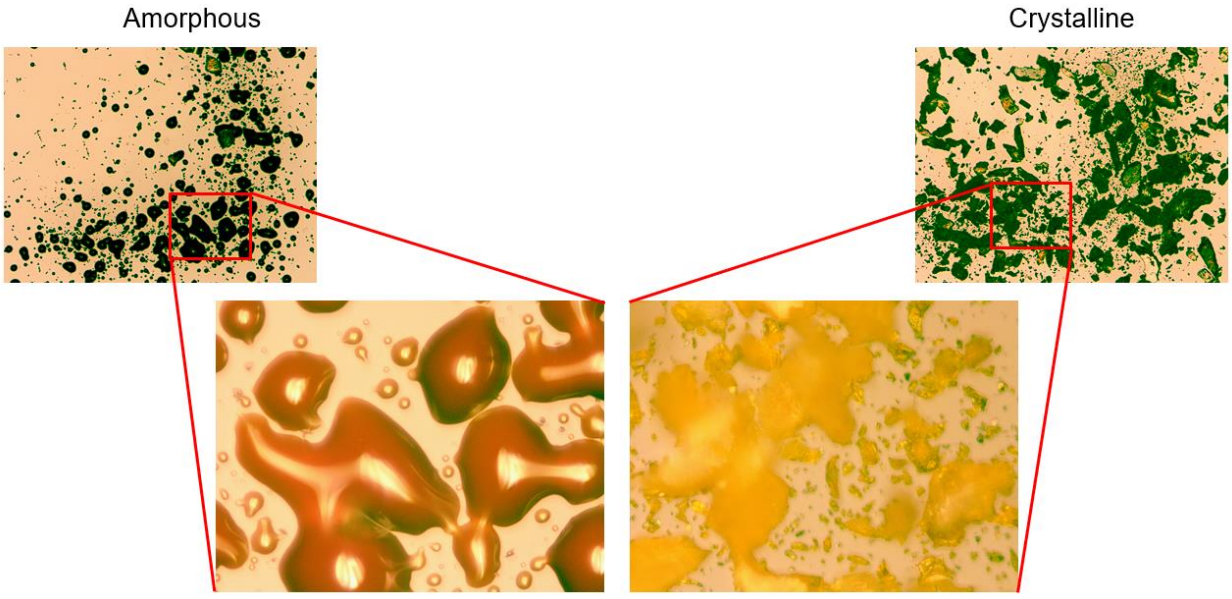


Figure 41. DPP8 molecule in its amorphous, supercooled liquid (left) and crystalline (right) states.

Supercooled DPP8, also referred to as amorphous DPP8, has been shown to crystallize under shear vibrations.[224] SJP offers a unique opportunity to induce this crystallization during the deposition process, potentially creating crystalline patterns directly on the substrate. The

compatibility of these materials with SJP expands the range of applications, from optoelectronic devices to advanced sensors, while maintaining material integrity throughout the printing process.

.

6.2.4 Challenges and Techniques in Printing Organic Molecules

Printing organic molecules presents unique challenges due to their sensitivity to thermal and mechanical stresses during deposition. The material phase, whether supercooled liquid or crystalline, significantly affects deposition quality and resolution. Supercooled liquids may spread uncontrollably on receiving substrates, while crystalline solids may not adhere uniformly. These challenges require process optimization to ensure precise patterning and material retention.

Photoacoustic printing addresses these issues by offering a non-contact, nozzle-free approach that minimizes thermal degradation and preserves the molecular integrity of the molecules. Modifying the receiving substrate, such as applying a PDMS coating, can improve material adhesion and reduce spreading, while fine-tuning the travel distance between the transfer layer and the substrate improves resolution. For example, DPP8 has been successfully deposited on glass substrates, producing well-defined patterns that maintain their emissive properties. By addressing these optimization techniques, SJP provides a reliable and efficient method for integrating organic molecules into advanced optoelectronic devices without compromising their functional characteristics.

6.3 Case Study: Printing of Organic Molecules and Crystals

6.3.1 Morphological Characterization of Printed Solid Materials

The morphology of printed solid materials primarily depends on the properties of the transfer layer, including its uniformity, thickness, and crystal grain boundary size. SJP transfers solid materials in the form of macroscopic clusters rather than individual molecules, as shown in Figure 42. These clusters are influenced by the thickness and homogeneity of the transfer layer. Thinner and more uniform transfer layers result in smaller, more evenly distributed printed crystals. This trend was observed for both diketopyrrolopyrrole (DPP8) and Br1A/Br1 cocrystals, where thinner transfer layers enabled more controlled material ejection and smaller crystal sizes on the receiving substrate.

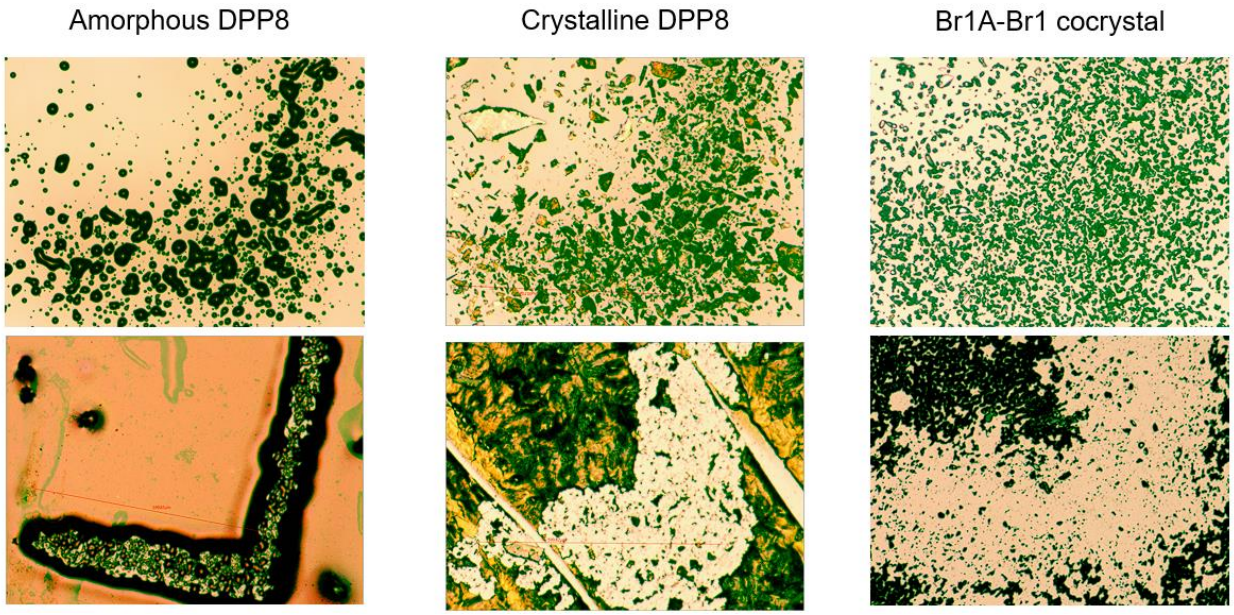


Figure 42. SJP-printed 600 μm “L” patterns for three transfer layers.

Additionally, cavitation shock waves generated during photoacoustic printing induced crystallization in DPP8 layers, as illustrated in Figure 43. The shock waves crystallized the base of the transfer layer, seen by the crystalline patterns in the transfer layer “L” and the appearance

of yellow fluorescence at 420 nm excitation. Some of this crystalline DPP8 was transferred to the printed pattern, demonstrating the dual role of shock waves in material ejection and structural modification. This capability highlights the potential of SJP not only to deposit materials but also to influence their structural properties during the process.

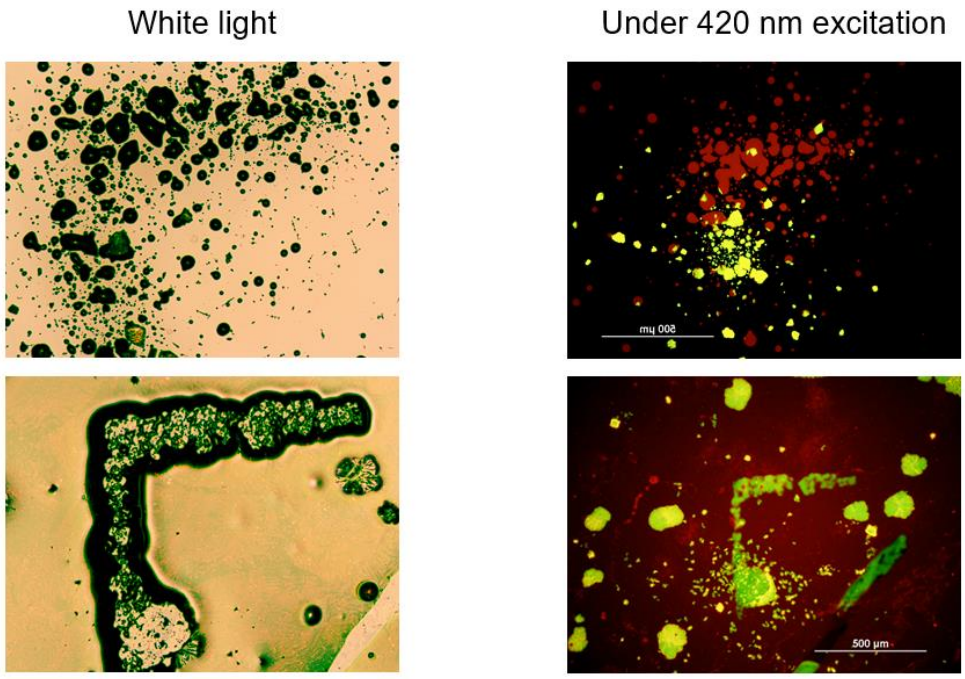


Figure 43. Fluorescence of printed DPP8 molecules, demonstrating crystallization along the transfer layer base (bottom right).

6.3.2 Optimization of Solid Printing Patterns

Optimizing the printing patterns of solid materials requires careful control of process parameters, particularly the travel distance between the transfer layer and the receiving substrate. Reducing this distance, determined by spacer thickness, minimizes material dispersion and enhances resolution, resulting in well-defined patterns. PET, Kapton, and PDMS spacers with variable thicknesses were tested, allowing spacing distances between 25 to 50 µm. However, to achieve smaller distances, glass microbeads with diameters as small as 7.5 µm were evaluated.

These smaller travel distances led to significant improvements in print resolution, achieving pattern resolutions as fine as 100 μm, as shown in Figure 44.

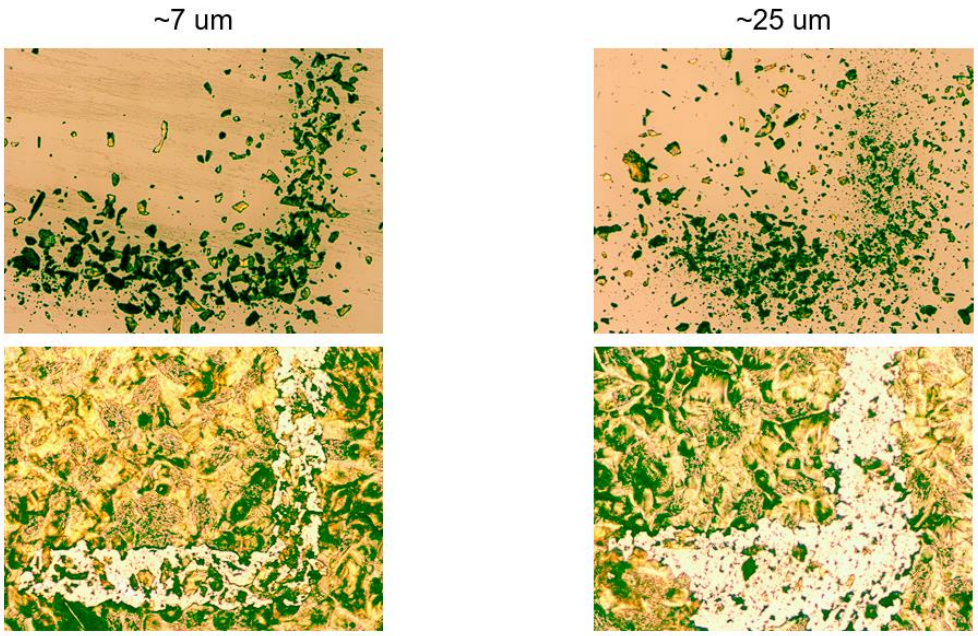


Figure 44. Crystalline DPP8 patterns for two different travel distances.

The receiving substrate properties also play a significant role in optimizing print quality. Figure 45 demonstrates four coatings with distinct differences in pattern resolution for amorphous DPP8, findings that were consistent across Br1A/Br1 and crystalline DPP8 materials. Sticky, viscoelastic coatings, such as PDMS, effectively captured printed material, reducing material loss and improving pattern retention. These coatings improved adhesion and minimized spreading, which is particularly important for materials with low cohesion.

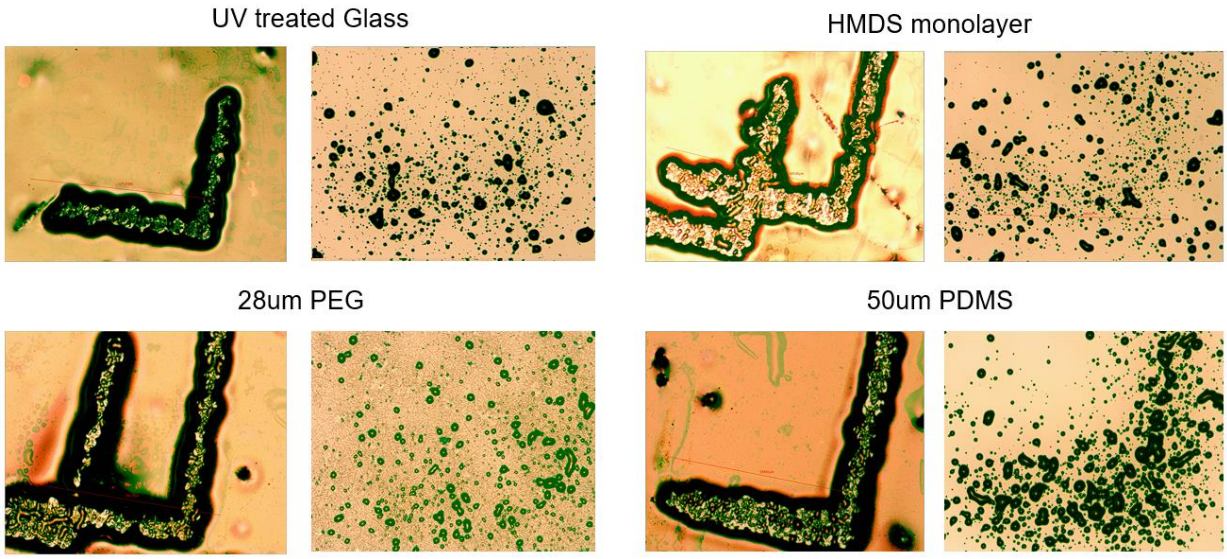


Figure 45. SJP-printed amorphous DPP8 on four glass coatings.

By refining the transfer layer, travel distance, and substrate properties, SJP achieves high-resolution, reproducible patterns of solid functional materials. These advancements pave the way for integrating solid-state materials into advanced manufacturing processes, enabling scalable production of high-performance devices for optoelectronics, sensors, and other emerging technologies. This optimization highlights the potential of photoacoustic printing to overcome existing limitations in material deposition and drive innovation in solid-material-based applications.

Chapter 7 Conclusion and Future Work

7.1 Summary of Key Findings

This thesis explores the advancement of thin-film coatings, structural color applications, and novel printing techniques for functional materials, bridging the gap between material innovation and scalable manufacturing. Each chapter builds on foundational principles and demonstrates how these technologies can address limitations in current processes while enabling cutting-edge applications.

The study begins with an exploration of structural color coatings, emphasizing their ability to produce vibrant colors without relying on pigments or dyes. High-low-absorber (HLA) and metal-dielectric-metal (MDM) stacks were investigated as fundamental structures for achieving vivid colors. HLA stacks, composed of abundant dielectric materials like SiO_2 and TiO_2, offer a cost-effective alternative to MDM structures by avoiding expensive metallic layers. Meanwhile, the tunability of MDM structures, with their sharp spectral contrast, makes them ideal for advanced applications. These findings underscore the potential of structural color coatings to combine vibrancy, environmental sustainability, and economic feasibility, setting the stage for more complex applications.

Building on the principles of structural color, the use of raw, minimally processed minerals as source materials for thin-film deposition was explored. Electron-beam evaporation demonstrated its effectiveness in purifying and depositing impure starting materials like rutile-derived TiO_2 and silica-based SiO_2. X-ray photoelectron spectroscopy (XPS) revealed key insights into the optical and material properties of these coatings, highlighting the potential of

raw mineral sources to produce high-quality films. Best practices for deposition were established, emphasized the importance of the evaporation mechanism, and demonstrated the environmental and economic advantages of using abundant, natural resources in optical coatings.

Structural color coatings were extended to advanced applications, such as structural black coatings, thermochromic films, and fused glass systems. Modified MDM designs were optimized to achieve near-zero reflection for structural black coatings, suitable for automotive and decorative applications. TiO_2 films exhibited reversible thermochromic behavior, demonstrating their potential as temperature sensors in integrated electronic systems. Additionally, structural color flakes were successfully fused into glass coatings, producing scratch-resistant, aesthetically appealing surfaces. These innovations highlight the versatility of structural color coatings in both functional and decorative contexts.

Area-selective atomic layer deposition (AS-ALD) was then introduced as a method to create conformal and patterned color coatings. By using polymer inhibitors deposited via electrohydrodynamic jet printing, structural colors were precisely patterned with submicron resolution. AS-ALD enabled the fabrication of high-aspect-ratio conformal coatings and allowed for detailed designs on irregular substrates. This advancement showcases the potential of AS-ALD in optical and electronic applications, where precision patterning enhances both aesthetics and functionality.

The focus shifted to shock-wave jet printing (SJP) for fabricating carbon nanotube (CNT) thin-film transistors (TFTs). SJP was shown to overcome challenges associated with inkjet printing, such as nozzle clogging and material damage. By preserving the length and integrity of CNTs, SJP achieved functional devices with fewer printing passes, demonstrating higher efficiency and lower material consumption. Mobility correction analysis revealed superior

performance of SJP-printed devices compared to inkjet-printed counterparts, highlighting the suitability of SJP for scalable electronic applications.

The application of SJP was then expanded to solid organic molecules, such as diketopyrrolopyrrole (DPP8) and Br1A/Br1 cocrystals. The morphology of printed materials was influenced by the transfer layer properties, such as thickness and uniformity, as well as process parameters like travel distance and substrate coatings. Cavitation-induced shock waves were found to crystallize DPP8 during printing, demonstrating SJP's ability to simultaneously deposit and structurally modify materials. The ability to produce high-resolution patterns of organic molecules without thermal degradation underscores SJP's potential for advanced optoelectronic devices.

7.2 Future Research Directions

This thesis has demonstrated innovative advancements in structural color coatings and shock-wave jet printing (SJP) for both liquid and solid functional materials. Each chapter has provided insights into the limitations of current technologies while introducing novel solutions for optoelectronics, sensors, and manufacturing processes. Building on these findings, future research directions are proposed to address existing challenges and unlock the full potential of these technologies.

Structural color coatings could benefit from further optimization of deposition conditions to improve stability and long-term durability. Future studies could explore alternative abundant materials for novel optical layers, expanding the range of achievable colors while maintaining environmental sustainability. These efforts would lay a foundation for machine learning approaches to predict and optimize thin-film designs for specific optical properties, including color purity, reflection, and absorption. Such a framework would enable rapid development of

coatings for advanced applications, such as filters for integrated photonic devices or large-area decorative panels.

Thermochromic films, demonstrated as temperature sensors, could be combined with integrated optical sensing systems for real-time heat monitoring in electronic and photonic devices. Additionally, scaling up glass fusing methods to produce large-area structural color films could enable applications in architecture and renewable energy, such as decorative windows and scratch-resistant solar panel coatings. Research into improving the homogeneity and reproducibility of fused coatings would further enhance their functionality and visual appeal.

While AS-ALD offers precision for patterned coatings, its throughput could be significantly increased by integrating Spatial ALD (SALD). This approach could combine high-speed deposition with real-time optical monitoring of film uniformity and thickness, using the color of the deposited layer as a diagnostic tool. Such developments would allow for scalable production of conformal coatings with optical or electronic functionality, broadening their industrial applicability.

SJP demonstrated significant potential for fabricating CNT-based thin-film transistors (TFTs), but device performance variability remains a challenge. Future research should focus on optimizing ink formulation, processing steps, and substrate functionalization to enhance reproducibility. Controlling the CNT ink bath temperature during printing could further improve uniform deposition and reduce defects in the printed network. These advancements would enable SJP to compete more directly with established methods like inkjet printing (IJP) while addressing nozzle-clogging issues inherent to nozzle-based systems.

SJP's application to solid functional materials, including organic molecules, has shown promise but requires further refinement. Improvements in resolution and deposition uniformity

are essential to produce functional devices. For applications like transistors or OLEDs, the deposited molecules must form continuous, uniform layers rather than fragmented crystals. Future studies could explore process optimization, including transfer layer materials, cavitation control, and substrate modifications. Multiple print passes can improve pattern density, and incorporating multiple SJP printing heads can increase the throughput. Expanding the SJP process to print fully functional devices, such as organic light-emitting diodes or photodetectors, would validate its potential as a transformative tool in advanced manufacturing.

Both structural color coatings and SJP have demonstrated strong potential for scalable production, but further research is needed to integrate these techniques into automated manufacturing workflows. Exploring hybrid approaches, such as combining ALD with SJP or fusing structural color coatings with existing large-scale deposition technologies, could broaden the impact of this work across multiple industries.

The findings of this thesis provide a robust foundation for future research into scalable, cost-effective, and environmentally sustainable manufacturing methods. By addressing current limitations and utilizing interdisciplinary approaches, these technologies could revolutionize fields like optoelectronics, sensors, and functional coatings. With continued development, the innovations presented here have the potential to significantly impact both scientific progress and industrial practices.

Appendices

Appendix A: The Custom-Built Evaporator Setup

A custom-built electron-beam (e-beam) evaporator system was developed between 2020 and 2023 in collaboration with Yian Cheng to facilitate the testing and evaporation of impure materials, as described in Chapter 2. Unlike pre-assembled systems, this evaporator was built using individual components, requiring extensive knowledge of circuitry, mechanical integration, and system assembly.

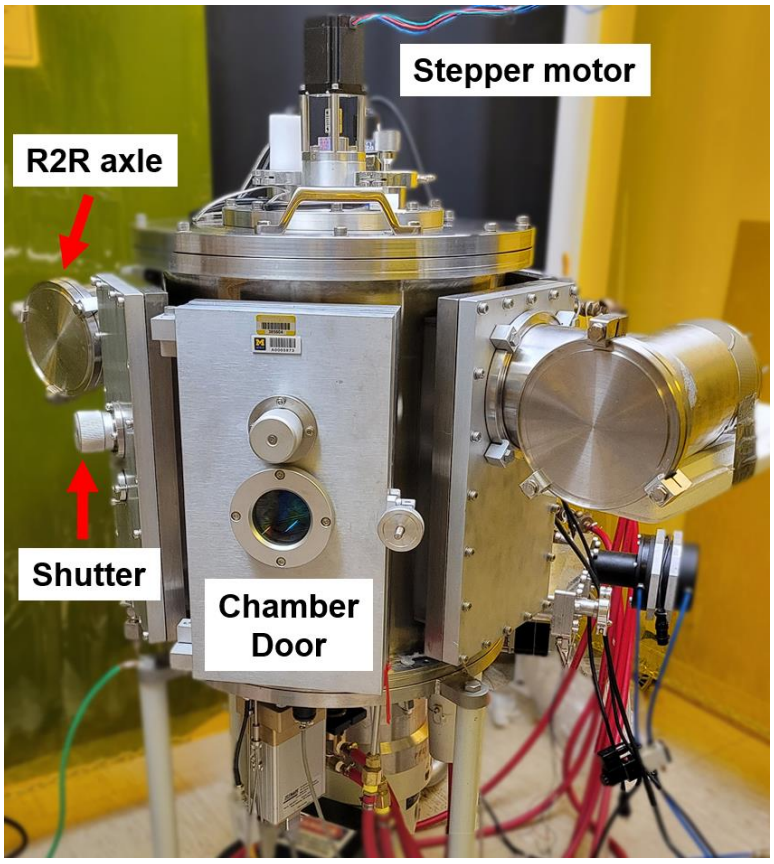


Figure 46. Exterior of the custom-built evaporator chamber.

The system's vacuum chamber and pumps are essential components for maintaining the necessary low-pressure environment for deposition. The vacuum chamber is a six-sided cylindrical structure with five removable walls. Two of these walls are equipped with roll-to-roll (R2R) axles, intended for future R2R sputtering deposition. Another wall features a rotating handle to manually control the source shutter, while the adjacent wall serves as the chamber door. The wall opposite the door houses the feedthrough for the rough and turbo pumps, enabling vacuum operations.

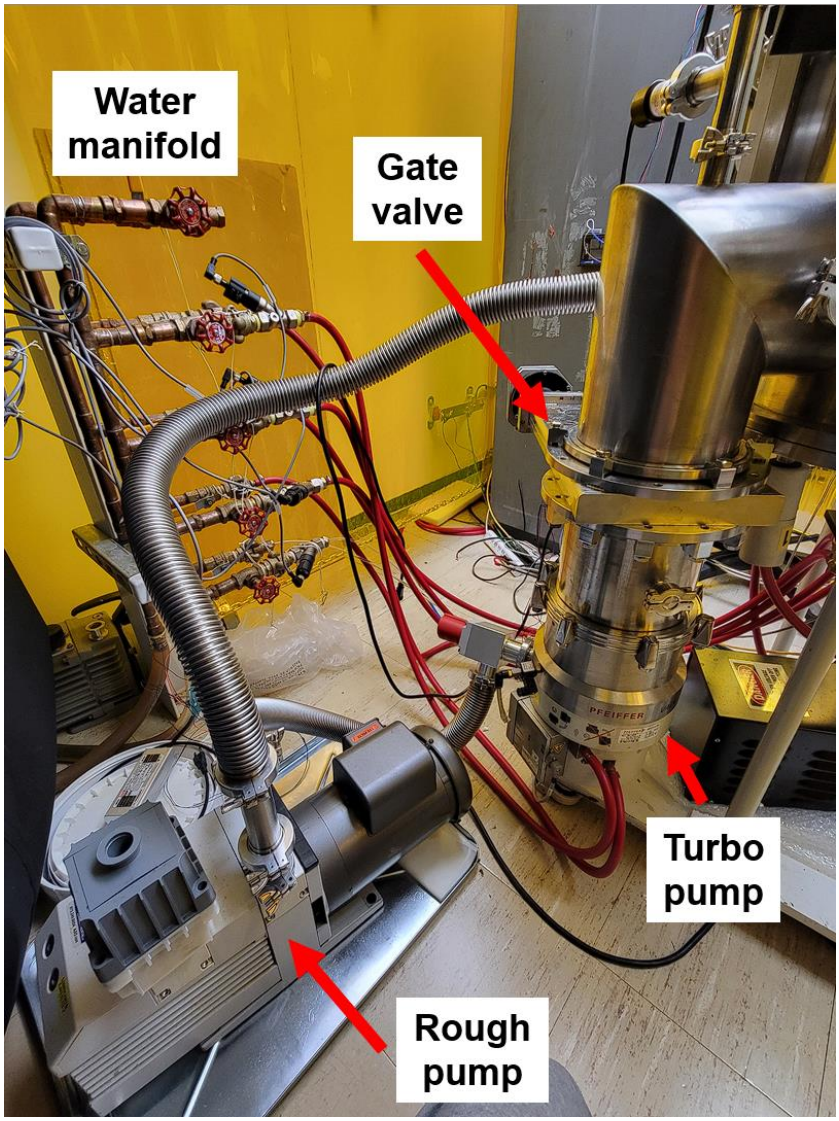


Figure 47. Vacuum and water-cooling system of the custom-built evaporator.

The rough pump, a Leybold D25B, has two attachments controlled by manually actuated valves: one attachment connects directly to the chamber feedthrough, and the other connects to the foreline of a Pfeiffer TMH 1001P turbo pump. The turbo pump is connected to the chamber via a pneumatic gate valve. During operation, the rough pump is used to evacuate the chamber to 10 Pa. At this point, the rough pump is closed from the chamber and the gate valve is opened, allowing the turbo pump to bring the chamber to high vacuum. Meanwhile, the rough pump connection is switched, pulling from the turbo foreline and managing its exhaust. Chamber pressure is monitored throughout the process using a ZDF-5227A composite vacuum gauge.

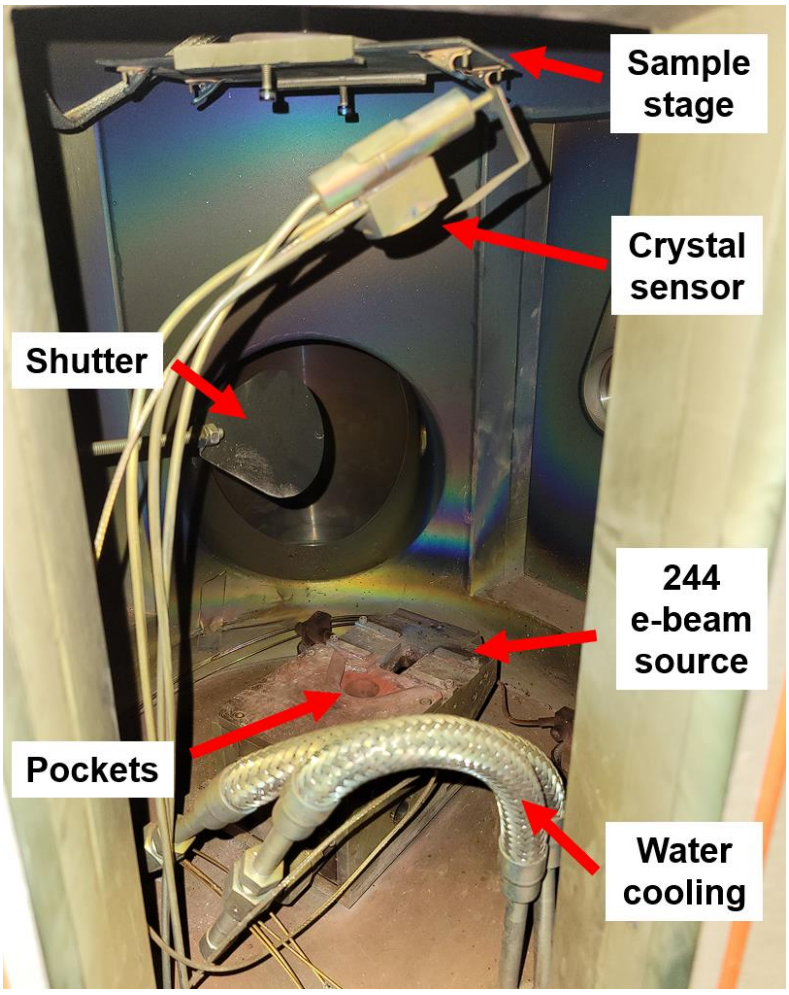


Figure 48. Interior of the custom-built evaporator chamber.

Once the chamber reaches the desired deposition pressure, the e-beam system is activated. The chamber contains a Telemark 244 e-beam source equipped with six pockets, each able to hold crucible liners with a 4 cubic centimeter capacity. The system's operations are managed by a Telemark 861 deposition controller, which regulates the power supplied to the tungsten filament, generating the e-beam. The 861 controller also monitors the deposition rate using a 5 MHz gold-coated quartz crystal sensor mounted near the chamber ceiling. Material selection is managed via a pocket rotation mechanism operated by a Telemark indexer. A Telemark ST high-voltage power supply drives the e-beam source, and its sweep is controlled by a Telemark XY sweep system, which determines the amplitude, shape, and frequency of the beam's movement. After deposition, the 861 controller ramps the e-beam power down, the ST power supply is turned off, the pneumatic gate valve is closed, and the chamber is vented.

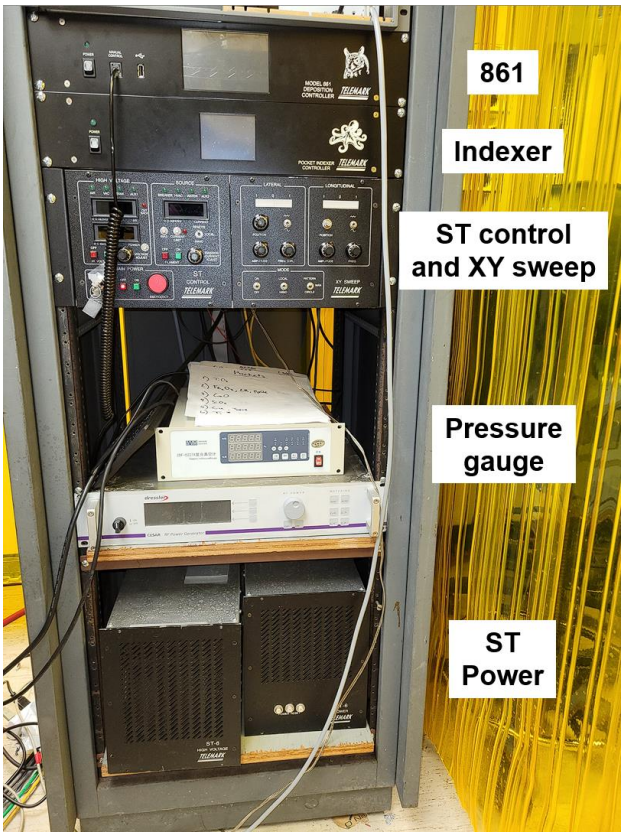


Figure 49. Controllers of the custom-built evaporator.

The substrate stage, located at the top of the chamber, is rotated at 20 rpm during deposition by a stepper motor controlled by an Arduino microcontroller. This setup ensures uniform film deposition across the substrate. To manage heat generated during operation, the turbo pump, 244 e-beam source, and quartz crystal sensor are water-cooled via a custom-built water manifold that filters city water. Proper operation requires the cooling water to be turned on at the start of the process and turned off upon completion.

This custom-built evaporator system has been instrumental in exploring the deposition of impure materials, offering precise control over deposition parameters and paving the way for further developments in material research. An additional benefit of this private system is the ability to deposit any material without the risk of contaminating other users' samples, a concern in shared cleanroom systems. This flexibility enables the exploration of unconventional or impure source materials, expanding the scope of potential applications and fostering innovative research.

Appendix B: The Shock-wave Jet Printing Setup and TFT Device Fabrication

The Shock-wave Jet Printing (SJP) Setup:

The SJP system is a novel, nozzle-free printing technology that converts pulsed light energy into focused ultrasound. This ultrasound generates microcavitation at the focal point within a liquid, producing shock waves that eject material upward as a jet for liquids or as particle clusters for solids. Since inheriting this system in 2020, I have significantly overhauled its structure, completing many of the updates with the assistance of Daniel Penley.

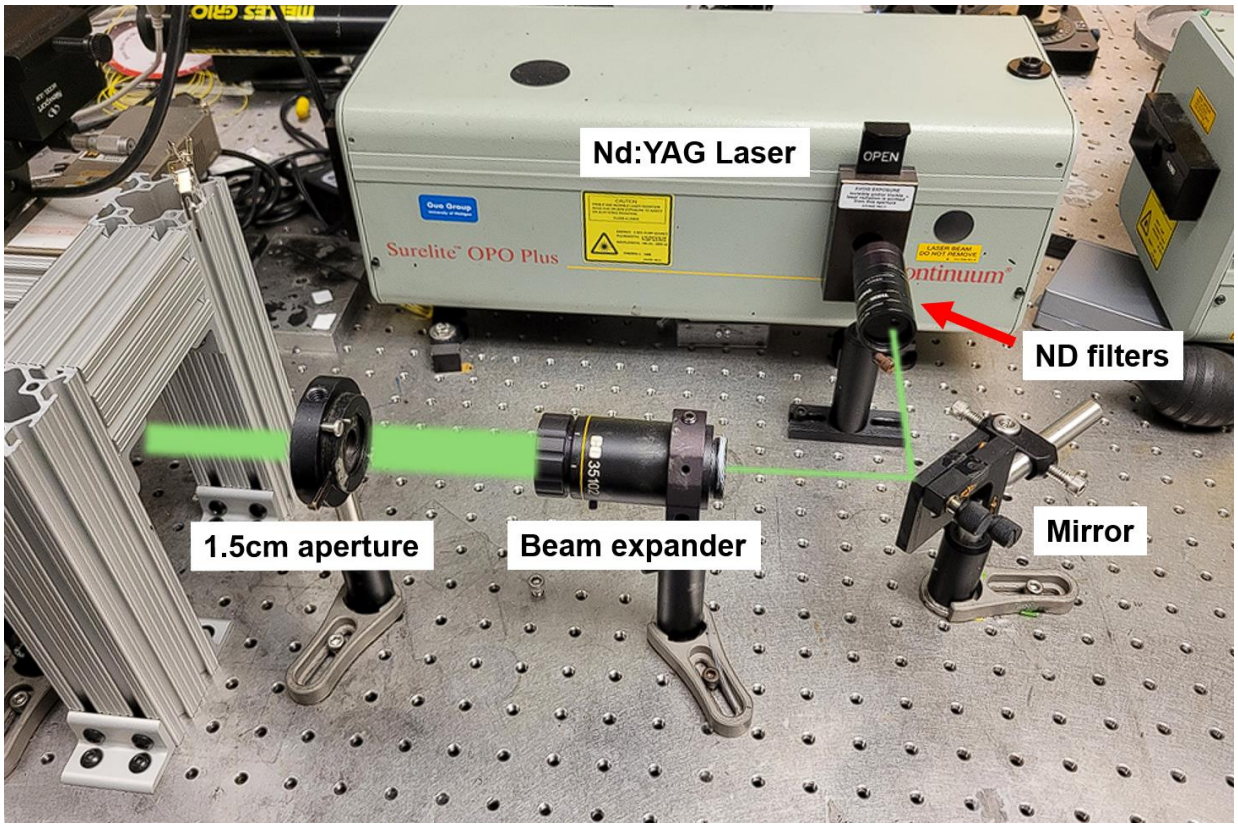


Figure 50. Optics of the SJP system.

The SJP system employs a Surelite I Nd:YAG laser operating at a wavelength of 532 nm, with 6 ns pulses at a frequency of 20 Hz. The laser's 6 mm beam is expanded to a diameter of 1.5 cm to match the size of the photoacoustic (PA) lens, illuminating it from below. The PA layer on the lens absorbs the incident light, converting it to heat, which causes rapid thermal expansion and generates sound waves. These waves are geometrically focused based on the curvature of the lens. When the ink is filled to the correct height, the focal point is located just a few microns below the liquid's surface, producing small, visible bubbles when the laser is activated. These bubbles are caused by the turbulent ink surface due to shock waves and microjets, though the jets themselves are not visible to the naked eye.

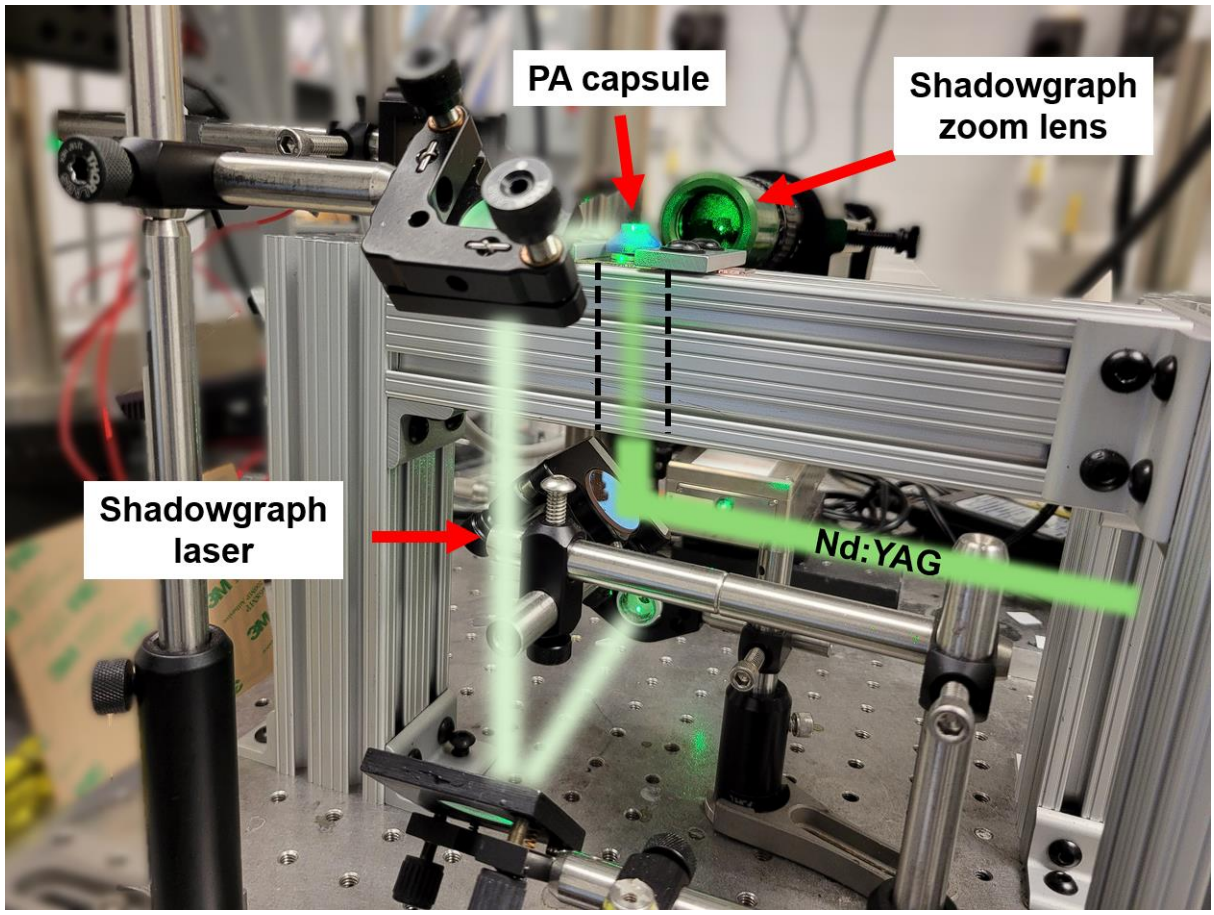


Figure 51. PA capsule and shadowgraph lens of the SJP system.

To visualize the microjets, a shadowgraph system is employed. As shown in Figure B2, a small tabletop laser illuminates the side of the PA capsule, while the background illumination passes through a zoom lens. A CCD camera attached to the other side of the zoom lens captures the laser intensity. Since the ink surface blocks part of the light, the camera records it as a shadow. Continuous operation of the SJP system does not make the jets visible, so the tabletop laser is synchronized to pulse only when a jet is present. This synchronization is achieved using a delay generator, which pulses the tabletop laser 220 μs after the Nd:YAG laser fires, accounting for the propagation time of the ultrasound.

For CNT printing, a heating pad is placed on the backside of the substrate to assist solvent evaporation. For solid printing, a transfer layer is applied to the front of the sample, with two spacers on either side of the printing region. This ensures that the solid material faces the sample, while the PET or Kapton faces the PA capsule. Once prepared, samples are clamped into a 3D translation stage and carefully lowered toward the PA capsule. For liquid printing, the sample should be positioned ~200 μm from the liquid surface. For solid printing, the sample is lowered slowly until it makes contact with the water and then lowered an additional 20 μm to ensure even water contact, compensating for any unevenness in the sample's surface.

PA Lens Fabrication:

The PA lens is a 1.5 cm diameter glass plano-concave lens with a composite carbon soot and polydimethylsiloxane (PDMS) film applied to its concave surface. First, the lens is thoroughly cleaned using acetone, isopropanol, and deionized (DI) water, followed by oxygen plasma treatment using a 360-second O_2 strip recipe.

Next, PDMS is prepared by mixing 10 g of PDMS polymer with 1 g of primer and degassing the mixture in a vacuum chamber for 30 minutes. During this degassing process, the clean lens is subjected to flame synthesis by holding the concave surface over an unscented candle flame for three seconds. This process deposits a slightly transparent, uniform soot coating.

Once the soot coating is complete, the lens is placed on a spin coater. PDMS is carefully poured onto the edge of the soot-coated surface, filling the "bowl" of the lens about halfway. The lens is then spun at 500 rpm for 10 seconds, followed by 3,000 rpm for 30 seconds, ensuring uniform PDMS application. Finally, the lens is cured on a hot plate at 115 ℃ for 15 minutes.

PA Capsule Preparation:

A 3D-printed water capsule is attached to the exterior of the PA lens using Norland Optical Adhesive (UV-cured). The capsule is filled with DI water, completing the setup for printing solid materials. For liquid inks, a thin PVC film is placed over the water to separate the ink and water layers, ensuring no air bubbles are trapped beneath the film. The PVC film is glued to the capsule exterior, and a 1 mm tall ring is attached on top of the film and secured with UV-cured glue. A few drops of ink are added to the upper compartment, enabling jetting in the SJP system.

The completed capsule consists of two liquid compartments separated by the PVC film. The water layer allows the laser-generated focused ultrasound (LGFU) to travel to the focal point with minimal attenuation, while the ink layer is positioned for precise jetting.

CNT TFT Fabrication:

The gold source and drain contacts for CNT transistors were patterned on 90 nm SiO_2/Si substrates using photolithography, physical vapor deposition, and a resist-remover-based lift-off process. SPR 220 photoresist was patterned on the wafer, and 10 nm titanium followed by 50 nm gold were deposited onto the patterned areas.

For the semiconducting channels, a commercially available aqueous solution of 99.9% pure semiconducting single-walled carbon nanotubes (S-SWCNTs) from NanoIntegris, with a concentration of 0.01 mg/mL, was used. Prior to printing, the substrates were cleaned with acetone, isopropanol, and DI water, followed by oxygen plasma treatment for 4 minutes at 100 W to remove contaminants and improve CNT adhesion. To further promote adhesion, the substrates were soaked in a poly-l-lysine solution (0.1% w/v in water) for 5 minutes and rinsed in DI water.

Inkjet printing of CNTs was performed using a Fujifilm Dimatix Materials Printer (DMP-2850). The cartridge was operated at 40 °C, with a platen temperature of 60 °C. A single nozzle was used for printing, with a cartridge height of 300 μm, jetting voltage of 30 V, jetting frequency of 1 kHz, drop spacing of 20 μm, and a printing speed of approximately 10 mm/s. For SJP printing, the samples were translated at 50 μm/s, and the substrate was heated to 80 °C.

After printing, the samples were placed on a hot plate at 80 °C for 15 minutes to dry and then dipped in DI water at 80 °C for 10 seconds to remove proprietary surfactants. This step was conducted under a fume hood. Finally, the samples were annealed in a tube furnace at 200 °C under a forming gas atmosphere (H_2/N_2) for 40 minutes to complete the transistor fabrication process.

Bibliography

[1] Y. Zhou, F. Fan, Y. Liu, S. Zhao, Q. Xu, S. Wang, D. Luo, Y. Long, *Unconventional smart windows: Materials, structures and designs*, Vol. 90, Elsevier Ltd, **2021**.

[2] Z. Li, T. Ma, H. Yang, L. Lu, R. Wang, *Transparent and Colored Solar Photovoltaics for Building Integration*, Vol. 5, John Wiley and Sons Inc, **2021**.

[3] Jongsu Lee, Sang-Kyu Byun, Jeong-Dong Lee, Tai-Yoo Kim, In *PICMET '03: Portland International Conference on Management of Engineering and Technology Technology Management for Reshaping the World, 2003.*, Portland State Univ, **2003**, pp. 140–149.

[4] B. A. Rorem, T. H. Cho, N. Farjam, J. D. Lenef, K. Barton, N. P. Dasgupta, L. J. Guo, *ACS Appl Mater Interfaces* **2022**, *14*, 31099.

[5] G. Rasiya, A. Shukla, K. Saran, In *Materials Today: Proceedings*, Elsevier Ltd, **2020**, pp. 6896–6901.

[6] C. Sun, Y. Wang, M. D. McMurtrey, N. D. Jerred, F. Liou, J. Li, *Appl Energy* **2021**, *282*.

[7] B. Blakey-Milner, P. Gradl, G. Snedden, M. Brooks, J. Pitot, E. Lopez, M. Leary, F. Berto, A. du Plessis, *Mater Des* **2021**, *209*.

[8] C. Zhang, Y. Li, W. Kang, X. Liu, Q. Wang, *SusMat* **2021**, *1*, 127.

[9] D. Han, H. Lee, *Recent advances in multi-material additive manufacturing: methods and applications*, Vol. 28, Elsevier Ltd, **2020**, pp. 158–166.

[10] N. Divakaran, J. P. Das, A. K. P V, S. Mohanty, A. Ramadoss, S. K. Nayak, *Comprehensive review on various additive manufacturing techniques and its implementation in electronic devices*, Vol. 62, Elsevier B.V., **2022**, pp. 477–502.

[11] J. Sun, B. Bhushan, J. Tong, *Structural coloration in nature*, Vol. 3, **2013**, pp. 14862–14889.

[12] T. Xu, H. Shi, Y. K. Wu, A. F. Kaplan, J. G. Ok, L. J. Guo, *Small* **2011**, *7*, 3128.

[13] R. Christie, A. Abel, *Physical Sciences Reviews* **2021**, *6*, 807.

[14] M. Zayat, P. Garcia-Parejo, D. Levy, *Chem Soc Rev* **2007**, *36*, 1270.

[15] A. C. Arsenault, D. P. Puzzo, I. Manners, G. A. Ozin, *Nat Photonics* **2007**, *1*, 468.

[16] J. Hong, E. Chan, T. Chang, T.-C. Fung, B. Hong, C. Kim, J. Ma, Y. Pan, R. Van Lier, S. Wang, B. Wen, L. Zhou, *Optica* **2015**, *2*, 589.

[17] X. Zhu, C. Vannahme, E. Højlund-Nielsen, N. A. Mortensen, A. Kristensen, *Nat Nanotechnol* **2016**, *11*, 325.

[18] K. Kumar, H. Duan, R. S. Hegde, S. C. W. Koh, J. N. Wei, J. K. W. Yang, *Nat Nanotechnol* **2012**, *7*, 557.

[19] H. Kim, J. Ge, J. Kim, S. E. Choi, H. Lee, H. Lee, W. Park, Y. Yin, S. Kwon, *Nat Photonics* **2009**, *3*, 534.

[20] K. T. Lee, C. Ji, D. Banerjee, L. J. Guo, *Laser Photon Rev* **2015**, *9*, 354.

[21] D. Banerjee, M. Zhang, *J Mod Opt* **2010**, *57*, 1180.

[22] T. Masuda, Y. Kudo, D. Banerjee, *Coatings* **2018**, *8*.

[23] T. Masuda, S. Hirai, M. Inoue, J. Chantana, Y. Kudo, T. Minemoto, *IEEE J Photovolt* **2018**, *8*, 1326.

[24] C. Ji, Z. Zhang, T. Masuda, Y. Kudo, L. J. Guo, *Nanoscale Horiz* **2019**, *4*, 874.

[25] C. Ji, K. T. Lee, T. Xu, J. Zhou, H. J. Park, L. J. Guo, *Engineering Light at the Nanoscale: Structural Color Filters and Broadband Perfect Absorbers*, Vol. 5, Wiley-VCH Verlag, **2017**.

[26] G. Xu, L. Shen, C. Cui, S. Wen, R. Xue, W. Chen, H. Chen, J. Zhang, H. Li, Y. Li, Y. Li, *Adv Funct Mater* **2017**, *27*.

[27] J. H. Lu, Y. H. Lin, B. H. Jiang, C. H. Yeh, J. C. Kao, C. P. Chen, *Adv Funct Mater* **2018**, *28*.

[28] R. W. Sabnis, *Color filter technology for liquid crystal displays*.

[29] Z. Li, S. Butun, K. Aydin, *ACS Photonics* **2015**, *2*, 183.

[30] W. J. Feng, Y. Cheng, L. J. Guo, *ACS Photonics* **2023**, *10*, 2784.

[31] C. Ji, S. Acharya, K. Yamada, S. Maldonado, L. J. Guo, *ACS Appl Mater Interfaces* **2019**, *11*, 29065.

[32] B. A. Rorem, Y. Cheng, L. J. Guo, *Adv Funct Mater* **2024**.

[33] W.-J. Feng, *Multilayer Structural Colors Realized by Solution-based Fabrications*.

[34] A. Saha, T. Ma, H. Wang, L. J. Guo, *ACS Appl Mater Interfaces* **2023**, *15*, 28772.

[35] A. Roorda, D. R. Williams, *Letters to Nature* **1999**, *397*, 520.

[36] M. C. Stone, W. B. Cowan, J. C. Beatty, *ACM Trans Graph* **1988**, *7*, 249.

[37] K. E. Spaulding, G. J. Woolfe, R. L. Joshi, *Col Res Appl* **2003**, *28*, 251.

[38] H. S. Chen, T. T. Chang, *Journal of Imaging Science and Technology* **2009**, *53*.

[39] H. S. Fairman, M. H. Brill, H. Hemmendinger, *Color Res Appl* **1997**, *22*, 11.

[40] C. Connolly, T. Fliess, *A Study of Efficiency and Accuracy in the Transformation from RGB to CIELAB Color Space*, Vol. 6, **1997**.

[41] M. Amara, F. Mandorlo, R. Couderc, F. Gérenton, M. Lemiti, *EPJ Photovoltaics* **2018**, *9*.

[42] X. Kong, M. Wei, M. J. Murdoch, I. Vogels, I. Heynderickx, *Journal of the Optical Society of America A* **2020**, *37*, 521.

[43] L. M. Hurvich, D. Jameson, *Psychol Rev* **1957**, *64*, 384.

[44] K. K. Niall, *Spat Vis* **1988**, *3*, 79.

[45] K. Godo, O. Watari, *Opt Rev* **2023**, *30*, 290.

[46] K. McLaren, *Journal of the Society of Dyers and Colourists* **1970**, *86*, 354.

[47] J. A. Endler, *On the measurement and classification of colour in studies of animal colour patterns*, Vol. 41, **1990**.

[48] C. Ji, K.-T. Lee, L. J. Guo, *Opt Lett* **2019**, *44*, 86.

[49] H. Gu, Y. Zhao, Y. Cheng, Z. Xie, F. Rong, J. Li, B. Wang, D. Fu, Z. Gu, *Small* **2013**, *9*, 2266.

[50] H. S. Lee, T. S. Shim, H. Hwang, S. M. Yang, S. H. Kim, *Chemistry of Materials* **2013**, *25*, 2684.

[51] H. Wang, K. Q. Zhang, *Photonic crystal structures with tunable structure color as colorimetric sensors*, Vol. 13, MDPI AG, **2013**, pp. 4192–4213.

[52] K. Lee, L. K. Povlich, J. Kim, *Analyst* **2010**, *135*, 2179.

[53] O. B. Ayyub, J. W. Sekowski, T. I. Yang, X. Zhang, R. M. Briber, P. Kofinas, *Biosens Bioelectron* **2011**, *28*, 349.

[54] N. Arrousse, J. Ferreira, S. Carvalho, M. Andritschky, *Coatings* **2023**, *13*.

[55] D. Wang, Z. Liu, H. Wang, M. Li, L. J. Guo, C. Zhang, *Structural color generation: From layered thin films to optical metasurfaces*, Vol. 12, De Gruyter Open Ltd, **2023**, pp. 1019–1081.

[56] L. M. Greenstein, *Pigment Handbook: Properties and Economics* (Ed.: Patton, T. C.), Vol. 1, John Wiley and Sons, New York, **1973**.

[57] M. A. Kats, R. Blanchard, P. Genevet, F. Capasso, *Nat Mater* **2013**, *12*, 20.

[58] M. A. Kats, S. J. Byrnes, R. Blanchard, M. Kolle, P. Genevet, J. Aizenberg, F. Capasso, *Appl Phys Lett* **2013**, *103*.

[59] M. de Kersauson, M. el Kurdi, S. David, X. Checoury, G. Fishman, S. Sauvage, R. Jakomin, G. Beaudoin, I. Sagnes, P. Boucaud, *Opt Express* **2011**, *19*, 17925.

[60] Y. G. Kim, Y. J. Quan, M. S. Kim, Y. Cho, S. H. Ahn, *International Journal of Precision Engineering and Manufacturing - Green Technology* **2021**, *8*, 997.

[61] D. F. Swinehart, *J Chem Educ* **1962**, *39*, 333.

[62] A. I. Lvovsky, *Encyclopedia of Optical and Photonic Engineering (Print) - Five Volume Set* (Eds.: Hoffman, C.; Driggers, R.), 2nd ed., Vol. 2, CRC Press, Boca Raton, **2015**.

[63] X. Shi, J. He, X. Lu, *Dyes and Pigments* **2020**, *175*.

[64] H. Wang, L. J. Guo, *iScience* **2022**, *25*, 104339.

[65] H. Wang, Z. Zheng, C. Ji, L. Jay Guo, *Mach Learn Sci Technol* **2021**, *2*, 025013.

[66] T. Ma, H. Wang, L. J. Guo, *Opto-Electronic Advances* **2024**, *7*.

[67] C. Yang, W. Shen, Y. Zhang, K. Li, X. Fang, X. Zhang, X. Liu, *Sci Rep* **2015**, *5*.

[68] Z. Yang, C. Ji, D. Liu, L. J. Guo, *Adv Opt Mater* **2019**, *7*.

[69] U.S. Environmental Protection Agency, *Compilation of Air Pollutant Emissions Factors from Stationary Sources (AP-42), Fifth Edition, Volume 1*, **1996**.

[70] D. Santos-Cruz, S. A. Mayén-Hernández, F. de Moure-Flores, J. Campos-Álvarez, M. Pal, J. Santos-Cruz, *Results Phys* **2017**, *7*, 4140.

[71] M. F. Al-Kuhaili, M. Saleem, S. M. A. Durrani, *J Alloys Compd* **2012**, *521*, 178.

[72] T. Hansen, *Rutile*, **2024**.

[73] T. Hansen, *Copper Oxide Black*, **2024**.

[74] T. Hansen, *Iron Oxide Red*, **2024**.

[75] T. Hansen, *Silica*, **2024**.

[76] W. Kroll, *Transactions of the American Electrochemical Society* **1940**, *78*.

[77] M. Hasegawa, In *Treatise on Process Metallurgy*, Elsevier Ltd., **2013**, pp. 507–516.

[78] G. H. Major, D. J. Morgan, M. R. Linford, *Vacuum Technology & Coating* **2022**, 30.

[79] C. Tian, Y. Rao, G. Su, T. Huang, C. Xiang, *J Chem* **2022**, *2022*.

[80] X. Zhang, Y. Song, L. Wu, N. Yin, J. Bao, Y. Li, *Miner Eng* **2022**, *184*.

[81] L. V. Rodríguez-de Marcos, J. I. Larruquert, J. A. Méndez, J. A. Aznárez, *Opt Mater Express* **2016**, *6*, 3622.

[82] H. A. A. Abdelbagi, E. G. Njoroge, T. M. Mohlala, T. Mokgadi, R. Heller, F. Schmidl, T. T. Hlatshwayo, C. Ronning, J. B. Malherbe, *Mater Chem Phys* **2023**, *309*.

[83] B. Scheffel, T. Modes, C. Metzner, *Surf Coat Technol* **2016**, *287*, 138.

[84] E. Ritter, *Journal of Vacuum Science and Technology* **1966**, *3*, 225.

[85] H. K. Pulker, G. Paesold, E. Ritter, *Refractive indices of TiO 2 films produced by reactive evaporation of various titanium-oxygen phases*.

[86] D. R. Lide, *CRC Handbook of Chemistry and Physics, 79th Edition*, **1998**.

[87] N. Pauly, S. Tougaard, F. Yubero, *Surf Sci* **2014**, *620*, 17.

[88] T. Yamashita, P. Hayes, *Appl Surf Sci* **2008**, *254*, 2441.

[89] P. Mills, J. L. Sullivan, *A study of the core level electrons in iron and its three oxides by means of x-ray photoelectron spectroscopy*, Vol. 16, **1983**.

[90] M. C. Biesinger, *Surface and Interface Analysis* **2017**, *49*, 1325.

[91] B. L. Fulton, C. K. Perkins, R. H. Mansergh, M. A. Jenkins, V. Gouliouk, M. N. Jackson, J. C. Ramos, N. M. Rogovoy, M. T. Gutierrez-Higgins, S. W. Boettcher, J. F. Conley, D. A. Keszler, J. E. Hutchison, D. W. Johnson, *Chemistry of Materials* **2017**, *29*, 7760.

[92] M. M. Bellah, S. M. Christensen, S. M. Iqbal, *Nanostructures for medical diagnostics*, Vol. 2012, **2012**.

[93] K. R. Balasubramaniam, V. M. Kao, J. Ravichandran, P. B. Rossen, W. Siemons, J. W. Ager, *Thin Solid Films* **2012**, *520*, 3914.

[94] A. Abd El Hamid Hassan, S. Abd El Moez Elnagar, I. Mohammadi El Tayeb, S. Abd El Halim Bolbol, *Open Journal of Safety Science and Technology* **2013**, *03*, 87.

[95] Robert L. Shook, *Why Didn't I Think of That!*, New American Library, **1982**.

[96] M. Kamalisarvestani, R. Saidur, S. Mekhilef, F. S. Javadi, *Performance, materials and coating technologies of thermochromic thin films on smart windows*, Vol. 26, Elsevier Ltd, **2013**, pp. 353–364.

[97] C. G. Granqvist, G. A. Niklasson, *Thermochromic oxide-based thin films and nanoparticle composites for energy-efficient glazings*, Vol. 7, MDPI AG, **2017**.

[98] O. Inganas, G. Gustafsson, W. R. Salaneck, *C377 C384 C377 THERMOCHROMISM IN THIN FILMS OF POLY(5-ALKYLTHIOPHENES)*, Vol. 28, **1989**, pp. 377–384.

[99] B. G. Kim, M. S. Kim, J. Kim, *ACS Nano* **2010**, *4*, 2160.

[100] H. Hintz, H. J. Egelhaaf, L. Lüer, J. Hauch, H. Peisert, T. Chassé, *Chemistry of Materials* **2011**, *23*, 145.

[101] Edward D. Palik, Gorachand Ghosh, *Handbook of Optical Constants of Solids*, Vol. V, Elsevier, **1997**.

[102] G. Rego, *Sensors* **2023**, *23*.

[103] J.-C. Weeber, A. Andrieux, M.-M. Gourier, J. Arocas, L. Markey, K. Hammani, A. Bouhelier, D. V. Bellas, E. Lidorikis, N. Pleros, *Opt Mater Express* **2023**, *13*, 2882.

[104] R. Suriano, R. Ciapponi, G. Griffini, M. Levi, S. Turri, *Surf Coat Technol* **2017**, *311*, 80.

[105] C. Seubert, K. Nietering, M. Nichols, R. Wykoff, S. Bollin, *An overview of the scratch resistance of automotive coatings: Exterior clearcoats and polycarbonate hardcoats*, Vol. 2, MDPI AG, **2012**, pp. 221–234.

[106] N. P. Dasgupta, H.-B.-R. Lee, S. F. Bent, P. S. Weiss, *Chemistry of Materials* **2016**, *28*, 1943.

[107] M. G. Steven, *Chem Rev* **2010**, *110*, 111.

[108] A. J. Gayle, Z. J. Berquist, Y. Chen, A. J. Hill, J. Y. Hoffman, A. R. Bielinski, A. Lenert, N. P. Dasgupta, *Chemistry of Materials* **2021**, *33*, 5572.

[109] R. E. Rodríguez, S. P. Agarwal, S. An, E. Kazyak, D. Das, W. Shang, R. Skye, T. Deng, N. P. Dasgupta, *ACS Appl Mater Interfaces* **2018**, *10*, 4614.

[110] A. R. Bielinski, M. Boban, Y. He, E. Kazyak, D. H. Lee, C. Wang, A. Tuteja, N. P. Dasgupta, *ACS Nano* **2017**, *11*, 478.

[111] E. Kazyak, K. H. Chen, Y. Chen, T. H. Cho, N. P. Dasgupta, *Adv Energy Mater* **2022**, *12*, 1.

[112] V. Cremers, R. L. Puurunen, J. Dendooven, *Appl Phys Rev* **2019**, *6*.

[113] M. Knez, K. Nielsch, L. Niinistö, *Advanced Materials* **2007**, *19*, 3425.

[114] Y. Chen, N. J. Ginga, W. S. LePage, E. Kazyak, A. J. Gayle, J. Wang, R. E. Rodríguez, M. D. Thouless, N. P. Dasgupta, *ACS Appl Mater Interfaces* **2019**, *11*, 43573.

[115] A. R. Bielinski, E. Kazyak, C. M. Schlepütz, H. J. Jung, K. N. Wood, N. P. Dasgupta, *Chemistry of Materials* **2015**, *27*, 4799.

[116] C. R. Ellinger, S. F. Nelson, **2014**.

[117] P. Poodt, B. Kniknie, A. Branca, H. Winands, F. Roozeboom, *Physica Status Solidi - Rapid Research Letters* **2011**, *5*, 165.

[118] I. Katsouras, C. Frijters, P. Poodt, G. Gelinck, A. J. Kronemeijer, *J Soc Inf Disp* **2019**, jsid. 783.

[119] S. Ng, C. Iffelsberger, J. Michalička, M. Pumera, *ACS Nano* **2021**, *15*, 686.

[120] S. Ng, R. Zazpe, J. Rodriguez-Pereira, J. Michalička, J. M. Macak, M. Pumera, *J Mater Chem A Mater* **2021**, *9*, 11405.

[121] G. N. Parsons, R. D. Clark, *Chemistry of Materials* **2020**, *32*, 4920.

[122] H. B. R. Lee, S. F. Bent, *Chemistry of Materials* **2020**, 3323.

[123] A. J. M. Mackus, M. J. M. Merkx, W. M. M. Kessels, **2019**.

[124] W. Lee, N. P. Dasgupta, O. Trejo, J. Lee, J. Hwang, T. Usui, F. B. Prinz, **2010**, *26*, 6845.

[125] D. Bobb-Semple, K. L. Nardi, N. Draeger, D. M. Hausmann, S. F. Bent, *Chemistry of Materials* **2019**, *31*, 1635.

[126] A. J. M. MacKus, S. A. F. Dielissen, J. J. L. Mulders, W. M. M. Kessels, *Nanoscale* **2012**, *4*, 4477.

[127] D. H. Levy, C. R. Ellinger, S. F. Nelson, *Appl Phys Lett* **2013**, *103*.

[128] A. Sinha, D. W. Hess, C. L. Henderson, *Journal of Vacuum Science & Technology B: Microelectronics and Nanometer Structures* **2006**, *24*, 2523.

[129] X. Jiang, S. F. Bent, *Journal of Physical Chemistry C* **2009**, *113*, 17613.

[130] A. Mameli, B. Karasulu, M. A. Verheijen, B. Barcones, B. Macco, A. J. M. Mackus, W. M. M. E. Kessels, F. Roozeboom, *Chemistry of Materials* **2019**, *31*, 1250.

[131] C. R. Ellinger, S. F. Nelson, *Chemistry of Materials* **2014**, *26*, 1514.

[132] T. H. Cho, N. Farjam, C. R. Allemang, C. P. Pannier, E. Kazyak, C. Huber, M. Rose, O. Trejo, R. L. Peterson, K. Barton, N. P. Dasgupta, *ACS Nano* **2020**, *14*, 17262.

[133] N. Farjam, T. H. Cho, N. P. Dasgupta, K. Barton, *Appl Phys Lett* **2020**, *117*.

[134] N. Farjam, T. H. Cho, N. P. Dasgupta, K. Barton, *Appl Phys Lett* **2020**, *117*.

[135] K. Li, T. Li, T. Zhang, H. Li, A. Li, Z. Li, X. Lai, X. Hou, Y. Wang, L. Shi, M. Li, Y. Song, *Facile full-color printing with a single transparent ink*, Vol. 7, **2021**.

[136] D. S. Engstrom, B. Porter, M. Pacios, H. Bhaskaran, *J Mater Res* **2014**, *29*, 1792.

[137] J. U. Park, M. Hardy, S. J. Kang, K. Barton, K. Adair, D. K. Mukhopadhyay, C. Y. Lee, M. S. Strano, A. G. Alleyne, J. G. Georgiadis, P. M. Ferreira, J. A. Rogers, *Nat Mater* **2007**, *6*, 782.

[138] M. S. Onses, E. Sutanto, P. M. Ferreira, A. G. Alleyne, J. A. Rogers, *Small* **2015**, *11*, 4237.

[139] V. Miikkulainen, M. Leskelä, M. Ritala, R. L. Puurunen, *Crystallinity of inorganic films grown by atomic layer deposition: Overview and general trends*, Vol. 113, **2013**.

[140] J. D. Lenef, J. Jo, O. Trejo, D. J. Mandia, R. L. Peterson, N. P. Dasgupta, *Journal of Physical Chemistry C* **2021**, *125*, 9383.

[141] Z. Li, A. Rahtu, R. G. Gordon, *J Electrochem Soc* **2006**, *153*, C787.

[142] E. Färm, M. Kemell, E. Santala, M. Ritala, M. Leskelä, *J Electrochem Soc* **2010**, *157*, K10.

[143] E. Färm, M. Kemell, M. Ritala, M. Leskelä, *Journal of Physical Chemistry C* **2008**, *112*, 15791.

[144] N. E. Richey, C. De Paula, S. F. Bent, *Journal of Chemical Physics* **2020**, *152*.

[145] H.-B.-R. Lee, *Chemistry of Materials* **2019**, *31*, 1471.

[146] A. J. M. Mackus, A. A. Bol, W. M. M. Kessels, **2014**, 10941.

[147] T. H. Cho, N. Farjam, K. Barton, N. P. Dasgupta, *Small Methods* **2024**, *8*.

[148] Z. J. Berquist, A. J. Gayle, N. P. Dasgupta, A. Lenert, *Adv Funct Mater* **2022**, *32*.

[149] Z. Yang, C. Ji, Q. Cui, L. J. Guo, *Adv Opt Mater* **2020**, *8*.

[150] D. Penley, T. H. Cho, A. J. Brooks, L. Ransohoff, H. Park, E. Herman, E. Zhao, O. Trejo, K. Barton, N. P. Dasgupta, *Adv Mater Technol* **2024**, *9*.

[151] W. S. Wong, M. L. Chabinyc, T.-N. Ng, A. Salleo, *Flexible Electronics: Materials and Applications*, Springer, New York, **2009**.

[152] Y. Rogers, J.A., Someya, T. and Huang, *Science (1979)* **2010**, pp. 1603.

[153] A. C. Arias, J. D. MacKenzie, I. McCulloch, J. Rivnay, A. Salleo, *Chem Rev* **2010**, *110*, 3.

[154] M. L. Hammock, A. Chortos, B. C.-K. Tee, J. B.-H. Tok, Z. Bao, *Advanced Materials* **2013**, *25*, 5997.

[155] iNEMI flexible hybrid electronics roadmap, **2017**.

[156] Y. Khan, A. Thielens, S. Muin, J. Ting, C. Baumbauer, A. C. Arias, *A New Frontier of Printed Electronics: Flexible Hybrid Electronics*, Vol. 32, Wiley-VCH Verlag, **2020**.

[157] T. R. Ray, J. Choi, A. J. Bandodkar, S. Krishnan, P. Gutruf, L. Tian, R. Ghaffari, J. A. Rogers, *Bio-integrated wearable systems: A comprehensive review*, Vol. 119, American Chemical Society, **2019**, pp. 5461–5533.

[158] T. Starner, *IEEE Micro* **2001**, *21*, 44.

[159] Y. Lin, M. Bariya, A. Javey, *Adv Funct Mater* **2021**, *31*.

[160] H. Xu, L. Yin, C. Liu, X. Sheng, N. Zhao, *Recent Advances in Biointegrated Optoelectronic Devices*, Vol. 30, Wiley-VCH Verlag, **2018**.

[161] Y. Khan, A. E. Ostfeld, C. M. Lochner, A. Pierre, A. C. Arias, *Monitoring of Vital Signs with Flexible and Wearable Medical Devices*, Vol. 28, Wiley-VCH Verlag, **2016**, pp. 4373–4395.

[162] S. F. Shaikh, H. F. Mazo-Mantilla, N. Qaiser, S. M. Khan, J. M. Nassar, N. R. Geraldi, C. M. Duarte, M. M. Hussain, *Small* **2019**, *15*.

[163] A. Kamyshny, S. Magdassi, *Conductive nanomaterials for printed electronics*, Vol. 10, Wiley-VCH Verlag, **2014**, pp. 3515–3535.

[164] R. Herbert, J. H. Kim, Y. S. Kim, H. M. Lee, W. H. Yeo, *Soft material-enabled, flexible hybrid electronics for medicine, healthcare, and human-machine interfaces*, Vol. 11, MDPI AG, **2018**.

[165] Y. Li, S. Nayak, Y. Luo, Y. Liu, H. K. S. V. Mohan, J. Pan, Z. Liu, C. H. Heng, A. V. Y. Thean, *Materials* **2019**, *12*.

[166] Y. Ma, Y. Zhang, S. Cai, Z. Han, X. Liu, F. Wang, Y. Cao, Z. Wang, H. Li, Y. Chen, X. Feng, *Flexible Hybrid Electronics for Digital Healthcare*, Vol. 32, Wiley-VCH Verlag, **2020**.

[167] V. Subramanian, J. B. Chang, A. de la F. Vornbrock, D. C. Huang, L. Jagannathan, F. Liao, B. Mattis, S. Molesa, D. R. Redinger, D. Soltman, S. K. Volkman, Q. Zhang, In *European Conference on Solid-State Circuits*, IEEE, **2008**.

[168] S. R. Forrest, *Nature* **2004**, *428*, 911.

[169] S. Khan, L. Lorenzelli, R. S. Dahiya, *IEEE Sens J* **2015**, *15*, 3164.

[170] C. Yeom, K. Chen, D. Kiriya, Z. Yu, G. Cho, A. Javey, *Advanced Materials* **2015**, *27*, 1561.

[171] S. Yao, Y. Zhu, *Nanoscale* **2014**, *6*, 2345.

[172] L. Li, L. Pan, Z. Ma, K. Yan, W. Cheng, Y. Shi, G. Yu, *Nano Lett* **2018**, *18*, 3322.

[173] S. Harada, W. Honda, T. Arie, S. Akita, K. Takei, *ACS Nano* **2014**, *8*, 3921.

[174] J. B. Andrews, C. Cao, M. A. Brooke, A. D. Franklin, *IEEE Sens J* **2017**, *17*, 4612.

[175] Y. Yamamoto, S. Harada, D. Yamamoto, W. Honda, T. Arie, S. Akita, K. Takei, *Printed multifunctional flexible device with an integrated motion sensor for health care monitoring*, **2016**.

[176] S. Kholghi Eshkalak, A. Chinnappan, W. A. D. M. Jayathilaka, M. Khatibzadeh, E. Kowsari, S. Ramakrishna, *Appl Mater Today* **2017**, *9*, 372.

[177] S. G. Bucella, J. M. Salazar-Rios, V. Derenskyi, M. Fritsch, U. Scherf, M. A. Loi, M. Caironi, *Adv Electron Mater* **2016**, *2*.

[178] K. D. Ausman, R. Piner, O. Lourie, R. S. Ruoff, M. Korobov, *Journal of Physical Chemistry B* **2000**, *104*, 8911.

[179] D. Bucknall, *Nanolithography and Patterning Techniques in Microelectronics*, 1st ed., Woodhead Publishing, **2005**.

[180] W. S. Wong, E. M. Chow, R. Lujan, V. Geluz-Aguilar, M. L. Chabinyc, *Appl Phys Lett* **2006**, *89*.

[181] B. Ballarin, A. Fraleoni-Morgera, D. Frascaro, S. Marazzita, C. Piana, L. Setti, *Synth Met* **2004**, *146*, 201.

[182] Inc. FUJIFILM Dimatix, *FUJIFILM Dimatix Materials Printer DMP-2800 Series User Manual*, **2010**.

[183] D. B. Bogy, F. E. Taike, *IBM J Res Dev* **1984**, *28*.

[184] L. Hu, D. S. Hecht, G. Gruner, *Nano Lett* **2004**, *4*, 2513.

[185] K. Schnittker, M. Tursunniyaz, J. B. Andrews, *Journal of Information Display* **2021**, *22*, 193.

[186] D. Corzo, K. Almasabi, E. Bihar, S. Macphee, D. Rosas-Villalva, N. Gasparini, S. Inal, D. Baran, *Adv Mater Technol* **2019**, *4*.

[187] R. P. Tortorich, J. W. Choi, *Inkjet printing of carbon nanotubes*, Vol. 3, MDPI, **2013**, pp. 453–468.

[188] D. S. Hecht, L. Hu, G. Irvin, *Emerging transparent electrodes based on thin films of carbon nanotubes, graphene, and metallic nanostructures*, Vol. 23, **2011**, pp. 1482–1513.

[189] Dimatix, *Highlights Cartridge Specifications*, **2021**.

[190] Dimatix, *Materials Printer & Cartridge DMP-2800 Series Printer & DMC-11600 Series Cartridge*, **2008**.

[191] T. Lee, H. W. Baac, J. G. Ok, H. S. Youn, L. J. Guo, *Phys Rev Appl* **2014**, *2*.

[192] H. W. Baac, J. G. Ok, A. Maxwell, K. T. Lee, Y. C. Chen, A. J. Hart, Z. Xu, E. Yoon, L. J. Guo, *Sci Rep* **2012**, *2*.

[193] S. Mitragotri, *Nat Rev Drug Discov* **2006**, *5*, 543.

[194] S. A. Elrod, B. Hadimioglu, B. T. Khuri-Yakub, E. G. Rawson, E. Richley, C. F. Quate, N. N. Mansour, T. S. Lundgren, *J Appl Phys* **1989**, *65*, 3441.

[195] S. T. Thoroddsen, K. Takehara, T. G. Etoh, C. D. Ohl, *Physics of Fluids* **2009**, *21*, 1.

[196] A. Patrascioiu, J. M. Fernández-Pradas, J. L. Morenza, P. Serra, In *Applied Surface Science*, Elsevier B.V., **2014**, pp. 303–308.

[197] A. Patrascioiu, J. M. Fernández-Pradas, A. Palla-Papavlu, J. L. Morenza, P. Serra, *Microfluid Nanofluidics* **2014**, *16*, 55.

[198] S. Seva, B. Rorem, K. Chinnathambi, D. Estrada, L. J. Guo, H. Subbaraman, *Small Methods* **2024**.

[199] K. Chen, W. Gao, S. Emaminejad, D. Kiriya, H. Ota, H. Y. Y. Nyein, K. Takei, A. Javey, *Printed Carbon Nanotube Electronics and Sensor Systems*, Vol. 28, Wiley-VCH Verlag, **2016**, pp. 4397–4414.

[200] G. L. Goh, S. Agarwala, W. Y. Yeong, *ACS Appl Mater Interfaces* **2019**, *11*, 43719.

[201] Z. Cheng, C. S. Pang, P. Wang, S. T. Le, Y. Wu, D. Shahrjerdi, I. Radu, M. C. Lemme, L. M. Peng, X. Duan, Z. Chen, J. Appenzeller, S. J. Koester, E. Pop, A. D. Franklin, C. A. Richter, *Nat Electron* **2022**, *5*, 416.

[202] A. D. Franklin, M. C. Hersam, H.-S. P. Wong, *Science (1979)* **2022**, *378*, 726.

[203] D. Estrada, S. Dutta, A. Liao, E. Pop, *Nanotechnology* **2010**, *21*.

[204] Q. Cao, M. Xia, C. Kocabas, M. Shim, J. A. Rogers, S. V. Rotkin, *Appl Phys Lett* **2007**, *90*.

[205] Q. Cao, H. S. Kim, N. Pimparkar, J. P. Kulkarni, C. Wang, M. Shim, K. Roy, M. A. Alam, J. A. Rogers, *Nature* **2008**, *454*, 495.

[206] C. Wang, J. C. Chien, K. Takei, T. Takahashi, J. Nah, A. M. Niknejad, A. Javey, *Nano Lett* **2012**, *12*, 1527.

[207] T. Dürkop, B. M. Kim, M. S. Fuhrer, *Properties and applications of high-mobility semiconducting nanotubes*, Vol. 16, **2004**.

[208] T. Dürkop, S. A. Getty, E. Cobas, M. S. Fuhrer, *Nano Lett* **2004**, *4*, 35.

[209] D. A. Ryndyk, In *Springer Series in Solid-State Sciences*, Springer Science and Business Media Deutschland GmbH, **2016**, pp. 17–54.

[210] D. Hecht, L. Hu, G. Grüner, *Appl Phys Lett* **2006**, *89*.

[211] D. Estrada, E. Pop, *Appl Phys Lett* **2011**, *98*.

[212] M. Y. Timmermans, D. Estrada, A. G. Nasibulin, J. D. Wood, A. Behnam, D. ming Sun, Y. Ohno, J. W. Lyding, A. Hassanien, E. Pop, E. I. Kauppinen, *Nano Res* **2012**, *5*, 307.

[213] F. Scuratti, J. M. Salazar-Rios, A. Luzio, S. Kowalski, S. Allard, S. Jung, U. Scherf, M. A. Loi, M. Caironi, *Adv Funct Mater* **2021**, *31*.

[214] A. E. Islam, J. A. Rogers, M. A. Alam, *Recent Progress in Obtaining Semiconducting Single-Walled Carbon Nanotubes for Transistor Applications*, Vol. 27, Wiley-VCH Verlag, **2015**, pp. 7908–7937.

[215] N. Pimparkar, Q. Cao, J. A. Rogers, M. A. Alam, *Nano Res* **2009**, *2*, 167.

[216] C. Wang, J. Zhang, K. Ryu, A. Badmaev, L. G. De Arco, C. Zhou, *Nano Lett* **2009**, *9*, 4285.

[217] N. Rouhi, D. Jain, K. Zand, P. J. Burke, *Advanced Materials* **2011**, *23*, 94.

[218] D. Hecht, L. Hu, G. Grüner, *Appl Phys Lett* **2006**, *89*.

[219] S. P. Schießl, X. De Vries, M. Rother, A. Massé, M. Brohmann, P. A. Bobbert, J. Zaumseil, *Phys Rev Mater* **2017**, *1*.

[220] J. Manzi, A. E. Weltner, T. Varghese, N. McKibben, M. Busuladzic-Begic, D. Estrada, H. Subbaraman, *Nanoscale* **2023**, *15*, 6596.

[221] S. J. Choi, P. Bennett, D. Lee, J. Bokor, *Nano Res* **2015**, *8*, 1320.

[222] A. Sugimoto, H. Ochi, S. Fujimura, A. Yoshida, T. Miyadera, M. Tsuchida, *IEEE Journal on Selected Topics in Quantum Electronics* **2004**, *10*, 107.

[223] C. mo Kang, H. Lee, *Journal of Information Display* **2022**, *23*, 19.

[224] K. Chung, M. S. Kwon, B. M. Leung, A. G. Wong-Foy, M. S. Kim, J. Kim, S. Takayama, J. Gierschner, A. J. Matzger, J. Kim, *ACS Cent Sci* **2015**, *1*, 94.

[225] Y. Li, P. Sonar, L. Murphy, W. Hong, *High mobility diketopyrrolopyrrole (DPP)-based organic semiconductor materials for organic thin film transistors and photovoltaics*, Vol. 6, **2013**, pp. 1684–1710.

[226] D. Chandran, K. S. Lee, *Diketopyrrolopyrrole: A versatile building block for organic photovoltaic materials*, Vol. 21, **2013**, pp. 272–283.

[227] H. Kim, K. Saitmacher, L. Unverdorben, C. Wille, In *Macromolecular Symposia*, John Wiley and Sons Ltd, **2002**, pp. 617–630.

[228] M. A. Baldo, V. G. Kozlov, P. E. Burrows, S. R. Forrest, V. S. Ban, B. Koene, M. E. Thompson, *Appl Phys Lett* **1997**, *71*, 3033.

[229] T. Ikeda, H. Murata, Y. Kinoshita, J. Shike, Y. Ikeda, M. Kitano, *Chem Phys Lett* **2006**, *426*, 111.

[230] S. Murano, K. Gilge, M. Ammann, A. Werner, *Dig Tech Pap* **2014**, *45*, 403.

[231] C. Kim, K. Kim, O. Kwon, J. Jung, J. K. Park, D. H. Kim, K. Jung, In *Digest of Technical Papers - SID International Symposium*, Blackwell Publishing Ltd, **2020**, pp. 905–908.

[232] C. Han, Y. Tak, B. Ahn, *J Soc Inf Disp* **2011**, *19*, 190.